ABSTRACT

Title of Dissertation: MOLECULAR-SCALE EXPLORATION OF INTERACTIONS BETWEEN DROPS AND PARTICLES WITH A POLYMERIC LAYER

Sai Ankit Etha, Doctor of Philosophy, 2023

Dissertation directed by: Professor Siddhartha Das, Department of Mechanical Engineering, University of Maryland.

Surface-grafted polymer molecules have been extensively employed for surface modifications as they ensure changes to the inherent physical/chemical properties of surface. Bottom-up surface processing with well-defined polymeric structures becomes increasingly important in many current technologies. Polymer brushes, which are polymer molecules grafted to a substrate by its one end at close enough proximity (thereby ensuring that they stretch out like the "bristles" of a toothbrush), provide an exemplary system of materials capable of achieving such a goal. In particular, producing functional polymer brushes with well-defined chemical configurations, densities, architectures, and thicknesses on a material surface has become increasingly important in many fields.

In my dissertation, I employ Molecular Dynamics (MD) simulations to study the interplay of interactions between nanoparticles (NPs), solvent drops and polymer grafted surfaces under

various system conditions. This study will help us to understand (1) the wetting dynamics of brush grafted surfaces and the associated brush conformational changes, (2) polymer-insoluble solvophilic NP assembly in brush grafted surfaces and the steric interactions driven establishment of direct contacts between a NP and a polymer layer (highly phobic to the NP), and (3) microphase separation and distillation-like behavior of grafted polymer bilayers interacting with a binary liquid mixture, and the resulting nanofluidic valving behavior of swollen polymer bilayers in a weak interpenetration regime.

In Chapter 1, I provide the background and motivation of the research presented in this thesis.

In Chapter 2, I study the spreading and imbibition of a liquid drop on a porous, soft, solvophilic, and responsive surface represented by a layer of polymer molecules grafted on a solvophilic solid. These polymer molecules are in a crumpled and collapsed globule-like state before the interaction with the drop, but transition to a "brush"-like state as they get wetted by the liquid drop. We hypothesize that for a wide range of densities of polymer grafting (σ_g), the drop spreading is dictated by the balance of the driving inertial pressure and balancing viscoelastic dissipation, associated with the spreading of the liquid drop on the polymer layer that undergoes globule-to-brush transition and serves as the viscoelastic solid. Finally, I argue that these simulations raise the possibility of designing soft and "responsive" and widely deployable liquid-infused surfaces where the polymer grafted solid, with the polymer undergoing a globule-to-brush transition, serving as the responsive "surface".

In Chapter 3, I employ coarse-grained molecular dynamics (MD) simulations and establish that under appropriate conditions, it is possible to develop numerous stable direct contacts between a polymer-insoluble NP and a solvated polymer layer (the polymer layer is phobic to the NP, while the solvent/liquid is philic to both the NP and the polymer). The NP is driven inside a layer of

collapsed and phobic (to the NP) polymer molecules by a drop of this liquid (which is philic to both the NP and the polymer layer). The liquid molecules imbibe and diffuse inside the polymer layer, but the NP remains localized within the polymer layer, due to large Steric effects, ensuring the establishment of highly stable numerous direct contacts between the NP and the highly phobic polymer molecules. Finally, I argue that our finding will open up avenues for leveraging NP-polymer interactions for a myriad of applications even for cases where the polymer molecules are phobic to the NPs.

In Chapter 4, I study the interaction of a binary mixture drop, containing two-miscible-liquids, with a polymer functionalized nanochannel that is philic to one of the liquids and phobic to the other. Liquid-liquid phase separation is achieved due to the asymmetry of interaction of the liquid species and we observe distillation like behavior wherein the drop becomes progressively concentrated with the phobic liquid with each ‘“pass” with the polymer bilayer absorbing an increasing fraction of the philic liquid molecules and transitioning into the polymer brush regime. Depending on the nanochannel height, the number of allowed passes varies, as the polymer chains stretch out until the oppositely grafted layers overlap and create a dense region of liquid infused polymer layers that act as a valve. Any further passage of drops through this nano-confined interpenetrating brush bilayer requires a much greater magnitude of applied force on the drop. I finally propose a design of nanovalves based on this mechanism of creating partially porous interpenetrating polymer brush layers.

MOLECULAR-SCALE EXPLORATION OF INTERACTIONS BETWEEN DROPS AND PARTICLES WITH A POLYMERIC LAYER

by

Sai Ankit Etha

Dissertation submitted to the Faculty of the Graduate School of the
University of Maryland, College Park, in partial fulfillment
of the requirements for the degree of
Doctor of Philosophy
2023

Advisory Committee:
Professor Siddhartha Das, Chair
Professor Pratyush Tiwary
Professor Amir Riaz
Professor Avik Dutt
Professor Taylor J. Woehl, Dean's Representative

Acknowledgements

I would like to express my eternal gratitude to my advisor, Dr. Siddharth Das, for his unconditional support all through my graduate studies. I am also thankful for the computational support provided by the Deepthought2 and the Zaratan High-Performance Computing clusters at the University of Maryland. Finally, I couldn't have done this without you, *Mummy and Papa.*

Table of Contents

Contents

List of Abbreviations

Nanoparticle (NP)

Molecular Dynamics (MD)

Coarse-grained Molecular Dynamics (CGMD)

Excluded Volume (EV)

Mean Squared Displacement (MSD)

Lennard-Jones (LJ)

List of Figures

List of Tables

Chapter 1: Background and Motivation

1.1. Overview

Functionalizing surfaces by grafting polymer molecules (usually using covalent bonds) is becoming increasingly popular because of its potential applications in multiple research fields, such as in chemical sensing, fabrication of hybrid biomimetic materials, tissue engineering, developing soft nanoscale devices, etc. Polymer brushes refer to grafted polymer molecules (with tethering being achieved either through covalent attachment or physical adsorption) that are close enough to each other to ensure that excluded volume interactions enforce these molecules to stretch out (in the form of bristles of a toothbrush) from the grafting surface.[1] Over the last few years, innovative research on polymer brushes has considerably increased its significance in material science and engineering.[2,3] Polymer brushes with variable conformations and structures behave as nanoscale "soft" building blocks capable of bestowing functions[4] – from redox activity to biocompatibility[5,6], tunable wettability[7] to controlled drug delivery[8] and friction control[9] – upon a broad range of materials, enabling a myriad of nanotechnological applications. Several of these applications rely on the fact that the conformation and the structure of polymer brush molecules can be dynamically regulated by a variety of external stimuli (e.g., temperature, pH, salt concentration, etc.).[10]

Molecular dynamics (MD) simulations, which employ the principles of statistical physics to atoms or group of atoms to understand the molecular level behaviors, have been extensively used to probe the behavior of polymer brush molecules. In this thesis, the behavior of the polymer brush grafted

surfaces and their interactions with solvent drops and nanoparticles (NPs) will be explored employing all-atom MD simulations.

1.2. Studying the Wetting Dynamics of Polymer Brush Grafted Surfaces

Regulating the wettability of material surfaces is extremely important for realizing special functionalities for a wide range of applications. Many methods have been developed and employed to control the wettability of material surfaces. The surface-grafted polymer brush technique, as one universal chemical modification strategy, exhibits unique advantages in controlling the surface wettability of materials. Especially, the surface-grafted stimulus–responsive polymer brush technique can offer the unique capability of controllably and reversibly changing the surface wettability, resulting from the dynamic conformation transition of polymer chains under external stimuli.

The behavior of multicomponent macromolecular systems at surfaces can differ significantly from that in the bulk because of preferential affinities of one or more components to the interface or the surrounding media.[11] For example, if we have a multicomponent polymer brush consisting of two distinct polymeric constituents of dramatically different surface energy characteristics, switching the interfacial organization of the polymer layer will lead to changes in wettability. Hence, by treating the surface with solvents selective to only one of the polymer types, rearrangement occurs revealing either the high or low surface energy constituent. This is the reason why a most common strategy for achieving solvent-responsive surfaces is the combination of two moieties with different solubility in the same polymer layer.[12] It is also important to note that by placing two incompatible polymer brushes in close proximity phase separation can occur when the surface is exposed to solvent.[13] For instance, a binary film containing poly(styrene) (PS) and poly(2-

vinylpyridine) (PVP) becomes hydrophobic upon exposure to toluene, θ_{AW} ~90°. This can be attributed to phase separation of the polymer chains since PS preferentially swells in toluene increasing its fraction at the surface. Conversely, the exposure of the film to acidic water, a good solvent for PVP, switches the surface into a hydrophilic state, θ_{AW} ~35°, since polymer rearrangement now brings the charged PVP to the surface.[13] Similarly, Lemieux *et al.* reported a film containing poly (methyl acrylate) (PMA) and poly(styrene-*co*-2,3,4,5,6-pentafluorostyrene) (PSF) brushes exhibiting switchable wettability when exposed to acetone (selective for PMA) or toluene (selective for PSF).[14] After treatment with toluene, the surface becomes enriched with PFS and contact angles of 95°–100° are seen, in line with that for the homopolymer. However, after treatment with acetone, the surface becomes enriched with PMA and excessive surface roughness is also observed: the resulting contact angles are therefore found to be around 117–122°, which is much higher than that seen for the corresponding PMA homopolymer.

1.3. NP-Solvent Interactions with Brush Grafted Surfaces

Introducing nanoparticles (NPs) into a grafted polymer layer gives rise to a wide range of new hybrid materials.[15,16] Such brush-NP systems have broad applications in various fields including sensors, information storage devices, medical diagnostic tools, and catalysts, depending on the combination of the NPs and the polymer brush.[17] The brush-NP hybrids also serve as a model system to study drug delivery.[18] Furthermore, if the polymer brush is responsive to some perturbations or signals, then the hybrid materials can be used as active components to make various “smart” systems.[19]

For a given brush-NP composite, the state of the brush and the distribution of NPs in the brush are critical factors that determine its prospect for particular applications. These considerations have

motivated many experimental studies on controlling the NP distribution and organization in a polymer brush so that certain functions can be realized.[17] The hybrid structure is determined collectively by the strength of the enthalpic NP-polymer interaction,[18] the brush characteristics including grafting density,[19] thickness,[20] pattern,[21-23] composition,[24] and possible gradients of these properties,[25-27] and the solvent being used.[28]

1.4. Grafted Polymer Bilayer Drives Separation and Valving of Binary Mixture Drops

The effort to separate a mixture of highly miscible liquids by enforcing the liquid mixture into a nanoconfinement that imparts distinctly different influences on the liquid has seen significant interest over the past few years (Refs. xxx in Chapter 4). Similar separation of miscible binary liquid mixture that occurs in absence of any confinement but leverages the differences in the volatilities of these two liquids, is popularly known as the distillation and has been practiced for a long time. It is worthwhile to investigate if such distinct influence that drives the separation of a miscible binary mixture can be afforded by making the binary mixture interact with grafted polymeric layers with the polymer showing different influences on the two liquids. If such separation is possible, it would be also possible to repeat the separation procedure using the same system stemming from the possible continuous changes in the swelling of the grafted polymer layers (on interacting with the liquids), thereby providing a dynamically increasing space for the liquids to localize after being separated. The same mechanism can be also utilized for nanoscale valving of liquids, where by changing the state of the swelled polymer layer (by changing the amount of a specific liquid inside the swelled polymer layer), it will be possible to trigger a controlled release (or controlled valving) of another liquid. Nanoscale liquid valves that enable an

on-demand controlled release of very little volume of liquid is of great technological significance and there has been considerable progress in fabricating nanoscopic valves that enable the controlled and *on-demand* release of as little as few molecules of a particular species[29-40] with potential applications in drug delivery,[30-32,37,38] possible treatment of osteoarthritis,[35] corrosion inhibition,[36] etc. On the other hand, investigations probing the design and development of nano-valves that enable the *on-demand* and regulated release of miniscule volume of liquids (e.g., femtoliter-scale liquid volume)[41,42] have been rather scarce. Therefore, this grafted polymer layer driven nanoscale liquid valving, enabling *on-demand* release of desired amount of a given liquid can be of great nanotechnological significance.

For my dissertation thesis, I have studied the interplay of interactions between NP, solvent molecules and the grafted polymer molecules in a variety of systems. I have described below the various MD simulation setups studied for the purposes of this dissertation which is discussed along with subsequent analysis and possible future studies.

Chapter 2: Wetting Driven Globule-to-Brush Transition of Polymer-grafted Surfaces*

Abstract

We employ molecular dynamics (MD) simulations to study the spreading and imbibition of a liquid drop on a porous, soft, solvophilic, and responsive surface represented by a layer of polymer molecules grafted on a solvophilic solid. These polymer molecules are in a crumpled and collapsed globule-like state before the interaction with the drop, but transition to a "brush"-like state as they get wetted by the liquid drop. We hypothesize that for a wide range of densities of polymer grafting (σ_g), the drop spreading is dictated by the balance of the driving inertial pressure and balancing viscoelastic dissipation (associated with the spreading of the liquid drop on the polymer layer that undergoes globule-to-brush transition and serves as the viscoelastic solid). Using the well-known idea that the viscoelastic resisting force exerted by the viscoelastic solid on a spreading drop scales as u^n (where n is the index of the power-law-like rheology of the polymer layer serving as the viscoelastic solid and u is the spreading velocity of the drop on this viscoelastic solid) and considering n=2/3, we show that the scaling calculation recovers the MD simulation prediction of $r \sim t^{1/4}$ and $r_{eq} \sim \sigma_g^{-1/3}$ (where r and r_{eq} are the instantaneous and equilibrium spreading radii). We further describe the wicking behavior of the drop through the polymer layer by appropriately accounting for the manner in which the progressive time-dependent swelling of the grafted polymer molecules provide larger space for the wicking. Third we quantify, possibly for the first time, the temporal dynamics of the "brush" forming process (i.e., capture the dynamics of wetting-mediated globule-to-brush transition). We show that the dynamics of the polymer chain

* Contents of this chapter are published as: Etha, S. A., Desai, P. R., Sachar, H. S., & Das, S. (2021). Wetting Dynamics on Solvophilic, Soft, Porous, and Responsive Surfaces. *Macromolecules*, *54*(2), 584-596.

swelling depends on σ_g and is faster for sparser grafting. Most importantly, we confirm that the height of the relaxed polymer chains approximately scales as $\sigma_g^{1/3}$ confirming the attainment of brush-like configuration by the polymer molecules as they are wetted by the liquid drop. Finally, we argue that our simulations raise the possibility of designing soft and "responsive" and widely deployable liquid-infused surfaces where the polymer grafted solid, with the polymer undergoing a globule-to-brush transition, serving as the responsive "surface".

2.1 Introduction

Studying the behavior of liquid drops on surfaces of various complexities has been critical in designing and fabricating a wide variety of surfaces that demonstrate different wettabilities[46-50] and could be employed in various energy[51-53] and biomedical[54,55] applications as well as applications such as heat transfer enhancement,[56-58] fabrication of anti-biofouling,[59-61] anti-corrosion,[62-64] anti-icing,[65-67] anti-bacterial,[61] and anti-thrombotic[69] surfaces, enhanced oil-water separation,[68,69] and many more. Advancement of computational techniques have enabled a nanoscale exploration of the drop-substrate interactions shedding light on fundamental mechanisms dictating these different interactions as well as enabling designing of surfaces with novel properties.[70-85]

In this study, we employ Molecular Dynamics (MD) simulations to probe the spreading and imbibition (wicking) dynamics of a liquid drop on a solvophilic, porous, soft, and responsive surface. The surface consists of polymer molecules (and therefore behaves as a soft surface) grafted on a solvophilic solid. Initially, the polymers are not in contact with any solvent. This is equivalent to the polymers being in an unfavorable (or a "poor") solvent making them attain

crumpled or collapsed or "globule"-like configuration.[86] Subsequently, when the polymer molecules come in contact with the liquid drop to which they are philic (as we are studying the drop dynamics on a philic polymer layer), the polymer molecules experience a change in solvent from a "poor" (no solvent case) one to a "good" one and accordingly undergo a globule-to-brush (or equivalently collapsed-state-to-brush-state) transition (see Fig. 2.1). This transition represents a swelling/stretching of the polymer molecules in presence of the good solvent: this is similar to the classical globule-to-coil transition,[87-89] with the key difference being the fact that in the present case, the polymer molecules being grafted at close proximity to each other attain a "brush"-like state instead of a coil. As the liquid drop comes in contact with the grafted layer of solvophilic polymer molecules, the drop spreads and wicks through this layer. Therefore, the soft surface behaves as a porous, nanoresponsive ("responsive" over nanoscale), and solvophilic substrate. Such unique substrate characteristic has been achieved by grafting it with polymer molecules undergoing a globule-to-brush transition, as the polymers change from non-wetted to wetted states. There have been prior simulation and experimental studies that have considered imparting different functionalities to a substrate, in terms of its interactions with a liquid drop, by grafting the surfaces with polymer molecules (or polymer brushes).[92-96] The present study adds to that endeavor and studies a unique problem of drop dynamics on a surface that is simultaneously philic, porous, soft, and "responsive" and responds (with the grafted polymers undergoing a globule-to brush transition) to the motion of the drop.

Our results first probe the detailed mechanism of the three simultaneously occurring dynamic processes: the drop spreading, the drop wicking, and the response of the grafted polymer molecules as they transition from non-wetted to wetted states (and undergo a globule-to-brush transition). With regards to the spreading dynamics of the drop, we hypothesize that for a wide

range of densities of polymer grafting (σ_g), a balance of the driving inertial pressure and balancing viscoelastic dissipation drives the spreading. The viscoelastic dissipation is associated with the polymer layer serving as responsive viscoelastic substrate. An average value of n=2/3 (where n is the index of the power-law-like rheology of the polymer layer serving as the viscoelastic solid[83,84]) ensures that the scaling calculation recovers the MD simulation prediction of $r \sim t^{1/4}$ and $r_{eq} \sim \sigma_g^{-1/3}$ (where r and r_{eq} are the instantaneous and equilibrium spreading radii). We also quantify the wicking behavior of the drop through the grafted polymer layer in a manner that takes into consideration the different rate of polymer swelling (and the consequent different rate of availability of the space for wicking) for different grafting densities: such a consideration ensures that the wicking fraction shows similar power law behavior (with time) for different grafting densities. Furthermore, we establish the responsive nature of the surface by quantifying the dynamics of the globule-to-brush transition of the polymer molecules as they come in contact with the liquid drop. It represents one of the earliest attempts to study the time-dependent "dynamics" of how grafted polymer molecules change from globule-like to brush-like states. We establish that the dynamics of the grafted polymer molecules depends on σ_g and that smaller σ_g corresponds to faster dynamics of the grafted polymer molecules. Most importantly, we establish that the final equilibrium height of the wetted polymer molecules approximately scales as $\sigma_g^{1/3}$ confirming the attainment of brush-like configuration by the polymer molecules as they come in contact with the liquid drop. Finally, we argue that this overall process of a drop spreading and wicking into a layer of philic polymer molecules, which themselves undergo a globule-to-brush transition as they change from non-wetted to wetted states coming in contact with the drop, is equivalent to the formation of *soft and responsive* liquid-infused surfaces (LISs),[99-106] where the rigid substrate grafted with the responsive (undergoing globule-to-brush transition) polymer layer serves as the

"surface" part of the LISs. While polymer brushes and grafted polymer layers have been extensively studied for a variety of difference applications over the past several decades, to the best of our knowledge, this is the first time that the grafted polymer molecules and their ability to transition from "globule" to "brush" state in presence of the appropriate solvent has been leveraged to conceptualize the design of LISs.

In summary, therefore, our paper sheds light on the following fundamental and applied issues. First, it is possibly one of the first studies that probes the simultaneous spreading and wicking of a liquid drop on a soft substrate. Drop spreading dynamics on soft surfaces have been extensively studied; however, these studies have always considered an impenetrable soft solid. Here on the contrary, we consider the drop spreading on such a soft surface that also allows for drop wicking. In fact, this wicking eventually leads to a complete mixing between the imbibing drop and the polymer layer (with the drop and the polymer layer being chemically identical). Previous studies[76,77] probing the interaction of polymer melt droplet with a layer of chemically identical polymer brushes have predicted the attainment of such completely mixing state at equilibrium: we use the scaling calculations provided in these studies[107,108] to confirm the validity of the attainment of such complete mixing state with our chosen set of parameters. Second, we discover that the spreading dynamics obeys behavior that is similar to the case when the drop spreads on a soft and viscoelastic solid and the drop spreading is balanced by the balance of the capillary pressure and the viscoelastic resistance (imparted on the drop by the viscoelastic solid). Therefore, we hypothesize that the layer of the grafted polymer molecules that undergo a "globule-to brush" transition serves as a viscoelastic solid. Third, to the best of our knowledge, this is also an example where the drop spreading and imbibition occurs on a soft substrate that "alters" its configuration in contact with the incoming liquid from the drop. In other words, this study represents one of the

first examples of drop spreading on a substrate that is not only soft, viscoelastic, and porous but also responsive and dynamic (i.e., undergoes a time-dependent transition). Finally, these specific interplays of the drop and the substrate enable us to conceptualize a system where a substrate grafted with a layer of responsive polymer molecules can serve as the “surface” of a novel design of an LIS.

2.2 Computational Methods

We study the dynamics of a polymeric liquid drop (octane) interacting with solvophillic (i.e., philic to this liquid drop) grafted polymer molecules (considered as simple alkanes) grafted on a solvophillic substrate by performing Molecular Dynamics (MD) simulations carried out using the LAMMPS software package with a united-atom model.[109] We consider an infinitely long cylindrical 2D drop and accordingly choose a significantly smaller box width. The simulation box dimensions are $x \times y \times z = 3500\text{Å} \times 50\text{Å} \times 650$ Å, with a much smaller y-dimension. The simulation domain is periodic in both the x and y directions, but not in the z-direction, where a fixed boundary condition is implemented.

As mentioned earlier we use a united-atom model for both the grafted polymer layer as well as the polymeric drop. We choose a simple alkane with 40 monomers as our grafted polymer molecules while the liquid drop is octane (8 monomer units). A uniform reflective wall is placed at the top of the simulation domain to prevent the liquid molecules from escaping. We use α-quartz, which is a polymorph of silica, as our solvophillic substrate. Silica has been shown to be extremely philic (contact angle, $\theta \sim 0^o$) to most *n*-alkanes,[110] and we tested this with our MD simulations as well. Our simulations confirmed that in the absence of the grafted polymer molecules, hexane formed a thin film on the quartz substrate verifying the philicity of quartz towards hexane.

The grafted polymer molecules as well as the polymeric liquid drop are modelled using the OPLS-UA force field known to predict the properties of alkanes accurately.[111] A previous study on ethane liquid-vapor interface by Taylor and Shields[112] using OPLS-UA as well as OPLS-AA (all-atom force field) found that the calculated surface tensions for OPLS-UA force field were in qualitative agreement with experimental data. More recently, da Silva et al.[113] conducted a comprehensive

study of the most common all-atom and united-atom force fields for the description of liquid properties of alkanes. They observed that OPLS-UA performed better than most other force fields for the calculated values of surface tension (of n-octane) (only being outperformed by GROMOS) as well as for the values of interfacial tension (of n-octane with water). They also concluded that among the force fields considered in their work, the united atom models perform better than the all-atom models for n-alkanes. Under these circumstances, we believe that the choice of OPLS-UA should give us qualitatively accurate results. The bonded and the non-bonded interaction parameters for the grafted polymer molecules and the liquid drop have been obtained from the OPLS database. On the other hand, the quartz substrate is modelled using the TraPPE-zeo force field.[114] We do not consider any Columbic interactions in our system (since most of the species are uncharged and we also neglect the effect of partial charges on quartz). Furthermore, the non-bonded interactions in our system only include a shifted-truncated 12-6 Lennard Jones (LJ) potential with a cutoff of 13 Å. For the interactions between the liquid drop and the grafted polymer molecules as well as interactions between the substrate and the polymeric species (liquid drop as well as the grafted polymer molecules), we use the Lorentz-Berthelot mixing rules.

The simulations are carried out in an NVT ensemble using the Nosé-Hoover thermostat.[115,116] All simulations are performed with a timestep of 2 fs and the relaxation time of the thermostat is considered to be 100 timesteps (200fs). We start the simulation with the temperature of all the particles set at T=0 K, and gradually increase the temperature to 300 K, while keeping the liquid drop fixed at a large enough distance away from the grafted polymer molecules so that their interactions are negligible. We then displace the drop in the negative z-direction to bring the drop closer to the grafted polymer molecules. The droplet is displaced to a height of 15 Å above the polymer layer and is then allowed to freely interact with the grafted polymer molecules to begin

the wetting process. As a result, drop undergoes spreading and imbibition (on the grafted polymer layer) and attains an equilibrium configuration. Subsequently, we run the simulations for another 4 ns to ensure that the overall system has equilibrated. This additional simulation time is necessary for allowing the longer alkane chains of the polymer molecules attain equilibrium after the liquid drop (consisting of smaller octane molecules) have already equilibrated. Usually, grafted polymer molecules take a few hundred τ_{LJ} to equilibrate,[117] where τ_{LJ} is the characteristic LJ timescale defined as $\tau_{LJ} = \sqrt{\frac{m\sigma^2}{\varepsilon}}$, where m is the mass of the monomers of the grafted polymer molecules and σ and ε are the corresponding distance and energy parameters associated with the LJ interaction potential for the monomers. For our case, for n-alkane $\tau_{LJ} \approx 4\,ps$, implying that we use an equilibration time of at least $1000\tau_{LJ}$ (i.e., 4 ns), which is sufficient to ensure the equilibration of the grafted polymer molecules. The liquid drop, on the other hand, consists of smaller chains of the same polymer (octane), implying it requires a shorter duration for equilibration. We shall like to point out here that we employ the stability of the height of the polymer layer (i.e., the height of the polymer layer does not change significantly with time) as the criterion to determine equilibration of the polymer molecules. This also requires that the drop spreading stops and that the drop attains an equilibrium state, confirmed by ensuring that the drop contact radius and the drop contact angle attain an equilibrium value. In order to further quantify equilibration, we calculate the autocorrelation function, $C_e(t) = \frac{\langle (h(t)-\langle h\rangle)(h(0)-\langle h\rangle)\rangle}{\langle h^2\rangle-\langle h\rangle^2}$ (where $\langle h\rangle$ denotes the mean value of the brush height) for the average brush height. Fig. A.5 in Appendix A provides the variation of the autocorrelation function of the average brush height for all grafting densities. From Fig. A.5, we can quantify the corresponding autocorrelation time scale to be less than 50ps for all grafting densities, which implies that an equilibration time of 4 ns should be sufficient for statistical

sampling. We collect data every 2ps, ensuring that most of the dynamics are captured. We carry out simulations with four different grafting densities (σ_g) of the polymer chain. σ_g is defined as the number of chains grafted per unit area of the substrate. Usually, we represent it in terms of the number of polymer chains per σ^2 area of the substrate, where σ = 3.905 Å is the LJ distance parameter for the methyl group on the polymer chain. For example, the grafting density for an inter-chain separation of l=12 Å would be given as $\sigma_g = 3.905^2/12^2 \times 1/\sigma^2 \approx 0.1/\ \sigma^2$. Also, all the visualizations of the atomic trajectories are performed using the open-source software OVITO.[118]

2.3 Results

Figs. 2.1(a-d) provide the MD simulation snapshots for describing the wetting behavior of a cylindrical LJ drop of octane on the solvophilic grafted alkane polymer layer for a grafting density $\sigma_g=0.1/\sigma^2$. We observe that the liquid penetrates the polymer chains while spreading, indicating the attainment of the *mixing wetting state* as described by Mensink *et al.*[94] The occurrence of spreading is confirmed by noting a progressive increase in *D*, which is the contact diameter (twice the contact radius *r*). Also, the snapshots for the later time instants clearly show the penetration/imbibition/wicking of the liquid molecules within the grafted polymer layer. As the liquid drop comes in contact with the polymer molecules, which are in a crumpled and globule-like state in absence of the drop, the polymer molecules transition to a brush-like state (as confirmed later, see Fig. 2.6, by showing that the height of the grafted polymer molecules approximately scale as $\sigma_g^{1/3}$).[119] We elucidate this exact transition by providing the "zoomed" in views of the time response of some of the chosen grafted polymer molecules [see Figs. 2.1(e-f)]. For a clearer visualization, we do not show all the polymer molecules along a given length of the solid surface; rather we show only a selected few. As expected, these molecules are in a crumpled, globule-like state initially, i.e., when the drop is yet to come in contact with them. However, over time, as the drop penetrates more and more into the polymer layer (this extent of penetration can be observed by noting to what extent the liquid front crosses the black line that provides the instantaneous average height of the grafted polymer molecules), the grafted polymer molecules sense the presence of a "good" solvent in its vicinity and stretch out to form the brushes. This crumpled-state-to-brush-state transition is even clearly manifested in Figs. 2.1(i-l), where we simply provide the snapshots showing the configuration of one single grafted molecule. In Fig. A.1 in Appendix A, we provide the same set of MD simulation snapshots describing the spreading

and wicking of the liquid drop as well as the globule-to-brush transition of the grafted polymer molecules for another grafting density value ($\sigma_g=0.31/\sigma^2$). For this case too, we observe that the

liquid penetrates the polymer chains while spreading, thereby giving rise to the *mixing wetting state*.

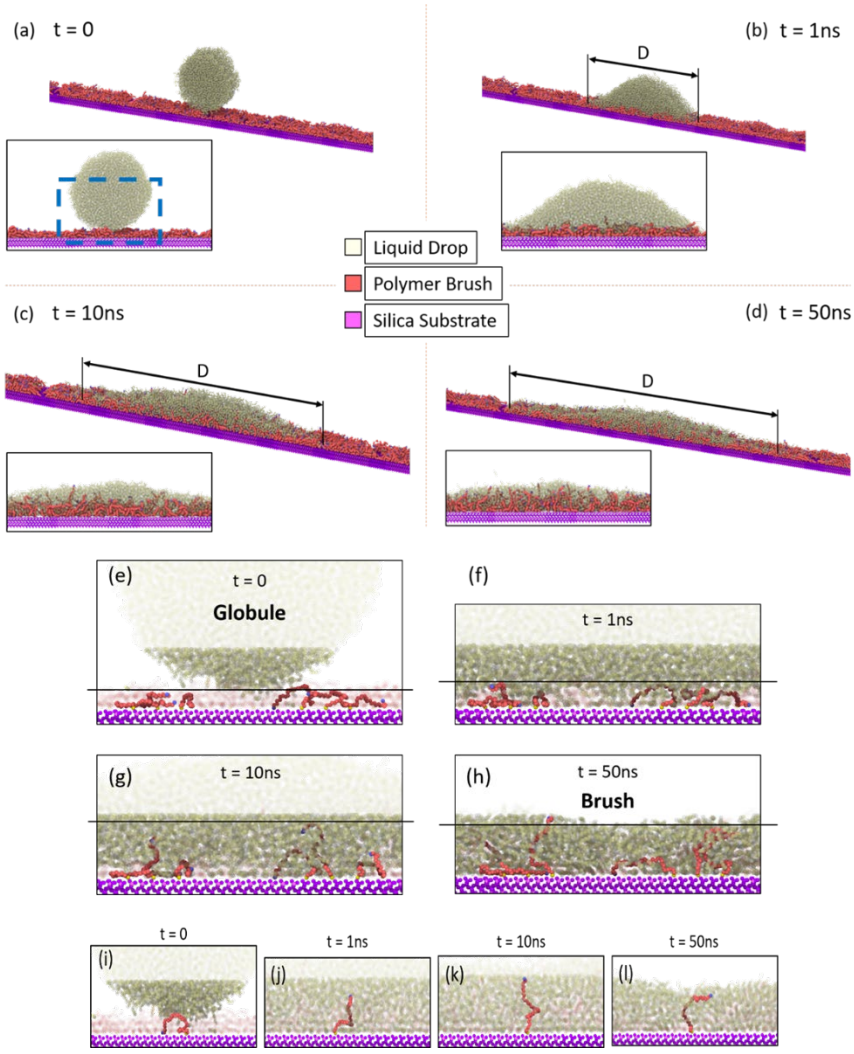

Figure 2.1. (a-d) MD simulation snapshots showing the interaction of the polymeric liquid drop with the layer of grafted polymer molecules (grafting density $\sigma_g = 0.1/\sigma^2$) at different time instants (identified on top of each snapshot). For these figures, the interaction is shown by depicting the entire length of the layer of the grafted polymer molecules. In the inset of these subfigures, we highlight a smaller section of the layer of the grafted polymer molecules providing a more detailed view of the solvent-polymer-molecule interface. The simultaneous spreading and wicking of the liquid molecules (inside the layer of the grafted polymer molecules) become apparent from these snapshots. In subfigures (a-d), *D* represents the contact diameter. (e-h) Zoomed MD simulation snapshots showcasing the behavior of the liquid molecules and the grafted polymer molecules corresponding to the region highlighted in (a) for different time instants (identified on top of each snapshot). These snapshots show that as the liquid penetrates more and more into the polymer layer (the extent of this penetration is represented by noting the location of the liquid front with respect to the black line that provides the instantaneous average height of the grafted polymer molecules), the polymer molecules swell and stretch out to take the form of brushes (the fact that they attain brush-like configuration is established in Fig. 2.6). For a clearer visualization, we do not show all the polymer molecules along a given length of the solid surface; rather we show only a selected few. (i-l) Zoomed MD simulation snapshots showcasing the behavior of a single grafted polymer molecule undergoing a crumpled-state-to-brush-state transition over time (the respective times are identified on the top of the snapshots).

We next quantify the spreading dynamics of the liquid drop as it comes in contact with the soft and responsive surface. Fig. 2.2(a) provides the contact radius (r) of the liquid drop as a function of time (t) for different grafting densities of the polymer chains. Regardless of the grafting densities, we recover a $r \sim t^{1/4}$ variation (from a fit to the MD simulation results), except at early times of spreading. This is a stark variation from the conventional power laws associated with the spreading of drops on solid substrates, where one witnesses $r \sim t^{1/2}$ (for the early inertial regime;[70,83,120] for the MD simulation of drops this is the only regime that gets manifested[70,83]) and $r \sim t^{1/10}$ (for the late viscous regime with the drop spreading obeying the Tanner's Law; this behavior is reproduced in experiment and scaling calculations).[121,122] Here we provide a detailed scaling calculation for describing this spreading process exhibiting $r \sim t^{1/4}$. For drop spreading, the key driving force is the capillary pressure (p_{cap}),[70,83] expressed as:

$$p_{cap} \sim \frac{\gamma R}{r^2}, \quad (1)$$

where γ is the liquid drop surface tension, R is the drop radius, and r is the contact radius. The r-vs-t scaling depends on the force that balances this driving capillary pressure. For the drop in the inertial regime the inertial pressure ($p_{intertial}$) balances this capillary pressure. Following Refs. 70 and 83, we can express $p_{interial}$ as (with $u=dr/dt$ being the spreading velocity):

$$p_{interial} \sim \rho u^2 \sim \rho \left(\frac{dr}{dt}\right)^2. \quad (2)$$

Balancing p_{cap} with $p_{inertial}$, we can write:

$$p_{cap} \sim p_{interial} \Rightarrow \frac{\gamma R}{r^2} \sim \rho \left(\frac{dr}{dt}\right)^2 \Rightarrow rdr \sim \left(\frac{\gamma R}{\rho}\right)^{1/2} dt \Rightarrow r^2 \sim \left(\frac{\gamma R}{\rho}\right)^{1/2} t \Rightarrow r \sim \left(\frac{\gamma R}{\rho}\right)^{1/4} t^{1/2}. \quad (3)$$

Therefore, in the inertial regime $r \sim t^{1/2}$ – as already pointed out, for MD simulations of drops spreading on rigid solids, this is the only regime that has been witnessed.[70,83]

On the other hand, if the viscous and viscoelastic resistances become the dominant resistance mechanisms (balancing the driving capillary pressure), we shall get different scaling predictions. The viscous dissipation force scales as u (this dissipation occurs due to the liquid motion within the spreading drop),[123,124] while the viscoelastic force scales as u^n (this dissipation occurs with the drop interacting with the solid that is soft and viscoelastic; also n is an exponent that is typically less than unity).[97,98,123,124] Therefore, by balancing the driving capillary pressure with the viscous force per unit area (expressed as $\sim K_1 u$, where K_1 is a constant), we can obtain:

$$\frac{\gamma R}{r^2} \sim K_1 u \Rightarrow \frac{\gamma R}{r^2} \sim K_1 \left(\frac{dr}{dt}\right) \Rightarrow r^2 dr \sim \left(\frac{\gamma R}{K_1}\right) dt \Rightarrow r^3 \sim \left(\frac{\gamma R}{K_1}\right) t \Rightarrow r \sim \left(\frac{\gamma R}{K_1}\right)^{1/3} t^{1/3}. \quad (4)$$

On the other hand, by balancing the driving capillary pressure with the viscoelastic resisting force per unit area (expressed as $\sim K_2 u^n$, where K_2 is a constant), we can obtain:

$$\frac{\gamma R}{r^2} \sim K_2 u^n \Rightarrow \frac{\gamma R}{r^2} \sim K_2 \left(\frac{dr}{dt}\right)^n \Rightarrow r^{\frac{2}{n}} dr \sim \left(\frac{\gamma R}{K_2}\right)^{\frac{1}{n}} dt \Rightarrow r^{\frac{2}{n}+1} \sim \left(\frac{\gamma R}{K_2}\right) t \Rightarrow r \sim \left(\frac{\gamma R}{K_2}\right)^{\frac{1}{2+n}} t^{\frac{n}{2+n}}. \quad (5)$$

For n=2/3, eq.(5) yields $r \sim t^{1/4}$, which is the scaling behavior resulting from the fit to the MD simulation results.

In Fig. 2.2(b), the equilibrium contact radius (r_{eq}) attained by the drop at the end of the spreading is plotted as a function of the grafting density (σ_g). Interestingly, r_{eq} decreases with an increase in σ_g. The viscoelastic resistance force (per unit area), can be expressed as:[98,123,124]

$$f_{viscoelastic} \sim \left(\frac{u}{u^*}\right)^n, \quad (6)$$

where u^* is the characteristic velocity that scales as:[97]

$$u^* \sim G^{-1}. \quad (7)$$

Here G is the static shear modulus, which for a layer of grafted polymer brushes (this is the final state of the grafted layer) scale with the polymer brush grafting density (σ_g) as:[125]

$$G \sim \sigma_g^p. \quad (8)$$

For a perfectly wetted brush, we have p=2 (see Ref. 125). However, for the present case, we consider a liquid drop, which although enforces the grafted polymer molecules to approximately brush-like states, causes an issue of undersaturation (see the **DISCUSSIONS** section later). Accordingly, as a conservative estimate, we consider a generic value of p with $1 < p \leq 2$.

Considering $f_{viscoelastic} \sim K_2 u^n$ and eqs.(6-8), we can write:

$$K_2 \sim (u^*)^{-n} \sim G^n \sim \sigma_g^{pn}. \quad (9)$$

Therefore, using eq.(9) in eq.(5) and using the condition that when the drop is in equilibrium (i.e., $r=r_{eq}$) the grafted polymer molecules are in brush-like state (such that $G\sim\sigma_g^p$, with $1 < p \leq 2$), we can write:

$$r_{eq}\sim\left(\frac{\gamma R}{\sigma_g^{pn}}\right)^{\frac{1}{2+n}} \Rightarrow r_{eq}\sim\sigma_g^{-\frac{pn}{2+n}}. \quad (10)$$

With n=2/3 and p=4/3, eq.(10) yields:

$$r_{eq}\sim\sigma_g^{-1/3}, \quad (11)$$

i.e., we perfectly recover the scaling behavior resulting from the fit to the MD simulation results [see Fig. 2.2(b)].

The above scaling calculations rely on expressing the viscoelastic resistance imparted on the drop to be proportional to u^n. Such a consideration has been widely accepted through the works of Shanahan and co-workers in the nineties[123,124] and Snoeijer and co-workers[97,98] in recent times. Both these groups successfully verified such a behavior by theory and experiments. The second critical issue is the choice of n. Karpitschka *et al.* pointed out that n is a measure of the power law rheology of the viscoelastic substrate with $G''(\omega)\sim\omega^n$ for the substrate (where G'' is the loss modulus of the viscoelastic solid and ω is the frequency).[83] They also pointed out that for typical soft and viscoelastic gels, $n< 1$ with values ranging between ½ and 2/3. Shanahan and co-workers also pointed to n value that can be in the similar range.[123] Therefore, we can infer that while it is not entirely possible to predict the exact rheology of the responsive grafted polymer system, considering it to be a viscoelastic solid with n=2/3 is not too unrealistic a choice. Finally, we provide a physical argument supporting the consideration of the grafted and responsive polymer

layer as a viscoelastic solid in the context of the spreading of the liquid drop. A spreading liquid drop is considered to be subjected to a viscoelastic resistance from a solid if the solid itself undergoes some configurational changes on account of the force exerted by the moving drop contact line. For example, Karpitschka *et al.* showed that a liquid drop moving on a viscoelastic solid significantly deforms the solid and that deformation, coupled with the thickness of the viscoelastic solid, dictates the attraction or repulsion of two adjacent drops.[98] In another study, Karpitschka *et al.* showed that for a single drop, the ridge formed on the solid due to the surface tension pull from the liquid contact line migrates as the drop migrates (with a contact line velocity u) and the "tilt" of the ridge scales as u^n.[97] In the present study, the solid being composed of the responsive polymer layer is affected and deformed by the drop spreading (at every stage of the spreading) and therefore, we can hypothesize such a grafted and responsive polymer layer as a representative viscoelastic solid.

As a part of probing the drop dynamics, we also provide the time variation of the drop dynamic contact angle as it spreads on the polymer-grafted substrate for different grafting densities [see Fig. 2.3(a)]. The extreme philicity of both the grafted polymer molecules and the solid grafting substrate ensures that for all the grafting densities, the dynamic contact angle of the spreading drop decreases very quickly and attains an extremely small equilibrium value θ_{eq} (of only a few degrees). In Fig. 2.3(b), we provide the variation of θ_{eq} as a function of σ_g. At equilibrium, for very small θ_{eq}, approximating the drop profile as a cylindrical cap, we could write (with V_{cap} being

the volume of the cylindrical cap, which is constant and is identical to the volume of the liquid drop, and h_{eq} being the equilibrium drop height with h_{eq}<<r_{eq}):

$$V_{cap}\sim h_{eq}r_{eq}^2\left[3+\left(\frac{h_{eq}}{r_{eq}}\right)^2\right]\sim h_{eq}r_{eq}^2\sim\left(1-cos\theta_{eq}\right)r_{eq}^2\sim\theta_{eq}^2r_{eq}^2\Longrightarrow\theta_{eq}\sim r_{eq}^{-1}. \quad (12)$$

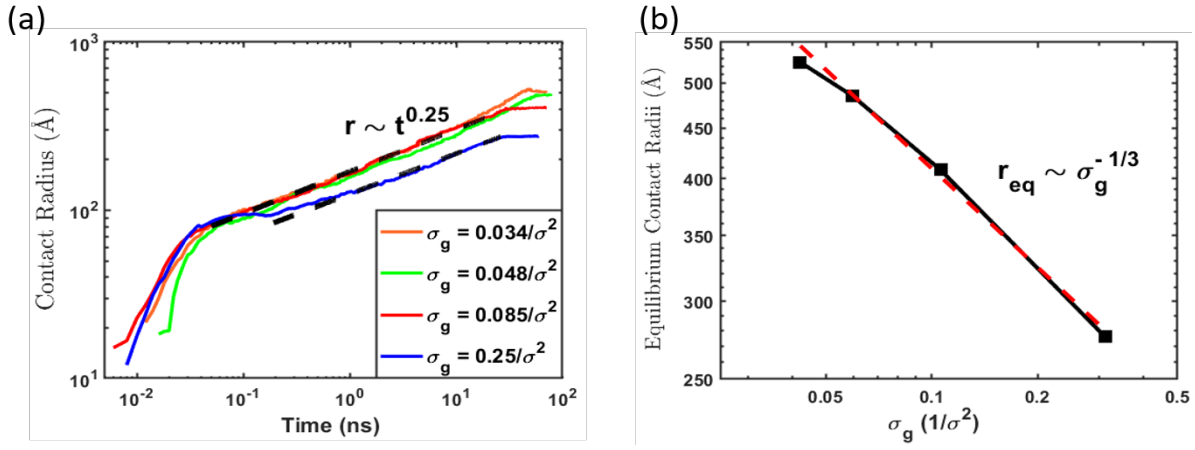

Figure 2.2. (a) MD simulation results showing the dynamics of drop spreading by quantifying the variation of the contact radius r with time for different values of the grafting density (σ_g). The fitting to the MD simulation results, showing $r\sim t^{1/4}$ is shown by dashed lines. The scaling calculations, considering that the drop spreading is governed by the balance of the driving capillary pressure and the resulting viscoelastic dissipation yields the same scaling behavior if one considers the exponent (dictating the viscoelastic rheology of the solid) as n=2/3. (b) MD simulation results showing the variation of the equilibrium contact radius r_{eq} with the grafting density (σ_g). A fit to the MD simulation result, yielding $r_{eq}\sim\sigma_g^{-1/3}$, is shown by the dashed line. The scaling calculations, with n=2/3, reproduces this behavior.

Eq.(12) explains the reason for which we observe $\theta_{eq}\sim\sigma_g^{1/3}$ by fitting the results from the MD simulations [see Fig. 2.3(b)], given that one obtains $r_{eq}\sim\sigma_g^{-1/3}$ [from the fitting of the MD simulation results, see Fig. 2.2(b) as well as from the scaling calculations (see above)].

In order to confirm that in its final equilibrium wetting state, the liquid retains its "drop-like" configuration, in Fig. A.4 (see Appendix A) we depict only the droplet as it spreads over the

substrate grafted with the polymer chains. In this visualization, the polymer chains are "turned off" to make them invisible, although the spreading still occurs in their presence. This allows us to understand the drop spreading more clearly. The subfigure S4(c) depicts the equilibrium structure of the drop, and although the contact angle is quite small (only a few degrees), the drop configuration is still preserved (and we do not encounter a liquid film). The contact angles are calculated using curve-fitting through the edge of the 2D drops and although it is true that the individual polymer molecules of the liquid droplet and the grafted polymer molecules show relatively large fluctuations in their positions and heights respectively, the contact line is pinned (fixed in position) at equilibrium, and so the contact angles determined using curve-fitting attain a stable value at equilibrium. Of course, these equilibrium contact angles are small since the polymer molecules are extremely solvophilic, and so they look indistinguishable. However, we use 3-Å-wide vertical bins and the resolution of this method for the drops in our study is less than 0.5º (the exact value depends on equilibrium radius of the drop). Accordingly, the drop equilibrium contact angle, which is still much larger than this resolution, can be easily captured.

Finally, it can be noted that the results from the scaling argument deviate from the MD simulation results at low grafting densities (this is especially apparent in the variation of the contact radius). Our scaling arguments assume that the grafted polymer layer behave as a continuous soft deformable surface (with a finite shear modulus) on which the drop spreads and imbibes. However, at very small grafting densities, the inter-chain separation becomes so large that the continuum description of the grafted polymer layer starts to break down, causing this difference between the results from the scaling arguments and the MD simulation results.

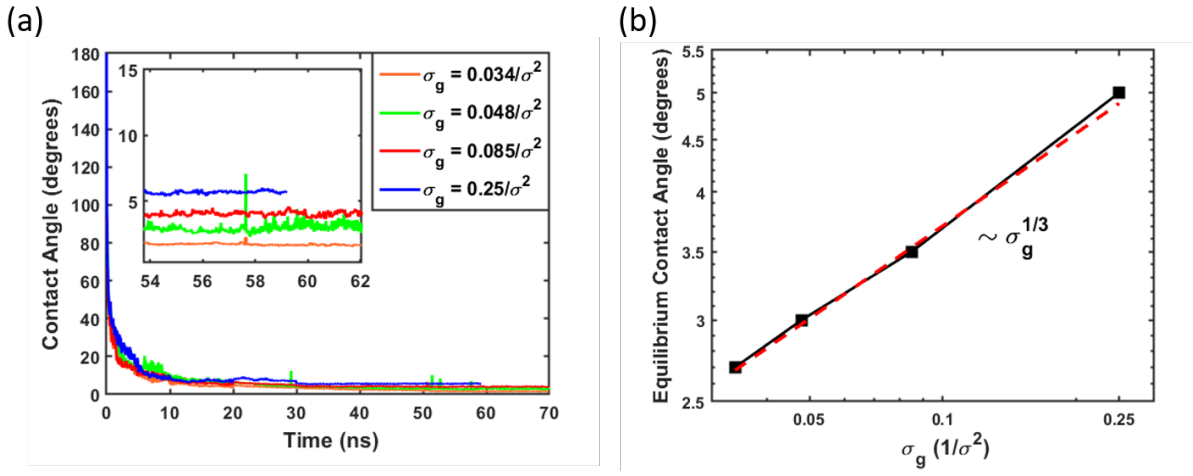

Figure 2.3. (a) MD simulation results showing the dynamics of drop spreading by quantifying the variation of the dynamic drop contact angle θ with time for different values of the grafting density (σ_g). In the inset of the figure, we zoom the variation of θ corresponding to the later time instants of the spreading process. (b) MD simulation results showing the variation of the equilibrium contact angle θ_{eq} with the grafting density (σ_g). A fit to the MD simulation result yielding $\theta_{eq} \sim \sigma_g^{1/3}$ is shown by the dashed line.

The drop, other than wetting, also exhibits imbibition into the soft substrate as it spreads. The imbibition occurs simultaneously with the swelling of the polymer chains. In order to characterize this behavior, we first determine the instantaneous number density of the drop liquid molecules [$n_{wk}(t)$] that have imbibed/wicked into the grafted polymer layer (that itself is undergoing swelling) within a region that is x_{wk} =10-nm wide and localized below the drop and around the drop center [shown in fig. 2.4(a)]. $n_{wk}(t)$ is computed as the ratio of the instantaneous total number of the drop liquid molecules [$N_{wk}(t)$] that have imbibed/wicked into the grafted polymer layer within the above-identified region (see section A.2 in Appendix A for the specifics of how the imbibed/wicked drop liquid molecules are identified) to the instantaneous average volume of the grafted polymer layer (of the above-identified region). This average volume is the product of the

instantaneous average height $h(t)$ of the polymer layer and the cross-sectional area ($x_{wk} \times y_b$, where y_b is the dimension of the simulation box in y direction). Therefore, we can write:

$$n_{wk}(t) = \frac{N_{wk}(t)}{h(t) x_{wk} y_b}. \quad (5)$$

Similarly, we define the maximum number density n_{wk0} (or steady state number density) of the imbibed liquid within this same region that is x_{wk} =10-nm wide and localized below the drop and around the drop center [shown in fig. 2.4(a)] as:

$$n_{wk0} = \frac{N_{wk0}}{h_0 x_{wk} y_b}. \quad (6)$$

where N_{wk0} is the total number of liquid molecules that have imbibed/wicked into the grafted polymer layer (within the above identified zone) and h_0 is the final average equilibrium height of the grafted polymer layer (of the above identified zone). Finally, we quantify the wicking by defining a *wicking fraction*, which is the ratio of these quantities, i.e.,

$$Wicking\ Fraction = \frac{n_{wk}}{n_{wk0}}. \quad (7)$$

In Fig. 2.4(b), we provide this wicking fraction for various grafting densities. We observe that for all the values of the grafting density, the wicking fraction scales as $t^{0.25\pm0.02}$, as obtained from fitting the MD simulation results. An increase in the grafting density leads to a much slower rate of swelling of the polymer molecules (see Fig. 2.5). This would imply that the rates of the availability of the volume through which the drop molecules can wick get reduced with an increase in the grafting density. Therefore, defining the wicking fraction on the basis of the number density of the wicked drop molecules that accounts for the initial height of the grafted polymer molecules (which

signifies the space available to the liquid drop molecules for imbibition/wicking) ensures the wicking fraction shows a scaling behavior with time that is independent of the grafting density.

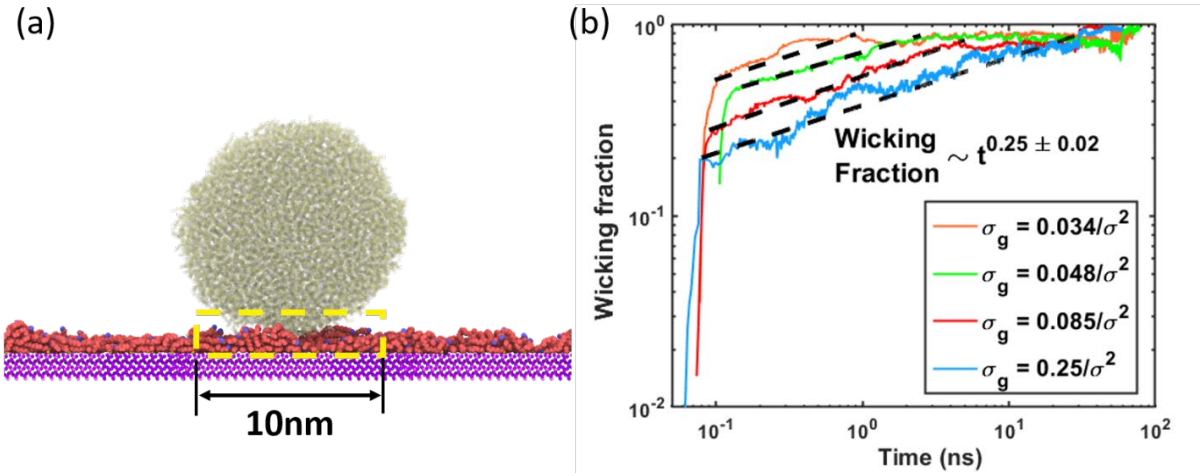

Figure 2.4. (a) MD simulation snapshot depicting a section of the system and identifying the length x_{wk}=10 nm of the region (around the drop center) where we study the wicking behavior inside the layer of grafted polymer molecules. (b) MD simulation results showing the dynamics of drop imbibition into the layer of grafted polymer molecules by quantifying the wicking fraction (defined in eq. 7) with time for different values of the grafting density (σ_g). A fit to the MD simulation result yielding $Wicking\ fraction \sim t^{0.25\pm0.02}$ is shown in the figure by the dashed lines.

In order to complete the picture, we finally quantify the responsiveness of the substrate itself, i.e., the grafted polymer layer as it transitions from a globule-like state to a brush-like state. In Figure 5, we quantify the time response of the average height of the grafted polymer molecules for the molecules present within the region that is x_{wk} =10-nm wide and localized below the drop and around the drop center [shown in fig. 2.4(a)]. Section S.2 in the SI provides more details of this quantification process. It can be noted that the grafted polymer molecules experience a quick increase in their height initially, owing to the sudden availability of a favorable medium, followed

by a gradual decrease in height before reaching an equilibrium value. The decrease in the height of the polymer molecules in this central location (i.e., the region that is x_{wk} =10-nm wide and localized below the drop and around the drop center, see Fig. 2.5a) is due to the fact that as the drop spreads, the amount of liquid available to interact with the polymer molecules at this central location decreases leading to a dearth of liquid around the polymer chains at this central location. As an inset to the figure, the log-log plot of the brush height is presented along with the scaling of the brush height as it transitions from a globule-like to a brush-like state. We observe that for early stages of polymer chain stretching, the time-dependent polymer stretching obeys a power-law like behavior, with the instantaneous height of the grafted polymer molecules scaling as t^{δ}. A decrease in the grafting density leads to a larger δ, indicating a faster polymer stretching for a less dense brush. This is intuitive given the fact that sparsely grafted chains are freer to deform and stretch than denser ones. The polymer chains with lower grafting density experience a lower inter-chain attraction and hence can be swollen easily by the introduction of a favorable environment (i.e., by wetting the grafted polymer molecules by a liquid to which the molecules are philic). Finally, and most importantly, in Fig. 2.6 we demonstrate that the final equilibrium height of the stretched polymer chains approximately scale as $\sigma_g^{1/3}$. This confirms that the stretched polymer molecules indeed attain a brush-like configuration,[88] as they get wetted by the spreading and imbibing liquid drop.

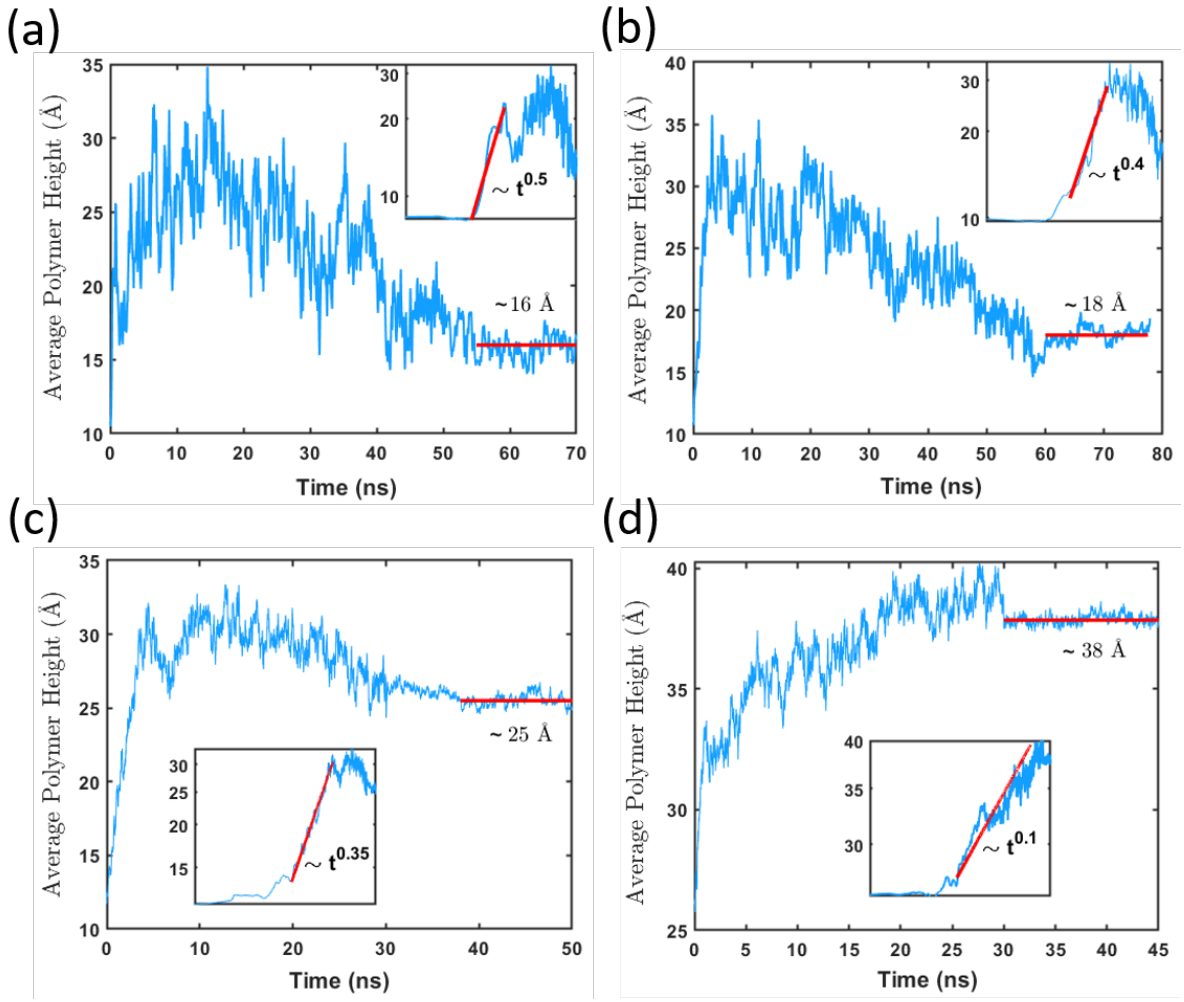

Figure 2.5. MD simulation results showing for the dynamic response of the polymer molecules (representing the "responsiveness" of the substrate) by quantifying the time-dependent variation of the average height of the grafted polymer molecules for (a) $\sigma_g = 0.04/\sigma^2$, (b)$\sigma_g = 0.06/\sigma^2$, (c) $\sigma_g = 0.1/\sigma^2$, and (d) $\sigma_g = 0.31/\sigma^2$. For each of these figures we provide the final equilibrium value of the height of polymer molecules. Furthermore, in the inset of each of the figures, we quantify the "power"-law like ($\sim t^{\delta}$) increase in the height of the grafted polymer molecules at the early stages of the dynamic process. We identify that $(\delta)_{\sigma_g = 0.04/\sigma^2} = 0.5$ [see (a)], $(\delta)_{\sigma_g = 0.06/\sigma^2} = 0.4$ [see (b)], $(\delta)_{\sigma_g = 0.1/\sigma^2} = 0.35$ [see (c)], and $(\delta)_{\sigma_g = 0.3/\sigma^2} = 0.1$ [see (d)].

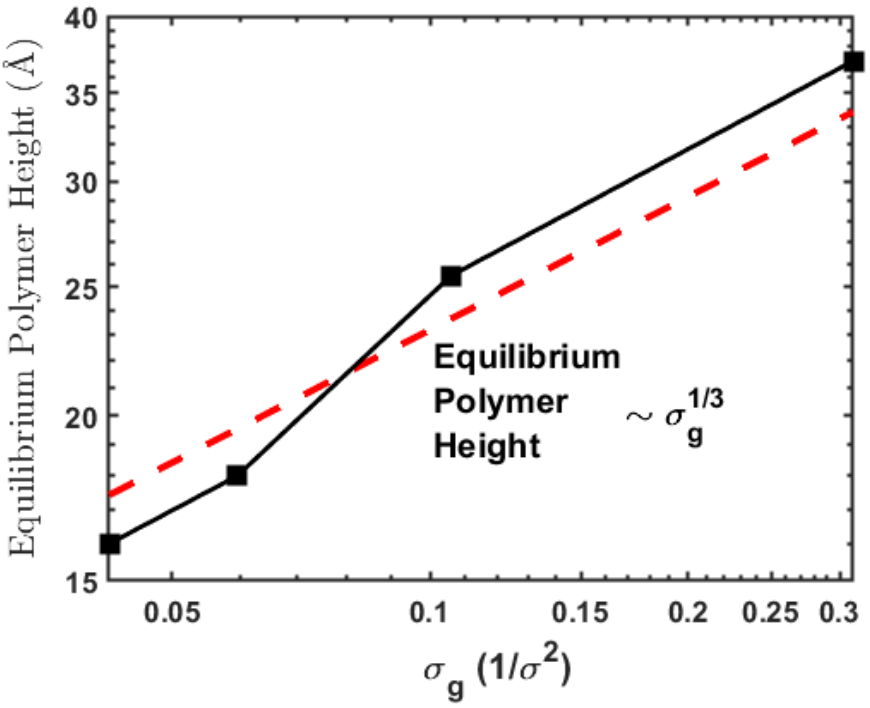

Figure 2.6. MD simulation results quantifying the average equilibrium height of the grafted polymer molecules (this equilibrium height is quantified in Fig. 2.5) as a function of the grafting density. An approximate fit (shown by a dashed line) confirming that this height scales as $\sigma_g{}^{1/3}$is recovered establishing that the swollen grafted polymer molecules (after being wetted by the liquid drop) attain a brush-like configuration.

Finally, we shall like to discuss the relevance of this study in designing novel, soft and responsive liquid-infused surfaces and coatings.[99-106] These liquid-infused surfaces and coatings typically consist of a thin and conformal lubricating layer of a liquid that wets the solid surface, with the solid surface typically being either corrugated or pillar or fiber-like providing spaces for the liquid to impregnate. This lubricating liquid should be strongly philic to the substrate and when that is not the case, chemical modification of the solid surface is conducted to ensure that it becomes philic to the liquid.[126] In this context, the present study can be considered to represent a design of such *liquid-infused* surface or coating: the final liquid-imbibed equilibrium state of the system represents a structure [see Fig. 2.1(d) and its inset] that is very similar to a standard *liquid-infused*

surface or coating with the liquid of the drop serving as the "lubricating liquid", while the quartz substrate grafted with a layer of polymer serving as the "surface" that is responsive. The detailed quantifications proposed in this study, e.g., the equilibrium radius of the drop (which signifies the extent of wetting of the "surface" by the "liquid" in our hypothesized liquid-infused surface), the time dependent spreading and wicking behaviors (which signify how fast the fabrication of the liquid-infused surface occurs), and the time dependent response of the polymer molecules (which signify the "responsiveness" of the "responsive" surface) enable a nanoscopic quantification of designing a liquid-infused surface or coating. Earlier MD simulation studies have probed the dynamics of a liquid drop interacting with a pre-existing liquid-infused surface;[75,76] however, these studies have not considered the nanoscale dynamics associated with the formation of a soft and responsive liquid infused surface, as has been considered here. Additionally, there are several other facets of this hypothesized liquid-infused surface or coating that are worth (re)emphasizing. First and foremost, this hypothesized liquid-infused surface or coating is an interesting example of designing a liquid-infused surface or coating where the solid surface attains its final structural configuration after coming in contact with the lubricating liquid. Second, given the ease of grafting different types of surfaces with a layer of polymer molecules, this design will be more suited for the fabrication and deployment of liquid-infused coatings across a plethora of different surfaces.

We shall like to point out here that while polymer brushes have been studied for more than four decades, to the best of our knowledge, this study represents the first example of designing liquid-infused surfaces by employing a responsive layer of polymer molecules that undergo a globule-to-brush transition as it comes into contact with a liquid to which it is philic. Moreover, given the fact that we study the interaction of a liquid drop (i.e., a limited volume of liquid) with the grafted polymer layer, the equilibrium configuration consists of relaxed (in the form of "brushes") polymer

layer wetted by a thin film of liquid. Such a configuration is necessary to conceptualize the formation of the liquid-infused surface composed of polymer brush layer. Finally, as has been already pointed out, the use of the responsive polymer molecules (responding to the changes in the surrounding solvent) as “solid” or the “surface” part of the liquid-infused surfaces ensure that we are able to design a liquid-infused surface that responds to the presence of the liquid itself.

2.4 Discussions

Effect of Chain Length and Chain Wettability on the Drop Spreading-imbibition Process

This study, due to computational considerations, probes a 40-mer grafted polymer layer. Experimental papers studying the interactions of drops with the grafted polymer layers, however, have considered much longer polymer chains. For example, Brown et al. considered the interactions of a liquid drop with PNVOCMA (poly(4,5- dimethoxy-2-nitrobenzyl methacrylate)) brushes with the brush height (determined via ellipsometry) of 8-11 nm.[127] In another study, Brown et al. considered drop-brush interactions with poly[2-(methacryloyloxy)- ethyl-trimethylammonium chloride] (PMETAC) brushes of height 20 nm.[128] On the other hand, for our case, the height of the polymer layer varies from 1 nm (in the non-wetted state) to 1.7-2 nm (in the wetted and brush-like state).

A thorough analysis of the effect of the length of grafted polymer molecules on competing spreading and imbibition processes will require conducting several more simulations with gradually increasing the length of the polymer as well as the size of the liquid drop (without considering this increase in the drop size, there will not be sufficient liquid to wet the grafted polymer chains of longer length). That is a separate study altogether and beyond the scope of the present paper. However, even without conducting these actual simulations, we can make certain conjectures as to what might happen for cases when the liquid drop interacts with long chains of grafted, solvophilic polymer molecules. For a large enough size of the drop (i.e., a size that is large enough to completely imbibe into the layer of the grafted polymer molecules, which get extended to form brush-like architecture in contact with the liquid of the drop), we believe that the drop spreading and imbibition dynamics will be very similar to what we witness here. On the other hand, in case the drop is significantly small (i.e., so small that it fails to imbibe into the entire layer

of the grafted polymer molecules), we might have a highly interesting scenario. For this case, the drop will "wet" only the top half of the grafted polymer layers, while the bottom half of the grafted polymer layer will remain non-wetted. More interestingly, the drop having failed to wet the entire length of the grafted layer of polymer molecules and hence failing to reach the solid substrate, will remain localized only on the polymer surface (having wetted only the top part of the polymer layer). Under such circumstances, the drop might attain a "Neumann-like" state: this is the typical state attained by a liquid drop wetting a highly deformable, soft solid.[129-131] In fact such Neumann state is commonly witnessed for cases when a liquid drop equilibrates on the surface of another immiscible liquid. Also, this conjectured Neumann state for the present case will be different from that reported by Lubbers et al.[129] given the fact that for the present case, the drop is able to penetrate and imbibe inside the soft layer (the polymer layer), while in Lubbers et al.[129] such penetration of the drop inside the soft layer never occurs. As already mentioned, a possible future study probing different combinations of lengths of polymer molecule and drop sizes will be able to explore these different wetting and imbibition states.

In one of our recent papers,[124] we studied the interaction of a liquid drop on a layer of highly solvophobic polymer chains. We found that the drop does not imbibe at all in the polymer chain layer. We also found that the drop, like a nanoparticle, rolls (and never spreads) on the solvophobic polymer layer. The present case is the exact opposite: here the polymer layer is extremely solvophilic enabling spontaneous imbibition and spreading. Therefore, for the case where the solvent is not so much wetting, we would anticipate a behavior that is in between these two extreme cases. i.e., there will be (1) a partial wetting and spreading of the drop on the polymer layer polymer layer and (2) a partial imbibition of the drop inside the polymer layer.

Use of Chemically Identical Materials as Liquid Drop and the Polymer Layer

In this work, we aim to study the interaction of a liquid drop with a layer of grafted polymer layers that are extremely philic to the liquid drop. In our study, the coatings (or the layer of grafted polymer) and the liquid drop are chemically identical. The reason for this choice is that we don't have the information of the interaction parameters of two chemically different materials that are extremely philic to one another and one material forms a drop at room temperature and another material is a polymer that can be grafted as a dense layer.

In the context of the liquid-infused surfaces (LISs), indeed a critical criterion to develop such surfaces is to ensure that the lubricating liquid (which serves the purpose of the "infused liquid") must wet and spread onto the rough solid substrate. Very often this does not occur spontaneously, and one needs to chemically coat the pre-existing rough surface to make it wettable by this lubricating liquid.[99] For our problem to consider such a scenario, we need to be certain that material used for this chemical coating can form grafted polymer layers (which will transition to "brush"-like state in presence of appropriate solvent). The central idea, however, is not whether these materials (the coating on the solid surface and the lubricating oil) are chemically different significantly; rather the idea is that in existing studies of the LISs, the pre-existing solid surfaces might not always be directly usable and requires an additional chemical coating treatment. On the other hand, our proposed method opens up the possibility of developing such LISs without the requirements of such additional coating treatment: the layer of densely grafted polymer molecules grafted on a philic solid surface serves the purpose of the "surface" and the drop of the chemically identical (to the grafted polymer molecules) liquid that imbibes into the polymer layer spontaneously serves the purpose of the "liquid" (or the very thin liquid film that completely wets

the rough solid in a LIS set-up). The final result, therefore, is this proposed system that resembles the LISs without necessitating additional coating treatment (often required for conventional LISs).

Comparison of the Present Study with other related studies of Drops interacting with Layer of Polymer Brushes and other Brush-Like Soft Porous Materials/Coating

There have been several studies probing the interactions of grafted polymer layer (or polymer brushes) with a melt droplet that is chemically identical to the grafted polymer layer. Therefore, system-wise, these studies are very similar to our study. Of course, we consider the dynamics of the interaction of the drop with the grafted polymer layer, which these studies do not do. However, in terms of the final equilibrium state, we can use these studies to check our findings. For example, Ferreira et al.[107] presented the scaling conditions for the transition to autophobicity as a function of the parameters N (polymerization index of the grafted chains), P (polymerization index of the polymer melt) and σ_g (non-dimensional grafting density): they showed that this autophobic transition (i.e., the transition when the brushes, with respect to the chemically identical melt droplets, become phobic from philic) will not occur as long as $\sigma_g\sqrt{N} < \left(P/N\right)^{-1/2}$ (for $P/N < 1$) or $\sigma_g\sqrt{N} > P/N$ (for $P/N > 1$). For our case, P/N=0.2 and we find that $\sigma_g\sqrt{N}$ = 0.22, 0.3, 0.54, 1.58 (for $\sigma_g = 0.034, 0.048, 0.085, 0.25$) and $\left(P/N\right)^{-1/2} = 2.24$. Therefore, for all possible values of σ_g, we have $\sigma_g\sqrt{N} < \left(P/N\right)^{-1/2}$: therefore, our results confirming the presence of swollen wet brush state (or equivalently, a state of complete mixing between the polymer melt and the grafted polymer layer) for all the grafting density values are supported by the scaling calculation predictions of Ferreira et al.[107] Similarly, Mass et al.[108] introduced an identical scaling

criterion as that of Ferreira et al.[107] for the transition to autophobicity: therefore, our results are also confirmed by the scaling predictions of Mass et al.[108]

Pastorino et al.[132] employed MD simulations to probe the static and dynamic properties of the interface between a polymer brush layer and a chemically identical melt. This paper provided some extremely useful results such as the configurations of the chains of the brush layer and the melt film, the velocity of the melt film at the brush surface, variation of the viscosity of the melt, etc. as functions of the grafting density of the polymer brush layer, dimensionless shear rate (quantified by the corresponding Weissenberg number), etc. This paper[132], however, is different in the geometry (as compared to our case) since they did not consider the melt in the form of a droplet. Rather the melt is considered as a thin film that is sandwiched between two layers of polymer brushes. Therefore, the dynamical issues (e.g., dynamics of drop spreading, drop imbibition, relaxation of the grafted collapsed polymer chain as they come in contact with the droplet, etc.) haven't been probed. In fact, none of the results of Pastorino et al.'s paper[132] provide any time-dependent variation of any of the quantities.

de Beer et al.[133] conducted experiments on interactions between miscible and immiscible polymer brushes and showed that the immiscible brush systems can form slick interfaces, eliminating interdigitation and thereby strongly reducing dissipation. These facets ensured direct a significant reduction in friction, while still maintaining load-bearing ability. This work, while also discussed the case of interactions between chemically identical brushes, did not consider any droplet and therefore did not provide insights into the details of the coupled spreading-imbibition dynamics and the resulting attainment of a completely mixed state (between the droplet and the polymer layers) that has been done in the present study.

There are also several studies probing the interactions between a droplet and a polymer-based coating (e.g., studies by Zhao *et al.*[134], Xu *et al.*[135], etc.). However, there are some significant difference between our present work and these studies. For example, in our current work, the coating, i.e., the grafted polymer layer shows complete mixing with the liquid drop as the drop spreads. Most of the previous works (Refs. 134, 135), on the other hand, considered a porous substrate where the drop and the substrate always maintained a sharp interface between them and the drop phase always remained separate from the coating (even though the liquid can permeate through the soft substrate). These studies (Refs. 134, 135) also do not explicitly discuss the imbibition dynamics of the drop. Inutsuka *et al.*,[136] in an apparently related study, considered the surface reconstruction of a matrix of PDMS elastomer with a small amount of added diblock copolymer that can interact with a water drop upon wetting. However, our study is significantly different from this system, since in our work the wetting occurs in the presence of a collapsed polymer layer that is end-grafted to the surface. Also, Inutsuka *et al.*,[136] the surface reconfiguration occurs after drop spreading, unlike in our system where these processes are simultaneous. Moreover, in the current work, we consider a scenario where the dimensions of the liquid drop are comparable to the length scale of the polymer chains, which does not seem to be the case in Inutsuka *et al.*[136] In another related study, Cohen-Stuart *et al.*[137] discussed the wetting properties of water on a hydrophilic polymer coating (poly-ethylene oxide) on an inherently hydrophobic substrate (polystyrene). They observed a partial wetting state with philic grafted polymers and beyond a critical value of grafting density a stable value of the equilibrium contact angle of the drop was observed. The current work is significantly different from this scenario in the sense that the bare substrate (silica) in our study is extremely solvophilic, and correspondingly, has a zero contact angle with the drop. Thiele at al.[138] solved the problem of drop wetting on polymer brushes

using a gradient dynamics model. They considered simple substrates that can be characterized by a single order parameter: for their case, this single order parameter was the amount of liquid absorbed into the polymer layer. The dynamics occurred in the presence of an appropriate energy functional, which included terms for capillarity, wettability, and the brush energy. The results in their work were for a simplified case where the drop was much larger in dimension than the polymer chains preventing the drop from completely mixing with the grafted layer. This is in sharp contrast to the present paper, where the liquid drop completely penetrates the brushes and the height of the drop is pinned by the polymer chains. Under such circumstances, the dynamics of the drop spreading and imbibition associated with the case where the drop completed mixes with the polymer layer (as occurs in the present case) is not captured by the work of Thiele et al.[138]

Effect of Undersaturation in the Final Configuration of the Grafted Polymer Layer

Our results indicate that the final state of the grafted polymer brushes, on being wetted by the drop, is brush-like (confirmed by the brush height scaling as $\sigma_g^{1/3}$). However, we shall like to point out here that there is some extent of undersaturation at this final wetting state. This undersaturation occurs as the drop continues spreads to adjacent locations of the grafted polymer layer. However, this undersaturation is not too severe, and accordingly brush-like configuration is still retained. This is the reason why we still approximately recover the $h \sim \sigma_g^{1/3}$ scaling. In order to gauge the effect of undersaturation in the value of the equilibrium brush height in our simulations, we compare the brush height obtained for our case with those predicted by the established scaling laws (see Ref. 107) for the height ($h = N\sigma_g^{1/3}P^{-1/3}$) of the polymer brushes in the swollen wet state (i.e., for the cases where the polymer brushes are wetted by melts that are chemically identical to these polymer brushes[107]). For our case, the final equilibrium heights of the

grafted polymer molecules are 0.71, 0.7, 0.6, and 0.59 times that of the corresponding scaling calculation predicted brush height ($h=N\sigma_g^{1/3}P^{-1/3}$) for cases of $\sigma_g = 0.034/\sigma^2$, $0.048/\sigma^2$, $0.085/\sigma^2$ and $0.25/\sigma^2$, respectively. Therefore, the effect of the undersaturation representing a (not too severe) reduction in the brush height (as quantified by the aforementioned ratio) is similar for all grafting densities (the ratio varies between 0.59 and 0.7, irrespective of the grafting density, see above), thereby preserving the $h\sim\sigma_g^{1/3}$ scaling behavior.

Also, we shall like to point out here that only for the cases of low grafting density, the extent of undersaturation is evident from the difference between the maximum and final (equilibrium) heights of the polymer brush. For the case of larger grafting densities, on the other hand, the timescale of relaxation of the brushes becomes much larger than the timescale of the drop spreading. Under such circumstances, the brushes relax much more slowly and accordingly, the extent of undersaturation is no longer represented by the evolution of the brush height (as a result, for these cases of large grafting densities, the difference between the maximum and the final values of the brush height is negligible).

2.5 Conclusion

In this study, we investigate through MD simulations the behavior of a liquid drop interacting with a solvophilic, soft, porous, and responsive surface represented by a layer of grafted polymer molecules (philic to the liquid of the drop) that undergo a transition from a globule-like state (in absence of the drop) to a brush-like state (when wetted by the drop). The spreading dynamics is dictated by the balance of the driving vdW forces and the resisting inertial or brush-induced drag forces (depending on the stage of spreading) and this consideration allows deriving scaling laws that reasonably describe and agree with the MD simulation results for spreading dynamics and equilibrium contact radii. We also describe the wicking behavior of the drop through the polymer layer as well as the time-dependent response of the polymer molecules to the drop wicking. Finally, we argue that the present study points to a most remarkable possibility of designing widely deployable, "responsive", and soft liquid-infused surfaces and coatings with the imbibing liquid drop serving as the "lubricating liquid" and the polymer-grafted solid surface serving as an "responsive surface". The ability of nanoscale exploration of the problem through MD simulations enables shedding light on the nanoscale dynamics and formation of such "responsive" and soft liquid infused surfaces and coatings.

Chapter 3: Extensive Stable Physical Contacts Between a Nanoparticle and a Highly Repulsive Polymeric Layer *

Abstract

Interaction between nanoparticles (NPs) and a layer of grafted and solvated polymer molecules has been widely explored for a variety of applications ranging from fabrication of nanocomposites and sensors to developing nano-coating for virus de-activation. In all these applications, the solvated polymer molecules are necessarily philic to the NPs, and consequently, driven by the favorable NP-polymer interactions, there is the formation of numerous stable direct (i.e., without any intervening solvent molecule) NP-monomer (monomer of the polymer) contact pairs. Here we propose a paradigm shift in this problem: we employ molecular dynamics (MD) simulations and establish that under appropriate conditions, it is possible to develop numerous stable direct contacts between a NP and a solvated polymer layer even when the polymer molecules are extremely phobic to the NP. Here by "stable" contacts, we refer to the NP-Polymer contacts that remain intact for a finite duration of time; of course, such contacts, after being intact for a finite time duration, might get broken and re-formed. In terms of the mechanism of the process, the NP is driven inside a grafted layer of collapsed (in absence of solvent) and phobic (to the NP) polymer molecules by a liquid drop (polymer is philic to the liquid). Subsequently, the liquid molecules imbibe and diffuse inside the polymer layer, but the NP, due to the large Steric effect imposed by the polymer molecules, remain localized within the polymer layer. This ensures the establishment

* Contents of this chapter are published as: Etha, S. A., Pial, T. H., & Das, S. (2022). Extensive Stable Physical Contacts between a Nanoparticle and a Highly Repulsive Polymeric Layer. *The Journal of Physical Chemistry B*, *126*(30), 5715-5725.

of several stable direct contacts between the NP and the highly phobic polymer molecules. We quantify these contacts by their numbers, stability, and frequency of occurrences as well as their dependences on the NP-polymer interaction energies and NP sizes. We also quantify the associated NP dynamics inside the polymeric layer. Finally, we argue that our finding will open up avenues for leveraging NP-polymer interactions for a myriad of applications even for cases where the polymer molecules are phobic to the NPs.

3.1 Introduction

Grafting uncharged and charged polymer layers on solid surfaces and particles attributes a wide range of capabilities to these surfaces and particles.[139,140] Most of these capabilities stem from the responsiveness of the grafted polymer or polyelectrolyte (PE) layers to the environmental stimuli (e.g., temperature and quality of the solvent in which these layers are present, ions in the solvent for the charged polymeric molecules, etc.). Recently, there has been significant interests in probing the response of a grafted polymer/PE layer (sometimes in the form of densely grafted "brushes" in a good solvent) to a nanoparticle (NP). Such NP-polymer-layer or NP-polymer-brush (NP-PB) interactions are critical for fabricating polymer nanocomposites,[141] nanosensors,[142] plasmonic devices,[143] and virus-inactivating nanocoating,[144] optimizing the utilization and performance of a wide variety of polymer-based nano-reactors,[145,146] and ensuring assembly[147,148] control,[147] and organization[149] of NPs using polymer brushes. Other related applications include better understanding the interactions of cilia-bound brushes (constituting the periciliary layer of the lung epithelial cells, as proposed in a recent study by Button *et al.*[150]) with toxins (in the form NPs) for developing strategies to combat lung diseases, and for several uses involving interactions of NPs

with polymer brushes in air (polymer brushes in air, reviewed in details by van Eck *et al.*,[151] has recently received significant attention for a myriad of applications such as the sensing of volatile organic compounds like acetone,[152] water harvesting from fog by using brush-grafted cotton fabric,[153] etc.). Motivated by such wide-ranging applications, there has been significant exploration of developing molecular scale models for probing such interactions between NP and grafted polymer (or PB) layer.[154-157] Most often such interactions have been studied for the cases where the NPs are highly attractive or "philic" to the grafted polymer (or PB) layer: some examples include the study of Cheng *et al.*[154] probing the evaporation-driven self-assembly of the NPs within the PB layer, the work of Venkatesh *et al.*[158] studying the dynamics of infiltration of glassy polymers into solvent-filled NP packings, the investigation of the free energy cost associated with insertion of NPs into a polymer brush layer under varying solvent conditions,[159], etc.

In this study, we employ MD simulations for developing a novel concept of establishing and sustaining direct physical contact of a NP with a highly "*phobic*" polymeric layer (or a polymeric layer that is highly *repulsive to the NP*). The usual combination of a NP and a polymeric layer that is highly "philic" to the NP implies a significant reduction in the choices of the NP-polymer combination that can be employed for various applications. On the contrary this proposed capability of establishing sustainable physical contacts between a NP with a polymer layer that is significantly "phobic" to the NP signals the possibility of using much wider ranges of NP-polymer combinations that are well beyond the standard practice of using only highly favorable polymer-NP combinations. We consider a Lennard Jones (LJ) liquid drop containing a NP (composed of LJ beads) that interacts favorably with the drop (ensured by choosing $\varepsilon_{LN} = 1$, where ε_{LN} is the dimensionless LJ liquid-drop-NP interaction parameter). This NP-laden liquid drop is made to interact with a densely grafted layer of polymer molecules that are originally in a collapsed

globular state. The polymer molecules are represented as LJ bead-spring models and we choose $\varepsilon_{LP} = 1$ and $\varepsilon_{PN} < 1$ (where ε_{LP} and ε_{PN} are the dimensionless LJ liquid-drop-polymer and LJ polymer-NP interaction parameters, respectively). By imposing the condition $\varepsilon_{ij} = 1$ (e.g., $\varepsilon_{LN} = \varepsilon_{LP} = 1$), we imply that species *i* and *j* are behaving like identical species as long as their attractive interactions are concerned. In other words, $\varepsilon_{ij} = 1$ implies that the attractive interactions between one particle of species *i* and one particle of species *j* is identical to attractive interactions between two particles of species *i* or two particles of species *j*. Therefore, when we consider $\varepsilon_{ij} < 1$ (e.g., $\varepsilon_{PN} = 0.3$ or $\varepsilon_{PN} = 0.1$), we assume that the corresponding attractive interaction between these species *i* and *j* (i.e., the polymer and the NP) is significantly more unfavorable as compared to liquid-NP (with $\varepsilon_{LN} = 1$) and liquid-polymer (with $\varepsilon_{LP} = 1$) attractive interactions. In other words, these choices of ε_{LP} and ε_{PN} ensure that the polymer molecules are philic to the liquid drop and phobic to the NP. We consider cases where ε_{PN} can be as small as 0.1 (signifying that the polymer molecules are extremely phobic to the NP). On the other hand, the polymer molecules being philic to the drop (since $\varepsilon_{LP} = 1$), the drop simultaneously spreads and imbibes within the polymer layer and in response the polymer molecules start stretching out as the solvent around them changes from "poor" (case of no solvent) to "good" (case of the solvent as the liquid to which the polymers are philic). This combined response of the drop (simultaneous spreading and imbibition) and the grafted polymer molecules (changing from collapsed to stretched states) has been studied in great detail in our previous paper.[160] The most interesting question here is: *What happens to the NP as the drop spreads and imbibes through the grafted polymer layer?* We find that the NP starts to develop finite stable contacts with the polymer molecules: these contacts are direct "physical contacts" between the polymer and the NP without any intervening liquid molecules. We quantify such contacts by identifying (1) if at a given time there is at least one

contact between the NP and the polymer layer, (2) the total number of contact pairs established between the NP and the polymer layer at a given time, and (3) the stability of these contacts (measured by the time it takes for the contact to get disrupted after it has been formed). These quantities establish the most remarkable situation where stable physical contacts are established between the NP and a highly repulsive polymeric layer. By "stable", we refer to contacts that remain intact over a finite time duration. Given the highly "phobic" nature of interactions between the NP and the polymer, existence of such contact that remain unbroken for a finite time duration is rather remarkable. Of course, these contacts do not remain intact eternally: rather, they get broken and re-form time and over again. We further identify the effect of the values of ε_{PN} and the NP radii in such contact formation and probe the corresponding dynamics of the NP within the polymer layer. Finally, we discuss the manner in which our study opens up the scope of using a more extensive NP-polymer combination (including the cases where the polymers might be highly phobic to the NPs) for applications (see above) that rely on establishing highly stable NP-polymer direct contacts.

3.2 Computational Methods

We study the dynamics of a NP-laden Lennard-Jones (LJ) solvent drop interacting with a layer of solvophilic polymer molecules grafted on a solvophilic substrate by performing Molecular Dynamics (MD) simulations that are carried out using the Large-scale Atomic/Molecular Massively Parallel Simulator (LAMMPS) software package.[161]

All species in our system interact through a standard LJ 12-6 pair potential given by, $U_{LJ}(r) = 4\epsilon\left[\left(\frac{\sigma}{r}\right)^{12} - \left(\frac{\sigma}{r}\right)^{6} - \left(\frac{\sigma}{r_c}\right)^{12} + \left(\frac{\sigma}{r_c}\right)^{6}\right]$, where ϵ is the strength of LJ interactions, r is the distance between the centers of the interacting species and σ is the size of the species. The cutoff distance, $r_c = 5\sigma$ is used for all non-bonded pairs, unless explicitly mentioned. The interaction strength between the NP and polymer beads (ε_{PN}) is varied, while keeping all other interactions the same. We consider a 3D drop and choose a simulation box of dimensions $L_x \times L_y \times L_z = 64\sigma \times 64\sigma \times 160\sigma$. The simulation domain is periodic in both the x and y directions, but not in the z-direction, where a fixed boundary condition is implemented.

We model the grafted polymer as linear chains consisting of 100 beads connected by permanent bonds. We employ the bead-spring polymer model introduced by Kremer and Grest[162] (KG) for our grafted polymer molecules. The Kremer-Grest model represents a polymer chain as a series of beads that are connected by bonds. Each bead represents a monomer unit in the polymer chain, and the bonds represent the covalent bonds that connect adjacent monomer units. One of the main features of the Kremer-Grest model is the use of a "bead-spring" potential to describe the interactions between the beads. This potential includes a harmonic potential that models the bond stretching between adjacent beads, as well as a Lennard-Jones potential that models the non-bonded interactions between the beads. In addition to the bead-spring potential, the Kremer-Grest model also includes a "soft potential" that models the excluded volume interactions between the

beads. This potential ensures that the beads do not overlap with each other, which is important for simulating realistic polymer chains. Overall, the Kremer-Grest model provides a powerful tool for understanding the behavior of polymer chains in various environments and under different conditions. It has been used to study a wide range of phenomena, including polymer melts, glasses, and networks, as well as the behavior of polymer chains under confinement and in the presence of external fields. Previous studies have proved the efficacy of adapting the KG model to model melts of real polymers. The authors showed that Kuhn-scale mapped KG models faithfully represent the universal properties dominated by large-scale conformational statics and dynamics of flexible polymers.[163] The polymer beads are connected by bonds modeled using the finitely extensible nonlinear elastic (FENE) potential, $U_B = -0.5KR_0{}^2 \ln\left[1 - \left(\frac{r}{R_0}\right)^2\right]$, where r is the separation distance, $R_0 = 1.5\sigma$, and $K = 30\epsilon/\sigma^2$. We assume that the polymer chains have no inherent stiffness. All solvent and polymer beads have a mass m. All bonded pairs of neighboring beads on a polymer chain interact through the standard LJ 12-6 pair potential as given above, but with a cutoff distance of $r_c = 2^{\frac{1}{6}}\sigma$.

The NPs are modelled as spherical shaped LJ solids consisting of multiple coarse-grained (CG) beads arranged in an FCC lattice structure. Each CG bead has mass m and the NP has a resulting density of $1\ m/\sigma^3$. A uniform reflective wall is placed at the top of the simulation domain to prevent the liquid molecules from escaping. The substrate is modelled as a fixed wall of beads uniformly distributed with an area density of $1\ m/\sigma^2$ interacting with all other species *via* the 12-6 LJ potential with a cutoff distance of $r_c = 2^{\frac{1}{6}}\sigma$. We do not consider any Coulombic interactions in our system and the non-bonded interactions in our system only include a shifted-truncated 12-6 LJ potential. As such, the model adopted in this study is appropriate for systems dominated by van der Waals interactions. We summarize the LJ interaction parameters in our system in the table 1

below (in the table r_c denotes the cut-off for the LJ interactions). Also, the beads representing the different species (e.g., solvent molecules, monomers, nanoparticle pseudo-atoms, and wall molecules) are all identically sized ($\sigma = 1$).

Table 3.1: Strength and cut-off distances of the LJ interactions between different species

Particle Type A	**Particle Type B**	$\boldsymbol{\varepsilon_{LJ}}$	$\boldsymbol{r_c\ (\sigma)}$
Wall	Wall	0	-
Wall	Polymer/Fluid bead	1	1.12
Wall	NP bead	ε_{PN}	1.12
Polymer/Fluid bead	Polymer/Fluid bead	1	5
Polymer bead	NP	ε_{PN}	5
Fluid bead	NP	1	5
NP	NP	0	-

The simulations are carried out in an NVT ensemble using the Nosé-Hoover thermostat.[162,163] All simulations are performed with a timestep of 0.002τ and the damping factor of the thermostat is considered to be 100 timesteps (0.2τ). We start the simulation with the reduced LJ temperature of all particles set at T* $\left(= \frac{Tk_B}{\epsilon}\right)$ = 0.1, and gradually increasing the temperature to T* = 1, while keeping the liquid drop fixed at a large enough distance away from the grafted polymer molecules so that the drop-polymer interactions are negligible. We consequently displace the drop along with the nanoparticle in the negative z-direction to bring the drop closer to the brushes, so that the separation distance between the bottom of the liquid drop and the top of the collapsed polymeric layer is $\sim 2\sigma$, and simulate the system for a minimum of 40000τ to ensure the drop and polymer brush system achieves an equilibrium configuration. To visualize the uptake of the NP into the

phobic polymeric layer we provide the variation of the z-coordinate (vertical location) of the NP center-of-mass and the corresponding polymer layer height as functions of time from when the drop is displaced towards the grafted polymer layer, in the SI. We then perform production runs for our system and generate trajectories for an additional 20000τ, which in turn is split into 4 sampling runs each of which are of length 4000τ and are separated by a length of 1000τ that was omitted from all sampling calculations (to ensure that the sub-trajectories are independent). This commonly used sampling method, which is denoted as "block-averaging" method, has been demonstrated schematically in the figure below. We collect data every 0.1τ. Usually, grafted polymer molecules take a few hundred τ to equilibrate.[164] Also, all the visualizations of the atomic trajectories are performed using the open-source software OVITO.[165]

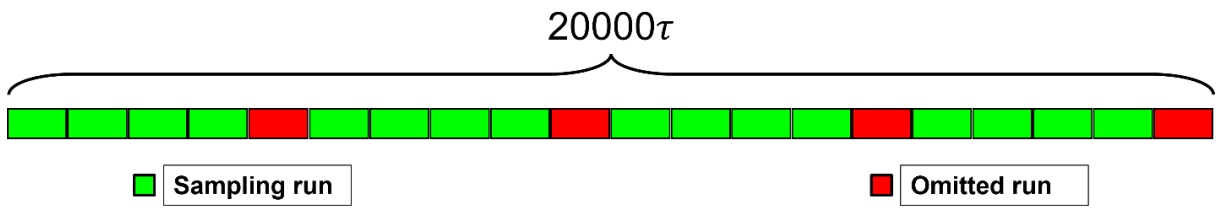

Figure 3.1. Schematic representing the sampling method employed in this work.

3.3 Results

Fig. 3.1(a-d) provides the MD simulation snapshots summarizing the mechanism of triggering stable physical contacts between the NP and the polymer layer that is phobic to the NPs. The process begins as the NP is carried by the drop into the polymer layer [see Fig. 3.1(a,b)]. Subsequently, as the drop spreads and imbibes through the polymer layer, there are two occurrences: (a) the collapsed polymer molecules (or polymer molecules in the globular state) stretch out (as they come in contact with a favorable solvent) and (b) the NP penetrates inside this polymer layer [see Figs. 3.1(c,d)]. The solvent molecules (of the drop) due to their philic interactions with the polymer layer imbibe throughout the polymer layer very quickly. On the other hand, the NP that has been originally introduced into a highly phobic (to the NP) polymer layer by the drop, due to the Steric effects imposed by the polymer layer, can no longer move along with the drop inside the polymeric layer. This large discrepancy in the mobility of the solvent molecules and the NPs within the polymer layer can be understood by comparing their MSDs (please see Fig. 3.4 and Fig. B.2 in the Appendix). Due to this discrepancy, the NP eventually loses (at least temporarily) some of the encapsulation by the solvent molecules, and therefore, establishes a direct contact (without the intervening solvent molecules) with the polymer molecules. Monomers that are within the first solvation shell of the NP are considered to be in contact with the NP for the case of such direct polymer-NP contact. Such a situation is depicted in Fig. 3.1(e). Of course, this direct NP-polymer contact can be quantified by a monomer-NP (monomer of the polymer molecule) separation distance of $d_1 \approx \sigma$ (where σ is the LJ distance parameter for the solvent) [see Fig. 3.1(e,g)]. This direct contact is often stable and the extent of this stability can be measured by identifying the time variation of this separation distance: for example, Fig. 3.1(g), which represents the dynamics of one such monomer-NP contact, elucidates that this separation distance d remains

approximately equal to d_1 for a significant period of time (establishing that the direct NP-polymer contact is stable), and only after an elapse of a significant amount of time, the NP loses this contact with the monomer of the polymer molecule leading to a much enhanced NP-polymer separation distance. Of course, this contact can actually re-form (and NP-monomer separation distance becomes d_3, with $d_3 \approx \sigma$) after some time [as evident from Fig. 3.1(g)].

It is important to discuss the thermodynamics governing the process of liquid drop mediated insertion of the NP into a layer of polymer molecules that are phobic to the NP. The process involves two favorable and two unfavorable energetic interactions. The liquid is philic to both the polymer and the NP. Therefore, there is an enthalpic gain (a favorable energetic interaction) associated with the liquid molecules coming in contact with the polymers as well as the NP remaining in contact with the liquid molecules. On the other hand, there is an energetic penalty (or unfavorable energetic interactions) associated with (1) a loss in entropy caused by the NP getting localized within the brush layer and (2) development of stable contacts between the NP and the polymer molecules. The occurrence of the NP getting localized within the brush layer, which in turn triggers these above-identified energetic penalties, becomes possible since these energetic penalties get compensated by the enthalpic gains associated discussed above. From a more fluid mechanics perspective, one can describe the process as follows. The NP prefers to stay inside the drop since the solvent of the drop is very philic to the NP, while the vacuum above the drop is very "poor" (or "phobic") to both the drop and the NP; subsequently, as the drop enters the brush layer, swells the brush, and disperses laterally, it pushes the NP inside the swollen brush layer.

The second important issue to note here is that the NP will remain trapped inside the grafted polymer layer as long as the polymer layer remain solvated. For actual practical scenarios, where

this solvent might get evaporated, the polymer-polymer interactions will start to dominate; in other words, the energetically favorable solvent-polymer interactions will disappear, and hence there will be no factor to compensate for the energetic penalty associated with the entrapment of the NP within the brush layer (as discussed above). As a consequence, the NP will no longer remain entrapped within the polymer layer (of course, it might remain adsorbed on the brush surface, similar to what happens in Cheng *et al.*[154]). This limitation of this approach, associated with the possible evaporation of the solvent, should be kept into consideration for the different practical applications of this method (some of these applications have been elucidated in the DISCUSSIONS section).

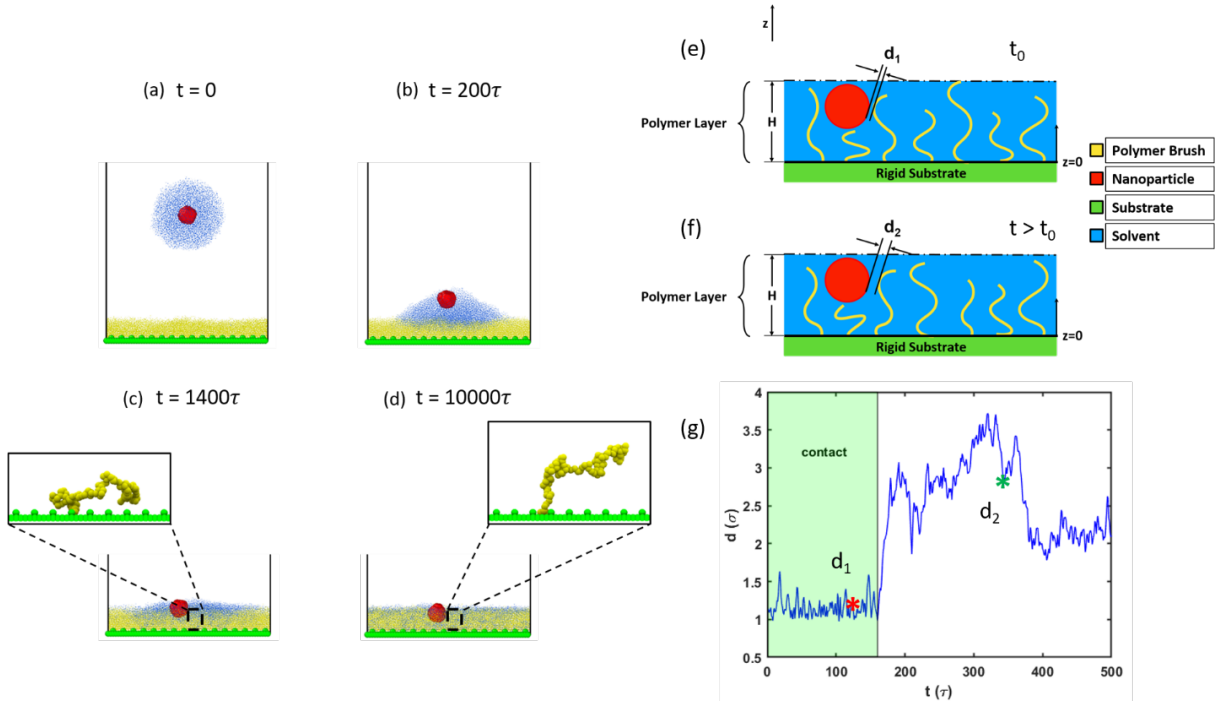

Figure 3.2. (a-d) MD simulation snapshots depicting the wetting of the grafted polymer layer and the simultaneous imbibition of the NP into the polymer layer as the NP is carried inside the polymer layer by the liquid drop. In the inset of (c) and (d) we provide a magnified view of the transition of a polymer from a collapsed [see the inset of (c)] to a stretched [see the inset of (d)] state as the polymer gets wetted by the solvent. (e) Schematic representing the existence of a direct contact (without any intervening solvent molecules) between the NP and a monomer of a polymer chain: the corresponding separation distance between the NP and the monomer is $d_1 \approx \sigma$. (f) Schematic representing the situation where this direct contact between the NP and the monomer has been lost. The corresponding monomer-NP separation distance is d_2. (g) Distance (d, expressed in terms of σ) between nanoparticle and monomer as a function of time. The distance d is approximately d_1 (identified with a red star) for a significant duration of time establishing the stability of the direct NP-polymer contacts. Once this direct NP-polymer contact is broken the NP-polymer separation distance increases; d_2 (shown with a green star) is a representative value of this enhanced distance of separation. However, such direct NP-polymer contacts can be re-established at a later time even after breaking, as shown by a second region of contact around ~1500τ by separation distance d_3 (also shown with a red star): this implies that the NP-polymer contacts have the ability to break and re-form. The sub-figures (a), (b), (c), (d), and (g) were generated using simulation data for the case of $\frac{\varepsilon_{PN}}{\varepsilon_{LP}} = 0.1$ and NP size 3σ.

Fig. 3.2 quantifies the establishment of stable direct contacts between the NP and the polymer molecules. The detailed procedure for such quantification has been provided in the

Methods section and the SI. In Figs. 3.2(a-c), we plot the probability of contact, $P_{contact}$, as a function of the ratio of the interaction strength $\frac{\varepsilon_{PN}}{\varepsilon_{LP}}$ for different NP sizes. $P_{contact}$ is the probability that at least one direct NP-polymer contact pair exists at any given instant. As expected, we observe that $P_{contact}$ increases with an increase in ε_{PN} (i.e., an increase in the NP-polymer interaction strength) since a larger ε_{PN} obviously makes the polymer-NP contacts energetically more favorable. As inset to these figures, we plot a binary function describing the existence of NP-polymer contacts as a function of time for each NP size (for the case of $\frac{\varepsilon_{PN}}{\varepsilon_{LP}} = 0.3$). A value of 0 for the function implies that no contact exists between the NP and the polymer layer. If at least one contact pair exists, the function has a value of 1. The result establishes that even for the case where the NP-polymer interactions is highly unfavorable (i.e., $\frac{\varepsilon_{PN}}{\varepsilon_{LP}} = 0.3$), there is at least one contact for virtually entire time duration for all possible choices of the NP sizes. The effect of the NP size on $P_{contact}$, however, is more subtle and only becomes significant for the case of the most repulsive polymer layer $\left(\frac{\varepsilon_{PN}}{\varepsilon_{LP}} = 0.1\right)$. At this interaction strength, $P_{contact}$ decreases significantly with an increase in the NP size (in particular for a NP size of 5σ). Larger the size of the NP, more challenging it becomes for the liquid drop to drive that NP inside the polymer layer; this, combined with a more pronounced tendency of the NP to come out of the polymeric layer for the case of smaller $\frac{\varepsilon_{PN}}{\varepsilon_{LP}}$ ratio, makes $(P_{contact})_{\frac{\varepsilon_{PN}}{\varepsilon_{LP}}=0.1, radius=5\sigma}$ significantly small.

In Figs. 3.2(d-f), we plot the average number of direct NP-polymer contact pairs for different NP-polymer interaction strengths (i.e., different $\frac{\varepsilon_{PN}}{\varepsilon_{LP}}$) and NP sizes. The corresponding time variation of the average number of direct NP-polymer contact pairs for different NP sizes and $\frac{\varepsilon_{PN}}{\varepsilon_{LP}} = 0.3$ is provided in the insets of Figs. 3.2(d-f). In Fig. 3.2(d-f), as expected, we see that the

number of contacts increases with increasing interaction strength, which can be attributed to the corresponding increase in the favorability in the formation of the contacts. The effect of the NP size, however, is highly non-trivial and depends on the $\frac{\varepsilon_{PN}}{\varepsilon_{LP}}$ values. For example, for $\frac{\varepsilon_{PN}}{\varepsilon_{LP}} \geq 0.5$, the average number of contacts increases with an increase in the NP size. On the other hand, for $\frac{\varepsilon_{PN}}{\varepsilon_{LP}} \leq 0.3$, the average number of NP-polymer contacts decreases with an increase in the NP size. There are two effects at play here. The size of the NP determines the number of species in its first solvation shell (defined to be in contact with the NP): a larger size implies a greater number of possible contacts after the NP has been driven inside the polymer layer. However, for a phobic polymeric layer, the fraction of the NP solvation shell (given that the NP has entered the polymeric layer) that can be occupied by the monomers of the polymer chains reduces. These two competing factors determine the average number of contacts between the NP and the polymer layer. For $\frac{\varepsilon_{PN}}{\varepsilon_{LP}} \geq 0.5$, the NP-polymer interaction is significant enough so that the NP size effect becomes the determining factor in ensuring an increase in the number of contacts with an increase in size. On the other hand, for $\frac{\varepsilon_{PN}}{\varepsilon_{LP}} \leq 0.3$, the NP-polymer interactions are so unfavorable that the effect of the lack of the monomers of the polymeric molecules inside the NP solvation shell becomes the dominant factor, thereby reducing the number of NP-polymer direct contacts with an increase in the NP size. We can qualitatively compare these findings (as functions of the NP size) corresponding to smaller values of $\frac{\varepsilon_{PN}}{\varepsilon_{LP}}$ against those by Merlitz *et al.*[166] They studied the force-driven inclusion of NPs in polymer brush layers (in theta and athermal solvents) under the conditions where the NP and polymers are repulsive to one another (which qualitatively matches the case of $\frac{\varepsilon_{PN}}{\varepsilon_{LP}}$ with values <<1). Merlitz *et al.*[166] reported that a larger force (or a larger inclusion energy value) is associated with driving a larger sized NP inside the polymer brush layer: this

result is commensurate with our finding that shows a progressive reduction in the number of NP-polymer direct contacts with an increase in the NP diameter for $\frac{\varepsilon_{PN}}{\varepsilon_{LP}} \leq 0.3$. Milchev *et al.*[167] also reports a similar situation where the free energy penalty associated with the inclusion of a NP inside a polymer brush layer that is repulsive to the NP increases with an increase in the NP radius.

We shall like to re-emphasize here that by "stable" contacts (between the NP and the polymer molecules), we imply contacts that last (or remain intact) for a finite duration of time. Given the highly "phobic" nature of interaction between the NP and the polymer molecules, formation and lasting (for a finite time duration) of such contacts are rather remarkable and that is the reason for which we focus our attention on the average number of "stable" contacts (or those contacts that remain intact over a finite time duration) formed between the NP and such polymer molecules. Of course, as has been already pointed out, these contacts will remain intact only for a finite duration of time: after that they will get disrupted and may or may not re-form again.

In Figs. 3.2(g-i), the relaxation time distribution (RTD) (see the *Methods* section and the SI for the calculation procedure) for the direct NP-polymer contact pairs is shown for different interaction strengths (or different $\frac{\varepsilon_{PN}}{\varepsilon_{LP}}$ ratios) and different NP sizes. Larger the RTD greater is the longevity of the contact pairs. Hence these figures [Figs. 3.2(g-i)] quantify the stability and the longevity of the direct NP-polymer contact pairs. Interestingly, the RTD for the case of phobic NP-polymer interactions ($\frac{\varepsilon_{PN}}{\varepsilon_{LP}} < 0.5$) remains identical across different interactions strengths and NP sizes. This is a very important observation: this confirms the significantly large stability of the NP-polymer direct contact pairs across a wide range of NP-polymer unfavorable interaction energies. The relaxation time for the less phobic NP (i.e., $\frac{\varepsilon_{PN}}{\varepsilon_{LP}} = 1$), however, is much larger than that of the more phobic NP (i.e., the NP for which $\frac{\varepsilon_{PN}}{\varepsilon_{LP}} < 0.5$), as evident from a much slower

decay of the RTD for $\frac{\varepsilon_{PN}}{\varepsilon_{LP}} = 1$. This is expected since the more favorable interactions between the NP and the polymer chain for the case of $\frac{\varepsilon_{PN}}{\varepsilon_{LP}} = 1$ leads to the formation of more stable NP-polymer contacts. It should also be noted that the RTD decays slower (implying larger relaxation time) for the larger NP sizes, albeit only slightly.

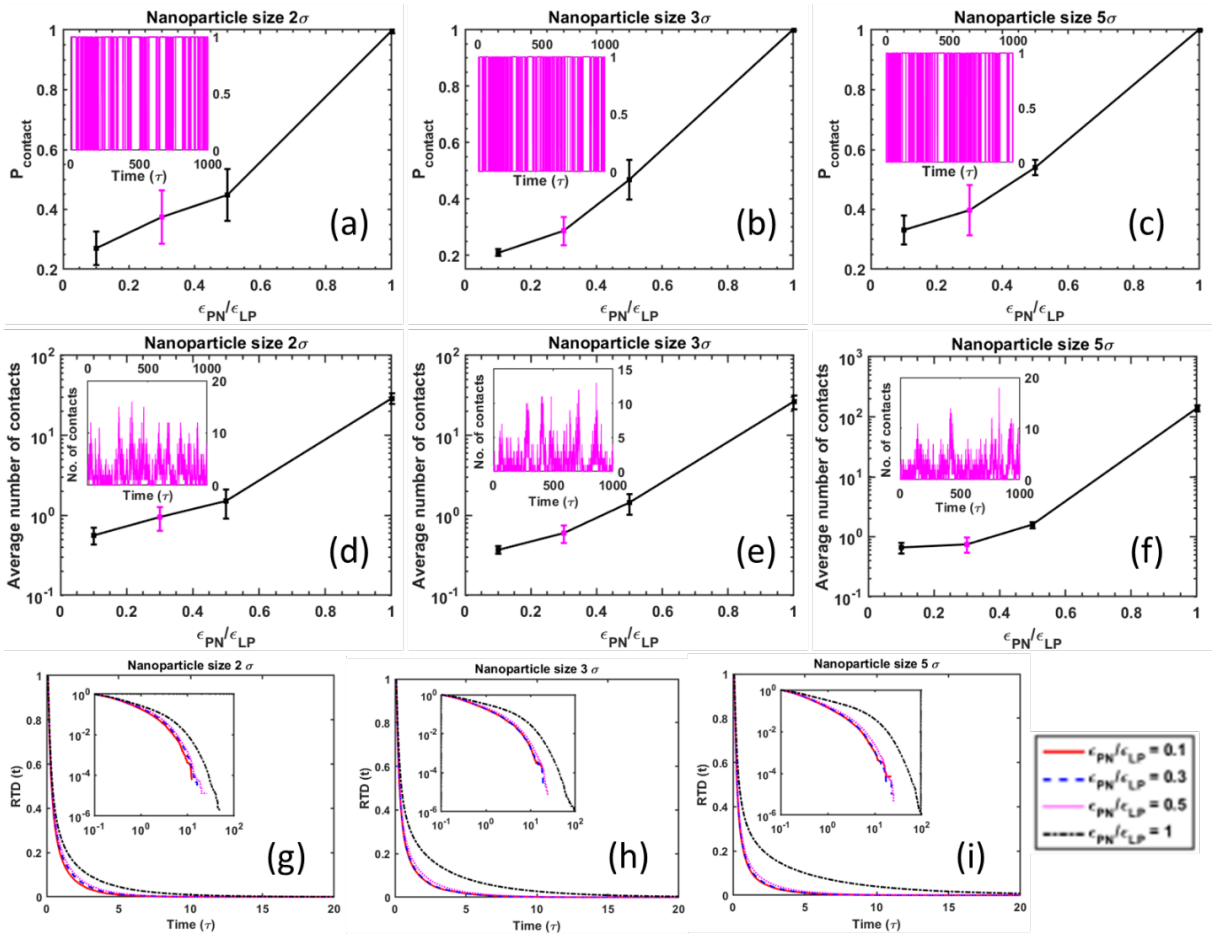

Figure 3.3. (a-c) Probability ($P_{contact}$) of the formation of at least 1 stable NP-polymer direct contact as a function of the NP-polymer interaction strength for different NP sizes. The figures in the inset of (a-c) provide the binary function of the NP-polymer direct contact as a function of time (for the case of $\frac{\varepsilon_{PN}}{\varepsilon_{LP}} = 0.3$ and the NP size being the same as the main figure), with the value of the function being 0 implying no contact and the value of the function being 1 representing the formation of at least one contact pair. (d-f) Average number of stable NP-polymer direct as a function of the NP-polymer interaction strength for different NP sizes. The figures in the inset of (d-f) provide the total number stable NP-polymer direct contact pairs as a function of time (for the case of $\frac{\varepsilon_{PN}}{\varepsilon_{LP}} = 0.3$ and the NP size being the same as the main figure). (g-i) Relaxation time distribution (RTD) for the NP-polymer direct contact pairs contact pairs direct as a function of the NP-polymer interaction strength for different NP sizes. The figures in the inset of (g-i) provide the same variation of RTD with time in the log-log scale.

Fig. 3.3 examines the mean square displacement (MSD) of the NP inside the grafted polymer layer in different directions (i.e., we report the NP MSDs in *x*, *y*, and *z* directions). We compare these MSD values in different directions for different values of the NP-polymer interaction strengths and sizes of the NP. As has been already pointed out, the NP, owing to its size and the associated Steric hindrance that it experiences from the polymer molecules, diffuses slower than the solvent molecules within the polymer layer: this is quantified by the large disparities in the MSD values of the NP in all directions and the solvent molecules inside the polymer layer (please also see Fig. B.2 in Appendix B). On the other hand, we find that the NP MSD values in the *unrestricted* directions (i.e., directions where we impose periodic boundary conditions, namely *x* and *y*) is much larger than the NP MSD value in the *z* direction. This difference exists for all possible values of the NP size (of course the difference is larger for smaller NP sizes) and NP-polymer interaction strength ($\frac{\varepsilon_{PN}}{\varepsilon_{LP}}$).

We observe that the NP MSD values (in any direction, *x*, *y*, or *z*) decrease with an increase in the NP size. This can be trivially explained by the fact that the larger NP experiences greater steric hindrance from the polymer layer and hence diffuses slower. The effect of the NP-polymer interaction strength ($\frac{\varepsilon_{PN}}{\varepsilon_{LP}}$) on the NP MSDs (for directions *x* and *y*), however, is non-trivial and is dictated by the NP size. For example, for the NP of size 2σ, the MSD of the NP (in *x* and *y* directions) decreases with an increase in the NP-polymer interaction strength (specially for $\frac{\varepsilon_{PN}}{\varepsilon_{LP}} \geq 0.5$): hence we find significantly reduced *x* and *y* MSD values for $\frac{\varepsilon_{PN}}{\varepsilon_{LP}} = 0.5, 1$ for NP of size 2σ [see Figs. 3.3(a,b)]. This can be attributed to the formation of a greater number of NP-polymer direct stable contacts for the case of a larger NP-polymer interaction strength, thereby inhibiting

the diffusion of the NP inside the polymer layer. On the other hand, for NPs of size 5σ, the massive size of the NPs imply orders of magnitude (as compared to that for the NP of size 2σ) smaller *x* and *y* MSD values (due to the obvious Steric hindrance from the polymer layer): for such small MSD values, we do not find any noticeable trend in the *x* and *y* MSD values as functions of $\frac{\varepsilon_{PN}}{\varepsilon_{LP}}$ ratios [see Figs. 3.3(g,h)]. For the NP of size 3σ, a separate factor also becomes important in dictating the NP *x* and *y* MSD as a function of $\frac{\varepsilon_{PN}}{\varepsilon_{LP}}$ values [see Figs. 3.3(d,e)]. For $\frac{\varepsilon_{PN}}{\varepsilon_{LP}} = 1$, very much like the case of the NP of size 2σ [see Figs. 3.3(a,b)], the strong interaction between the NP and the polymer molecules ensure a significantly reduced *x* and *y* MSD values. Very interestingly, however, *x* and *y* MSD values become small for $\frac{\varepsilon_{PN}}{\varepsilon_{LP}} = 0.1$ as well. A possible explanation for this behavior comes from probing the corresponding interaction of the NP with the solvent molecules. The NP having a very weak interaction strength with the polymer molecules (i.e., having a smaller $\frac{\varepsilon_{PN}}{\varepsilon_{LP}}$; e.g., $\frac{\varepsilon_{PN}}{\varepsilon_{LP}} = 0.1$) requires a shell of solvent molecules (henceforth denoted as solvent "cage") around it for ensuring that it remains stable inside the phobic polymer layer (see Fig. 3.4). This solvent "cage" increases the effective polymer size and hence increases the steric hindrance experienced by the NP, thereby restricting its motion. For the case of NP of size 3σ, this solvent "cage" is more pronounced and stable around the NP for the case of weak $\frac{\varepsilon_{PN}}{\varepsilon_{LP}}$ values, while for the NP with stronger $\frac{\varepsilon_{PN}}{\varepsilon_{LP}}$ values, the solvent "cage" around the NP is more easily distorted (see Fig. 3.4 and associated discussions for further details). A more stable solvent "cage" implies a NP with a larger effective size enforcing a weaker diffusion through the polymer layer; on the other hand, an unstable solvent "cage" ensures that the NP loses its encapsulating solvent molecules quicker, does not demonstrate any increased size effect, and hence can diffuse faster through the polymeric layer. This explains the significant reduction in the *x* and *y* MSD values of the NP (of size 3σ) for

$\frac{\varepsilon_{PN}}{\varepsilon_{LP}} = 0.1$. For smaller (size 2σ) and larger (size 5σ) NPs, there is little difference in the time responsiveness of the solvent "cage" for different values of $\frac{\varepsilon_{PN}}{\varepsilon_{LP}}$ (see Fig. 3.4); as a consequence, the solvent "cage" effect is less important in determining the variation of the MSDs (as functions of $\frac{\varepsilon_{PN}}{\varepsilon_{LP}}$) for the NPs of sizes 2σ and 5σ.

It is also useful to note that the *x* and *y* MSD values for some combinations of the NP size and the $\frac{\varepsilon_{PN}}{\varepsilon_{LP}}$ ratio show a near linear trend indicating a constant diffusivity for these cases [see Figs. 3.3(a,b,d,e,f,g)]. Of course, for certain parameter combinations (e.g., *y* MSD for the NP size of 3σ and $\frac{\varepsilon_{PN}}{\varepsilon_{LP}} = 1, 0.1$), the MSD curve plateaus (or increases very weakly with time) indicating a stagnation (or slowing down) of the NP in the corresponding direction. Effects such as enhanced interactions between the NP and polymer (for $\frac{\varepsilon_{PN}}{\varepsilon_{LP}} = 1$) or dominant role of the solvent cage effect (for $\frac{\varepsilon_{PN}}{\varepsilon_{LP}} = 0.1$ and NP size of 3σ) can justify such stagnation (or slowing down) of the NP inside the brush layer. In order to ensure the entrapment of the NP inside the solvated polymer layer the *z* MSD of the NP needs to be smaller than H^2 [*H* is the average height of the solvated polymer layer, see Figs. 3.1(e,f)]. We see distinct plateauing of the *z* MSD for NP (indicating NP does not move in *z* direction) of sizes 2σ and 3σ for most of the values of $\frac{\varepsilon_{PN}}{\varepsilon_{LP}}$ [see Figs. 3.3(c,f)]. The only exception is the case of $\frac{\varepsilon_{PN}}{\varepsilon_{LP}}$=1. Also, for the case of NP of size of 5σ, such plateauing of the *z* MSD is absent for the cases of $\frac{\varepsilon_{PN}}{\varepsilon_{LP}}$=0.1, 1 [see Fig. 3.3(i)]. For all these cases, where there is no plateauing of *z* MSD, these MSD values themselves are just a few σ^2 (and increases at a very slow rate) and are orders of magnitude smaller than H^2 (where $H^2 \sim 225\sigma^2$): this implies that while the NP has not stagnated in the *z* direction, it remains (and will remain over a very significant future time duration) very much entrapped within the brush layer (given that for

the NP to leave the brush layer, its z MSD has to be larger than H^2). Therefore, while what happens at a much later time instant (say at a time t equal to millions of τ) is not known (and is also beyond the scope of the present study in terms of the associated computational cost), we can safely infer from these MSD plots that the particle will remain entrapped inside the solvated brush layer for a significantly large time duration.

Fig. 3.4(a) demonstrates the solvent "cage" effect by quantifying the time variation of the species (solvent molecules or the monomers) occupying the first solvation shell of the NP (for the case of NP of size 3σ) for two different $\frac{\varepsilon_{PN}}{\varepsilon_{LP}}$ ratios (namely, $\frac{\varepsilon_{PN}}{\varepsilon_{LP}} = 0.1$ and $\frac{\varepsilon_{PN}}{\varepsilon_{LP}} = 1$). Detailed procedure of such quantification has been provided in Appendix B. Clearly, we observe a larger encapsulation of the NP by solvent molecules (i.e., the presence of a larger number of solvent molecules in the first solvation shell of the NP) for the case of $\frac{\varepsilon_{PN}}{\varepsilon_{LP}} = 0.1$, as compared to that for the case of $\frac{\varepsilon_{PN}}{\varepsilon_{LP}} = 1$. These solvent molecules occupying the first solvation shell of the NP is considered to constitute the solvent "cage". In order to probe the stability of the solvent "cage", we also provide the time series data of the total number of NP-solvent direct contact pairs, $\overline{N}$ (i.e., the contact pairs that are associated with the formation of the solvent "cage") for these two cases [see Fig. 3.4(b)]. We clearly observe that the solvent "cage" is more prominent (and less fluctuating, as established below) for the case where the NP-polymer layer interactions are most unfavorable (i.e., with $\frac{\varepsilon_{PN}}{\varepsilon_{LP}} = 0.1$). From the time variation of the quantity $\overline{N}$, we can quantify the normalized fluctuations in the number of NP-solvent direct contact pairs (defined as $\chi = \sqrt{\langle \overline{N}^2 - \langle \overline{N} \rangle^2 \rangle} \Big/ \langle \overline{N} \rangle$, where $\langle \quad \rangle$ represents ensemble average), which is a measure of the stability

(greater this χ lesser is the stability) of the solvent "cage". We find that $(\chi)_{\frac{\varepsilon_{PN}}{\varepsilon_{LP}}=0.1} \approx 0.0822$ and $(\chi)_{\frac{\varepsilon_{PN}}{\varepsilon_{LP}}=1} \approx 0.2638$, confirming the larger stability of the solvent "cage" for a smaller $\frac{\varepsilon_{PN}}{\varepsilon_{LP}}$.

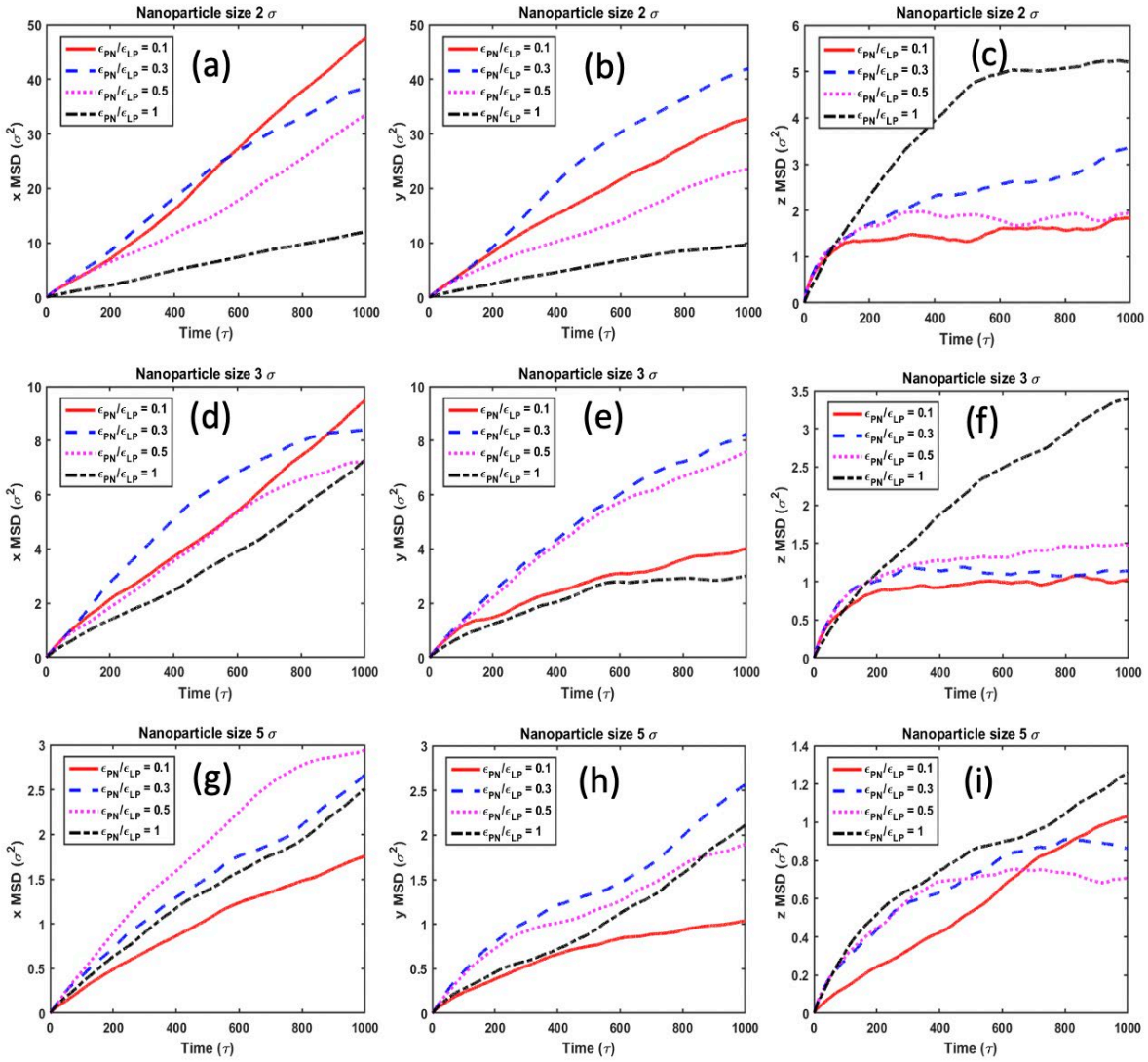

Figure 3.4. x, y, and z components of Mean Squared Displacement (MSD) of the NP inside the grafted polymer layer for different $\frac{\varepsilon_{PN}}{\varepsilon_{LP}}$ values and NP sizes.

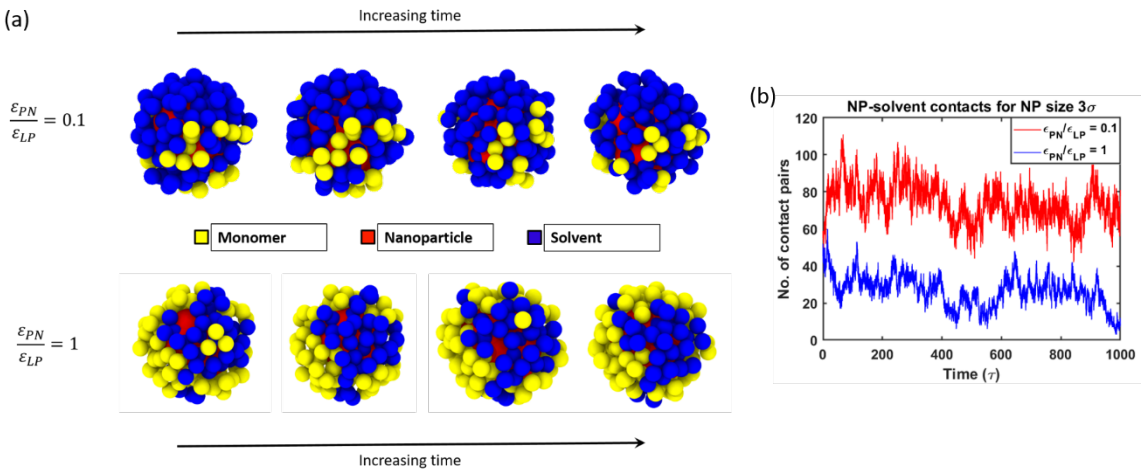

Figure 3.5. (a) Snapshots representing the time variation of the solvent "cage" around the NP of size 3σ for the most extreme cases of NP-polymer interaction strengths: $\frac{\varepsilon_{PN}}{\varepsilon_{LP}} = 0.1$ in the top row, and $\frac{\varepsilon_{PN}}{\varepsilon_{LP}} = 1$ in the bottom row. (b) The total number of NP-solvent direct contact pairs as a function of time for the aforementioned NPs.

As discussed in Fig. 3.3, the dependence of the stability of solvent "cage" around the NP on the values of $\frac{\varepsilon_{PN}}{\varepsilon_{LP}}$, for NPs of different sizes, is critical to explain the variation of NP MSDs as a function $\frac{\varepsilon_{PN}}{\varepsilon_{LP}}$. In order to quantify the stability of these solvent "cage", we studied the relaxation time distribution (RTD) of the solvent molecules in contact with the NP as a function of $\frac{\varepsilon_{PN}}{\varepsilon_{LP}}$ and the NP size (see Fig. 3.5). For the case of NPs of size 3σ, we observe that the RTD decays faster for the NPs with $\frac{\varepsilon_{PN}}{\varepsilon_{LP}} > 0.5$ than that for NPs with $\frac{\varepsilon_{PN}}{\varepsilon_{LP}} < 0.5$: this confirms that the solvent "cage" around the NPs (for NPs with $\frac{\varepsilon_{PN}}{\varepsilon_{LP}} > 0.5$) is much less stable enabling the NP to lose its solvent "cage" faster and to diffuse faster through the polymer layer. On the other hand, for the NPs of sizes 2σ and 5σ, the RTDs of the solvent molecules in contact with the NP show insignificant difference for different $\frac{\varepsilon_{PN}}{\varepsilon_{LP}}$ values: as a consequence, the effect of the solvent "cage" is irrelevant in determining the effect of $\frac{\varepsilon_{PN}}{\varepsilon_{LP}}$ values in the MSDs of the NP.

We can also provide a more physical understanding of why the solvent-case effect is witnessed only for a NP of size (or diameter) 3σ. The predominance of the solvent "cage" effect is determined by the interplay of factors such as the size of the NP, relative strength of the NP-polymer interactions (dictated by the $\varepsilon_{PN}/\varepsilon_{LP}$ ratio), and the grafting density of the polymeric layer. We consider the polymers to be having such a grafting density that ensures that the gap between the two adjacent polymer molecules (l) as 4σ. For a NP of size (or diameter) 2σ, the solvent cage effect leads to an effective size that is still significantly smaller than this gap (l) between the grafting sites of the polymer molecules: hence the solvent cage effect has insignificant impact on the motion of the NP of diameter 2σ. At the same time for a very large NP (size 5σ), the presence of the solvent cage does not lead to that significant a change in the size (as compared to the original size of 5σ): accordingly, for this case too, the solvent cage effect is less significant. On the other hand, the size of 3σ is that critical size, where the solvent cage effect leads to such an effective size of the NP that significantly impacts its dynamics, given the fact that the dynamics is controlled by the Steric hindrances imparted on the NP by the presence of the grafted polymeric layer (having a separation of l=4σ between the grafting sites of the adjacent polymer molecules). In summary, the solvent cage effect will be most prominent for that size of the NP, which in the presence of the solvent case effect, attains an effective size that is closely comparable to the space between the adjacent polymer molecules (as dictated by the value of l). For the present problem, this NP size is 3σ; obviously, if we had chosen a different value of the distance of separation l between the grafted polymers, the NP size for which the solvent cage effect would have been influential would be different.

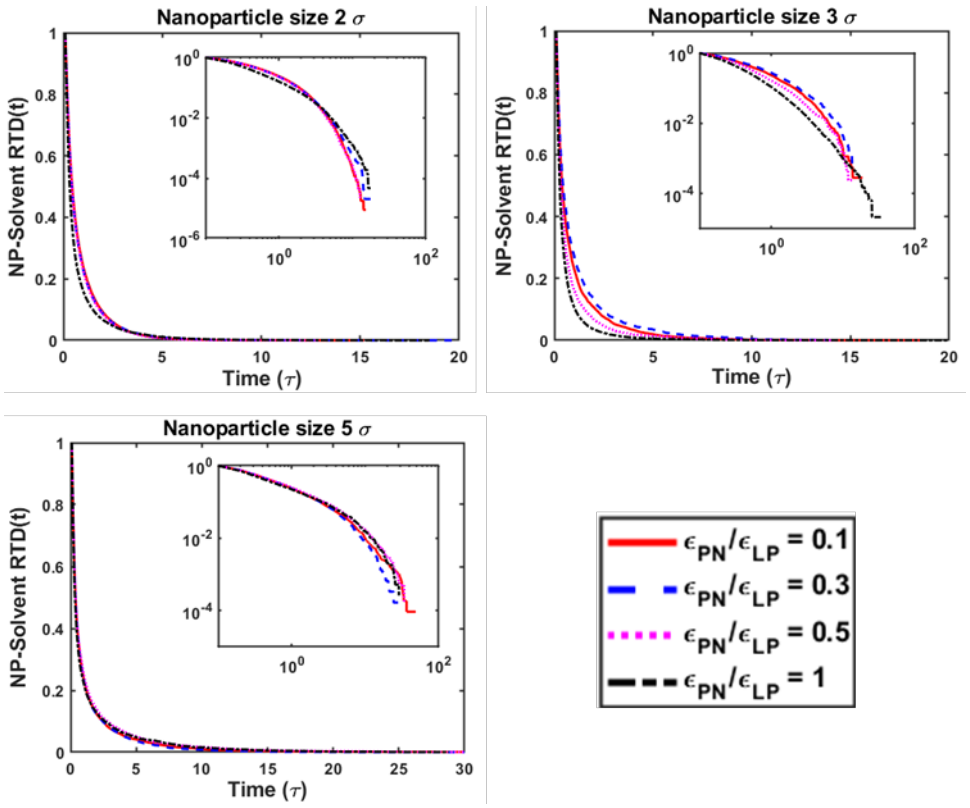

Figure 3.6. Relaxation time distribution (RTD) of the solvent molecules in contact with the NP as a function of the NP-polymer interaction strength for different NP sizes. The figures in the inset of provide the same variation of RTD with time in the log-log scale.

3.4 Discussions

A critical element of this study is opening up of the possibility of a much wide range of system choices for applications involving the interactions of NPs with a layer of polymer and PE molecules grafted on a solid surface. Typically, these applications involve the interactions of NPs with highly philic (with respect to the NPs) polymeric molecules. These polymeric molecules can either be in a fully pre-wetted state (and hence brush-like or coil-like states) or an originally collapsed state that gets wetted and hence transform into brush-like or coil-like state by the NP-carrying solvent. A very interesting and timely application of this second type of scenario is witnessed in the use of water-borne nanocoating for quick inactivation of SARS-CoV-2 and other virus NPs.[144] In this study, the authors demonstrated that when a water droplet carrying these virus particles impact on a dry surface grafted with a layer of collapsed polymer molecules [consisting of a polystyrene core with functional side groups containing N-isopropylacrylamide (NIPAM) and N,N- (dimethylamino)ethyl methacrylate (DMAEMA) and additional functional groups like polygalactose and guanidine for binding to the viral particles and degrading their RNA] present in the form of nanoworms, these polymer nanoworms stretch out and in the process ensures that the virus NPs get exposed to the functional groups of these nanoworms. Our present study establishes that under a judicious combination of the NP-carrying solvent and the grafted polymer molecules, one can not only introduce the NP (inside the polymer layer) but also ensure stable contacts between the NP and the polymer molecules even for the case where the polymer molecules are *substantially phobic* to the NP. Given that the virus inactivating action of the polymer molecules get triggered by the physical (or direct) contact between the NP and the polymer molecules, our findings raise the possibility of a design where virus NPs can be de-activated even by a polymer layer that is phobic to these virus NPs but philic to the solvent carrying these virus NPs inside the

polymer layer. This implies that our paper points to the possibility of fabricating a much more universal liquid-based nanocoating (in the sense that the nanocoating will function even when it is less philic to the incoming virus NPs) capable of inactivating the virus NPs.

Button *et al.* in a recent study proposed a new "gel-on-brush" mucus clearance model (such mucus clearance is the central mechanism that protects our lungs and airways from toxic substances).[150] In this model, it was proposed that the periciliary layer (PCL) consists of brushes that are tethered to the cilia. This proposed structure was key to prevent the mucins from the mucus layer and other toxic nanoparticles (NPs) from penetrating the PCL. This is an example where our present study can be strongly relevant by providing a foundation of understanding of how a toxic substance in the form of a NP (that has penetrated the mucus layer, specially under pathological condition where the mucus layer has been destroyed/damaged) can penetrate deeper into PCL by interacting with the cilia-bound brush layers (constituting the PCL).

For all other applications (such as fabricating nanocomposites, nano-sensors, or assembling and manipulating NPs using polymer brushes) that rely on ensuring such direct NP-polymer contacts, our study points to achieving the same degree of universality with a much broader choices of the polymeric materials that might even by phobic to the NPs.

While the model presented here considers simplistic LJ liquids, one can easily extend the possibilities revealed by the findings of this study to a more realistic system where the liquid is water and the polymer layer is hydrophilic. For such a case, the grafted polymer molecules might get swollen (into brush-like configuration) by the water vapor[168-170] even before the NP-laden water drop interacts with the polymer layer. Under such circumstances, while there might be some quantitative variation in the overall NP dynamics and the number and stability of the ensued NP-polymer direct contacts, we expect that the overall mechanism of the process, NP dynamics inside

the polymer layer, and the effect of different parameters (e.g., NP size, the value of the ratio $\frac{\varepsilon_{PN}}{\varepsilon_{LP}}$) will remain unchanged.

3.5 Conclusion

We have demonstrated the possibility of developing highly stable direct contacts between a NP and a polymeric layer that is extremely phobic to the NP. Interactions between NP and polymeric molecules form the cornerstone of a large number of applications with relevance in fields ranging from biomedical engineering to additive manufacturing: such interactions have inevitably been between NP and polymer molecules that are *philic* to the NP. Here, on the contrary the interactions are between a NP and polymer molecules that are *phobic* to the NP. Such a paradigm shift in the context of NP-polymer interactions become possible by driving the NP into the polymer layer by introducing the NP inside a liquid drop (with the liquid being philic to the polymer molecules). Once inside the polymer layer, the liquid molecules imbibe and diffuse; however, the NP experiences a retardation in its movement due to the Steric effect imposed by the polymer molecules. This ensures the localization of the NP within the polymeric layer and hence the development of stable NP-polymer contacts even when the NP-polymer interactions are extremely unfavorable. We also provide a detailed quantification of the role of the NP-polymer interaction energy and the NP size on the development of such NP-polymer contacts and the associated dynamics of the NP and NP-supported solvent molecules. Finally, we argue that our discovery of generating stable NP-polymer contacts for an energetically unfavorable NP-polymer system will be relevant for ensuring a much larger set of NP-polymer combinations for the different applications that depend on the existence of stable NP-polymer direct contacts.

Finally, we believe that our study, which probes a unique situation of a three-component system, has the potential to pave the way for a series of new research problems that take into account the following issues: (a) the liquid becomes phobic to the polymers, while the NP (encapsulated within the liquid) remains philic to both the liquid and the polymers; (b) there are

multiple NPs inside the drop and the NPs have shapes other than spherical;[171] (c) the NP is Janus-like, i.e., one hemisphere is philic and the other hemisphere is phobic to the polymer molecules; (d) the solvent themselves are composed of short polymers and there is a possibility of autophobic effect;[172] etc.

Chapter 4: Repeated Microphase Separation and Heating-Free Distillation-Like Behavior of Miscible Binary Liquid Mixture Using Nanoconfined Grafted Polymer Layers*

Abstract

Nanoconfinement is known to drive phase separation (often denoted as microphase separation) of two highly miscible liquids by subjecting the two liquids to disparate influences. Here we propose a paradigm shift to this problem: we introduce the idea of "repeatability" in nanoconfinement-driven microphase separation. A drop consisting of two highly miscible liquids (A and B) is made to pass through a nanochannel grafted with a collapsed layer of polymer that is philic to A, but phobic to B. Subsequently, a significant number of molecules of liquid A get imbibed into the polymer layer and the polymer layer partially swells, while the molecules of liquid B mostly remain out of the polymeric layer and are carried away, emerging as a drop on the other side of the polymer bilayer. This passage of drop (of liquids A and B) is continued and each time liquids A and B get separated with liquid A imbibing into the polymer layer and liquid B being carried away with the drop. This scenario, therefore, points to the repeated occurrence of the microphase separation of miscible binary liquid mixture, enabling the processing of a much larger volume of liquid, given the fact that the presence of grafted polymer layer continues to provide a dynamically increasing space where liquid A can get localized after being separated from liquid B. We quantify such repeated microphase separation by noting the extent of separation (of liquid A) and extent of recovery (of liquid B) as functions of nanochannel height and number of passes. Interestingly, we

* The contents of this chapter, excluding the results for nanoscale valving, has been submitted as the following journal article: Etha, S. A. & Das, S. Repeated Microphase Separation and Heating-Free Distillation-Like Behavior of Miscible Binary Liquid Mixture Using Nanoconfined Grafted Polymer Layers. *The Journal of Physical Chemistry B* (submitted for publication).
The results for nanoscale valving are being currently expanded for a second journal article from this chapter.

establish that this process also leads to a distillation-like behavior (without any heat addition), where the concentration of liquid B (equivalent to the "less volatile" liquid in a standard distillation process) progressively increases inside the drop after its passage through the nanochannel.

4.1 Introduction

The problem of microphase separation of highly miscible binary liquid mixtures (e.g., ethanol-water mixture, glycol-water mixture, mixture of isobutyric acid and water, etc.) have gained significant interests over the past couple of decades.[173-181] Such separation typically occurs when this miscible liquid mixture is enforced into a nanoconfinement (or confinement in general) and the two liquids respond differently to the confinement. For example, the nanochannel might be more philic to one liquid than another: under such circumstances, this liquid (to which the nanochannel wall is more philic) will prefer to remain localized at near-wall locations, while the other liquid is localized near the center of the nanochannel or nanopore. Separation of miscible liquids, in absence of any confinement, has been classically performed through many processes including fractional distillation. In fractional distillation, which is employed to separate two miscible liquids with different boiling points, the mixture of the two liquids is heated and the liquid with lower boiling point evaporates, thereby getting separated from the other liquid (or making the other liquid more concentrated).[182-184]

In this chapter, we propose a mechanism that uses nanoconfined grafted polymer layers to enable *repeated* microphase separation of a mixture of two highly miscible liquids (A and B), which have opposite interactions with the polymer chains (liquid A is philic, while liquid B is phobic to the polymer chains). Previous studies have reported confinement-driven separation of miscible

liquids:[173-181] our finding is a paradigm shift to this idea in the sense that we can ensure *repeated* microphase separation using the same nanochannel. To demonstrate the idea, we employ molecular dynamics (MD) simulations (see the Supplementary Materials for the details of MD simulations) to drive a liquid drop having an equal number of A and B molecules through a nanochannel with layers of collapsed polymer chains grafted on the nanochannel walls. During the process, depending on the nanochannel height, or the relative thickness of the polymeric layer with respect to the nanochannel height, some (or majority) of molecules of liquid A imbibe into the polymer layer, the polymer layer swells, and the drop containing a majority of molecules of liquid B is derived [Fig. 4.1(a)]. This is the microphase separation; however, this process can be *repeated* again and again (i.e., we can have multiple passes of the drop) until the polymer layers become fully saturated or overlap with each other [Fig. 4.1(b)]. Such *repeated* occurrence, which ensures the processing of a much larger volume of liquid, becomes possible since the presence of the grafted polymer layer that can progressively swell with the imbibition of the liquid A molecules continues to provide a *dynamically increasing space* for housing liquid A molecules separated from the drop (or liquid B molecules). There is a second effect of this process. After the passage of the drop through the polymeric layers, the drop will contain a much greater percentage of liquid B molecules as compared to that before the passage [Figs. 4.1(a,b)]. In other words, this scheme ensures a *distillation-like* behavior, where the density of one liquid (here, liquid B), in a miscible two-liquid mixture, increases progressively: of course, for our case, the process involves no boiling and a mismatch of the boiling points of the two liquids is not necessary.

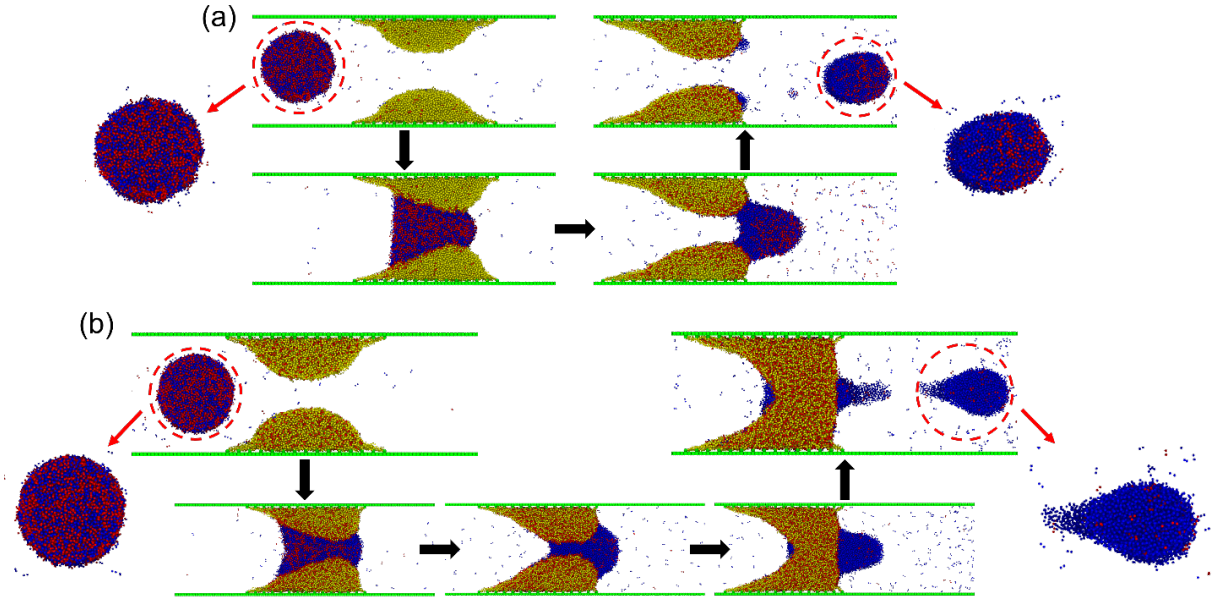

Figure 4.1. MD simulation snapshots summarizing the main findings. (a) A liquid drop consisting of equal number of A and B molecules (red dots: A molecules; blue dots: B molecules) pass through the grafted and collapsed nanoconfined polymer layer (philic to liquid A and phobic to liquid B) and in the process significant number of molecules of liquid A get separated from the drop (example of microphase separation), the polymer layer partially extends, and there is an enhancement in the fraction of liquid B molecules in the outgoing drop (distillation-like behavior). (b) The same microphase separation process repeated with the same nanochannel (but with an extended polymeric layer) leading to the removal of an even greater number of liquid A molecules from the drop and increasing further the fraction of liquid B molecules in the outgoing drop. The polymer layers overlap after this passage, making this nanochannel unusable for further drop passages.

4.2 Computational Methods

We employ Molecular Dynamics (MD) simulations to study the microphase separation behavior of a miscible binary mixture drop of two Lennard-Jones (LJ) liquids interacting with a nanoconfined grafted polymer layer. The MD simulations are conducted using the Large-scale Atomic/Molecular Massively Parallel Simulator (LAMMPS) software package.[168]

All species in our system interact through a standard Lennard-Jones 12-6 pair potential given by, $U_{LJ}(r) = 4\epsilon\left[\left(\frac{\sigma}{r}\right)^{12} - \left(\frac{\sigma}{r}\right)^{6} - \left(\frac{\sigma}{r_c}\right)^{12} + \left(\frac{\sigma}{r_c}\right)^{6}\right]$, where ϵ is the strength of LJ interactions, r is the distance between the centers of the interacting species, and σ is the size of the species. The cutoff distance, $r_c = 5\sigma$, is used for all non-bonded pairs unless explicitly mentioned. The polymer layer is chosen to have highly philic interactions with one of the liquids of the binary mixture (liquid A), while being phobic to the other liquid (B). We consider a 2D cylindrical drop containing a 1:1 ratio of the two composing liquids (A and B). The binary mixture drop is allowed to equilibrate before being driven towards the nanoconfined polymer layer with a constant force, emulating a pressure driven flow. We choose a simulation box of dimensions $L_x \times L_y = 225\sigma \times 40\sigma$. The height of the simulation box L_z varies across different simulations ($L_z = 40\sigma, 44\sigma, 48\sigma, 52\sigma$), and is the same as the nanochannel height. The simulation domain is periodic in y direction, but not in the x and z directions, where fixed boundary conditions are implemented.

We model the grafted polymer as linear chains with each chain consisting of 100 beads connected by permanent bonds. The Kremer-Grest (KG) technique detailed in chapter 3 was employed here to model the polymer molecules as approximately hard-sphered "beads" constrained by harmonic "springs". We consider a nanoconfined polymer bilayer with chains grafted on opposing planar surfaces having a separation of h. Each surface is grafted with 150 chains with a grafting density (σ_g) of $0.056/\sigma^2$, for a total of 300 nanoconfined polymer chains. The polymer beads are

connected by bonds modeled using the finitely extensible nonlinear elastic (FENE) potential, $U_B = -0.5KR_0^2 \ln\left[1 - \left(\frac{r}{R_0}\right)^2\right]$, where r is the separation distance, R_0 = 1.5σ, and K = 30ϵ/σ^2. We introduce stiffness in our grafted polymer chains via the application of a bending potential following the Faller and Müller-Plathe[187] augmented KG modelling procedure given by, $U_{bend}(\theta) = \epsilon[1 + \cos(\theta)]$, where θ is the angle subtended by adjacent bonds. The two liquids in our simulation are modelled as dimers made of LJ beads, having the same FENE bond parameters as the polymer chain. All liquid and polymer beads have a mass m. All bonded pairs of neighboring beads on a polymer chain interact through the standard LJ 12–6 pair potential as given above, but with a cutoff distance of $r_c = 2^{1/6}\sigma$. A purely repulsive LJ wall is placed at the right and left faces of the simulation domain to prevent the liquid molecules from escaping. The nanochannel is modeled as fixed walls of beads uniformly distributed with an area density of 1 m/σ^2 interacting with all other species via the 12–6 LJ potential with a cutoff distance of $r_c = 2^{1/6}\sigma$. We do not consider any Coulombic interactions in our system and the nonbonded interactions only include a shifted-truncated 12–6 LJ potential. As such, the model adopted in this study is appropriate for systems dominated by van der Waals interactions. We summarize the LJ interaction parameters used in our system in Table 4.1 below (in the table, r_c denotes the cutoff for the LJ interactions). Also, the beads representing the different species (e.g., liquid molecules, monomers, and wall molecules) are all identically sized (σ = 1).

The simulations are carried out in an NVT ensemble using the Nosé-Hoover thermostat.[169,170] All simulations are performed using a timestep of 0.001τ and the damping factor of the thermostat is considered to be 100 timesteps (0.1τ). We start the simulation with the reduced LJ temperature of all particles set at T* $\left(= \frac{Tk_B}{\epsilon}\right)$ = 0.1, and by gradually increasing the temperature to T* = 1, while keeping the binary mixture drop fixed at a large enough distance away from the grafted polymer

molecules (inside the nanochannel) so that the drop-polymer interactions are negligible. Initially, the polymer layer is "dry", meaning it is not solvated.

Table 4.1: Strength and cut-off distances of the LJ interactions between different species

Particle Type A	**Particle Type B**	$\boldsymbol{\varepsilon_{LJ}}$	$\boldsymbol{r_c\ (\sigma)}$
Wall	Wall	0	-
Wall	Polymer/Liquid bead	1	1.12
Polymer Bead	Polymer Bead	1	5
Polymer bead	Liquid A	1.5	5
Polymer bead	Liquid B	0.3	5
Liquid A	Liquid B	1	5

We consequently drive the cylindrical drop in the x-direction with a constant force on each drop molecule that emulates a pressure gradient of $0.009\ \epsilon/\sigma^4$, in order to push the drop through the nanoconfined polymer bilayer. The drop is allowed to gradually pass through the polymer layer; the polymer bilayer absorbs a fraction of the philic liquid (A) molecules and a corresponding drop containing a majority of phobic liquid (B) molecules is obtained on the other side of the nanoconfined polymer layer. This is defined as one "drop pass". At this stage, the drop obtained after the passage is deleted from the system and the polymer bilayer is equilibrated without the application of a pressure gradient force. The attainment of equilibration is confirmed by the autocorrelation function of the polymer layer heights. Once equilibrated, a binary mixture drop (same as our initial drop) is added back into the system, allowed to stably equilibrate far away from the polymer layer, and then pushed towards the polymer layer (with the same force), to obtain

"pass 2". This process is repeated to obtain multiple passes for a given nanochannel height, until the polymer bilayer interpenetrates. Of course, different nanochannel heights accommodate different number of total drop passes. We collect data every 0.5τ. All visualizations of the atomic trajectories are performed using the open-source software OVITO.[172]

4.3 Results

Repeated Microphase Separation and Distillation-Like Behavior: Process Description

We consider a drop of highly miscible binary mixture of two Lennard Jones (LJ) liquids A and B (their high miscibility is ensured by considering a dimensionless value of their interaction energy, $\varepsilon_{AB} \to 1$) that is driven (by applying a finite force) through a nanochannel whose two walls are grafted with *collapsed* layers of polymer chains (P). The drop contains an equal number of A and B molecules. The polymer chains are so chosen that they are philic to liquid A (i.e., $\varepsilon_{AP} \to 1$), but phobic to liquid B (i.e., $\varepsilon_{BP} \to 0$).

We show here the MD simulation snapshots for two separate cases: nanochannel with height 52σ (Fig. 4.2) and 40σ (Fig. 4.3) (σ is the LJ length parameter).

For the nanochannel with height 52σ, as the drop (consisting of liquids A and B) comes in contact with the collapsed polymeric chains, some of the molecules of liquid A get imbibed/infused into the polymer layer (and the polymer layer partially extends), while the drop now containing a much greater fraction of molecules of liquid B, passes through. This is the 1st stage of microphase separation. For this case, the separation process can be repeated as many as five times: each time we consider the liquid-infused nanoconfined polymer layer that resulted from the separation during the previous pass, but start with a drop that has an equal number of A and B molecules. Each time we get the separation with molecules of liquid A leaving the drop and entering the polymer layer, while the drop passing through with much greater fraction of molecules of liquid B. In addition to this separation, there is also a progressive swelling of the polymer layer and at the end of the fifth

pass, the polymer layers overlap: no further pass is carried out, given the fact that such overlapped polymeric layers block the drop passage.

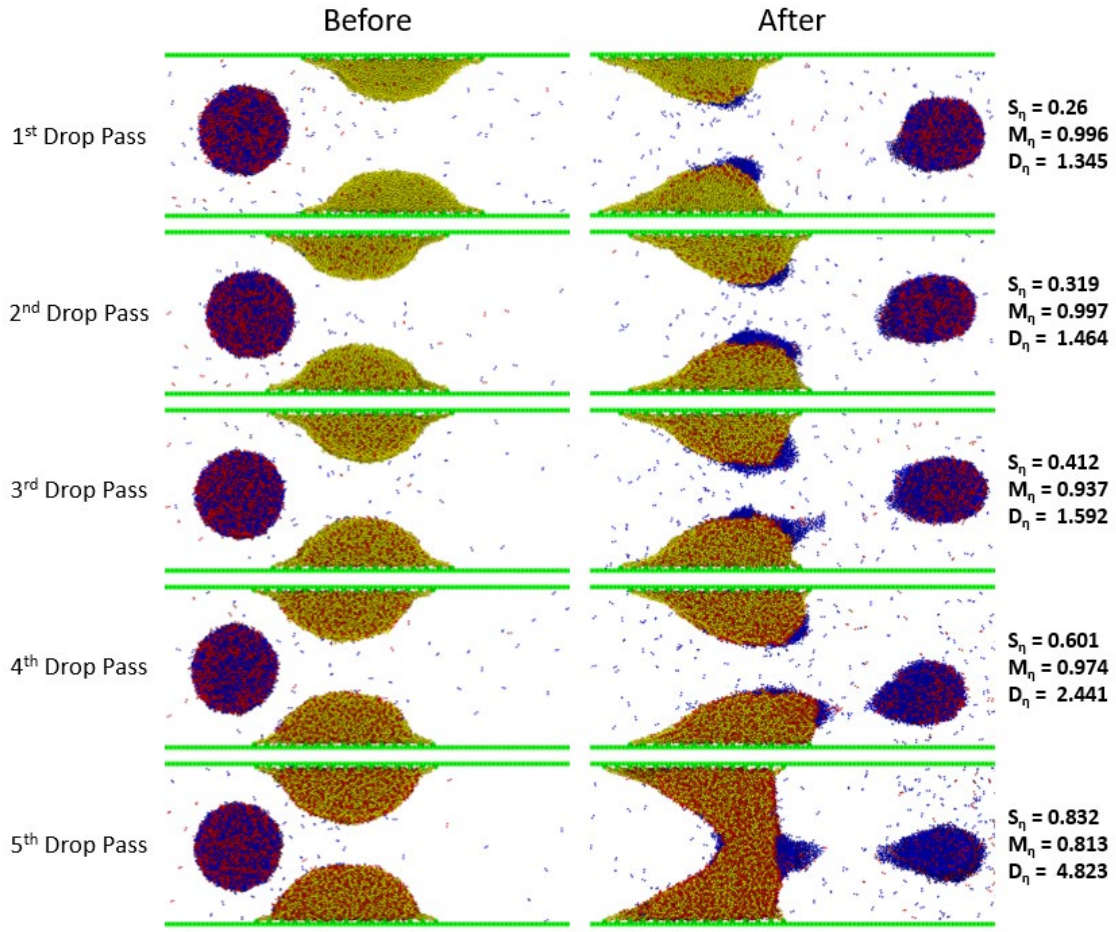

Figure 4.2. MD simulation snapshots showing the passage of the liquid drop through the nanoconfined polymer grafted layers for the nanochannel of height = 52σ. This nanochannel allows for 5 passages of the drop (hence the *microphase separation process* and distillation-like behaviors get repeated 5 times). On the margin of the figure showing each pass, we identify the corresponding parameters (discussed later) quantifying the separation (S_η, M_η) and distillation-like behavior (D_η).

For the case of the nanochannel with height 40σ, only one pass of the drop is possible and after that pass the collapsed polymer layers swell and interpenetrate (thereby preventing further passes) (see Fig. 4.3). Interestingly, for this case (as will be established later), we get near complete separation, i.e., almost all the liquid A molecules leave the drop and enter the polymer layer, while the drop that comes out is almost entirely composed of liquid B. While these are excellent metrices, the challenge is that such a scheme allows the handling of a much smaller volume of the liquid, as compared to that achieved where one can employ multiple passes (see Fig. 4.2).

We study cases for two more nanochannel heights: h=44σ and h=48σ. Both these cases enable multiple passes of the drop, thereby resulting in *repeated* microphase separation and distillation-like behaviors. The corresponding simulation snapshots have been provided in Appendix C. Additionally, we have provided movies as supporting material showing the drop passes for different passes for the case of a single nanochannel height.

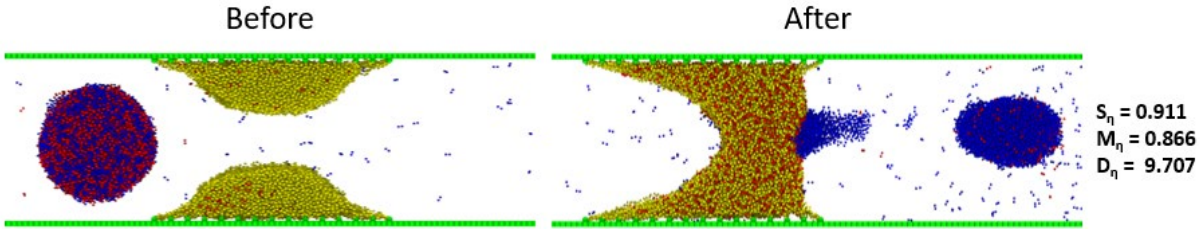

Figure 4.3. MD simulation snapshots showing the passage of the liquid drop through the nanoconfined polymer grafted layers for the nanochannel of height = 40σ. This nanochannel allows only one pass. On the margin of the figure, we identify the parameters (discussed later) quantifying the separation (S_η, M_η) and distillation-like behavior (D_η).

In addition to this microphase separation, we also notice a fractional-distillation-like behavior. Fractional distillation refers to a progressive increase in the concentration of one component in a binary, miscible liquid mixture under the setting where one liquid is more volatile and hence when subjected to heating evaporates and leaves the mixture. A more efficient distillation implies a greater concentration of the less volatile mixture. In the present case, liquid B behaves like the "less volatile" liquid present in the mixture (of course there is no heating or no evaporation of any liquid): depending upon the nanochannel height and the specific number of the pass, the concentration of liquid B in the drop that has passed through the nanochannel can be much higher than that in the drop before the passage of the drop through the nanochannel. Thus, we start with a drop that is a mixture of equal number of molecules of two highly miscible liquids (A and B) and "concentrate" (or "distill" the drop) with respect to liquid B molecules by simply passing it through the nanoconfined grafted polymeric layer. Most remarkably, by controlling the nanochannel height and the number of passes, we control the "extent" of this "distillation", i.e., the extent to which the drop gets concentrated with respect to the liquid B (detailed quantification has been provided later).

Quantification of the multi-step (repeated) microphase separation and distillation

First, we quantify this multi-step (or repeated) microphase separation. At each separation step (or each pass), certain number of molecules of liquid A leave the drop and settle inside the polymeric layer. Each pass starts with a fixed number liquid A molecules ($N_{A,i}$) mixed with an equal number of liquid B molecules ($N_{B,i}$, where $N_{B,i}=N_{A,i}$). Depending upon the nanochannel height and the pass number, only a certain number of molecules of liquid A leave the drop and imbibe inside the

polymer layer, leaving behind $N_{A,f}$ number of liquid A molecules inside the drop. Obviously smaller the value of $N_{A,f}$, better is the separation. Therefore, we define the separation efficiency S_η as

$$S_\eta = \frac{N_{A,i} - N_{A,f}}{N_{A,i}}. \quad (1)$$

Fig. 4.4(a) provides the variation of S_η as a function of the nanochannel height and the pass number.

S_η increases with the number of passes for a given nanochannel gap: this implies that for the higher pass number a greater fraction of liquid A molecules is removed from the passing drop. As the number of passes increases, the degree of swelling of the polymer layer increases thereby providing a greater space for the liquid A molecules (philic to the polymer layer), thereby enforcing the removal of a greater fraction of the liquid A molecules from the drop during the drop passage.

Just the variation of S_η is insufficient to completely quantify the separation efficiency. During the passage of the drop, some of the molecules of liquid B leave the drop and get attached to the polymer layer as they are attracted to the significant amount of the molecules of liquid A (given liquid A and B are philic to one another) that have already imbibed into the polymeric layer (see Fig. 4.2). Accordingly, in addition to quantifying the extent of removal of liquid A molecules (quantified by S_η), one also needs to calculate the mass recovery efficiency (M_η) of liquid B, where:

$$M_\eta = \frac{N_{B,f}}{N_{B,\mathrm{i}}}, \quad (2)$$

with $N_{B,\mathrm{i}}$ and $N_{B,\mathrm{f}}$ being the number of liquid B molecules inside the drop before and after its passage through the polymer-grafted nanochannel.

The best scenario for the separation is represented by a simultaneously large value (near unity) of S_η and a large value (near unity) of M_η.

M_η shows a non-monotonic dependence on both the number of passes and the nanochannel height [Fig. 4.4(b)]. During the greater-numbered pass, liquid B molecules interact with liquid-A-molecule-laden polymeric layer: the philic A-B interactions will enforce some B molecules to leave the drop and get retained back onto the polymer layer, thereby reducing M_η. There is another effect that counters this situation. As is evident from the variation of S_η, an increase in the number of passes increases the fraction of the liquid A molecules that are removed from the passing drop and get adsorbed into the polymer layer. This leads to a more wetted polymeric layer and a correspondingly more phobic drop with respect to the polymer, which in turn reduces the friction (and the resulting shearing force) on the ejaculated drop, thereby reducing the number of B liquid molecules that get detached (due to this shearing force) from the drop and localize on the polymeric layer. This event enhances M_η. Therefore, there are competing factors in play (one decreases and one increases M_η), which depend on the pass number (and hence the nanochannel height), thereby ensuring that M_η varies non-monotonically with the pass number and nanochannel height. The above reported shearing action can be more clearly observed in the videos provided as supporting material.

We finally quantify the distillation-like behavior of the drop with regards to increasing the concentration of liquid B inside the drop. This distillation-like behavior can be quantified by the parameter

$$D_\eta = \frac{N_{B,f}}{N_{A,f}}. \qquad (3)$$

Greater the value of D_η, greater is the fraction of molecules of liquid B inside the drop after the passage of the drop through the polymer grafted nanochannel. By this definition, perfect distillation would warrant that D_η tends to infinity. Given that we always have $N_{B,i} = N_{A,i}$ inside the drop before its passage through the nanochannel (regardless of the pass number), we can use eqs.(1,2) to re-express eq.(3) as:

$$D_\eta = \frac{M_\eta}{1-S_\eta}. \qquad (4)$$

Fig. 4.4(c) provides the variation of D_η as functions of the nanochannel height and the pass number. Despite the non-monotonic nature of M_η (with respect to the pass number), we find that D_η increases monotonically with the pass number. This stems from the progressive (and significant) increase of S_η with the pass number. In other words, at higher pass numbers, the extent of the removal of liquid A molecules from the drop is so high that the extent of the corresponding removal (or the lack of it) of the B molecules from the drop becomes less significant. Fig. 4.4(c) also confirms that for certain nanochannel heights, the increase in the pass numbers leads to D_η values that are much larger than the D_η for the nanochannel that allows only one pass (e.g., h=40σ). In

fact, such enhanced values at greater pass numbers, as compared to the case (nanochannel with h=40σ) that allows only one pass, can also be observed at some instances for S_η and M_η.

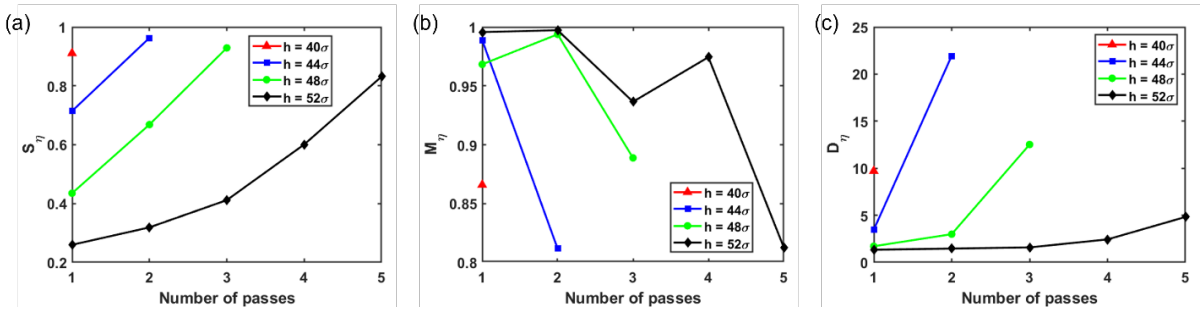

Figure 4.4. Variation of (a) S_η, (b) M_η, and (c) D_η with the nanochannel height and the number of passes (the allowed number of passes increases with the nanochannel height).

Quantification of the structure of the liquid-imbibed polymeric layers and the distribution of the liquid molecules across the polymeric layers

In Fig. 4.5(a-d), we plot the monomer profile of the polymer layer for different nanochannel heights, before (dashed) and after (solid) the final pass that is allowed by the corresponding nanochannel. Consequently, for each case, the monomer profiles (after the drop passage) will exhibit interpenetration. Beyond this point, no phobic liquid (liquid B is phobic to the polymeric layers) is permitted through the nanochannel (at least with the usual magnitude of force). This scenario resembles that of a "valve": we shall explore this idea in the next section. Interestingly, for all the cases shown in Figs. 4.5(a-d), the interpenetration length of the resulting polymer

structure is identical in magnitude to the minimum gap (represented as the distance between the red and blue dotted lines) between the opposing polymer layers before the final drop pass.

Finally, in order to show the progressive swelling of the polymeric layers after every pass, we provide the monomer profiles after all passes for the nanochannel height h=52σ (which allows the maximum number of passes). The dry polymer height is represented by the case of pass "0". The progressive increase in the polymer layer height (until the polymer layers overlap) with the number of drop passes becomes evident from the presence of a finite monomer concentration at a *z* value that is further away from the grafting location (at z=0σ and z=52σ) for a higher pass number; of course, this also means a progressive decrease in the peak monomer density values in order to conserve the total mass of the polymer layer and this conservation has been verified by matching the area under the monomer profile curves for all passes.

The corresponding density distributions for liquids A and B inside the polymer layer, as functions of the nanochannel height and number of passes, have been provided in Appendix C.

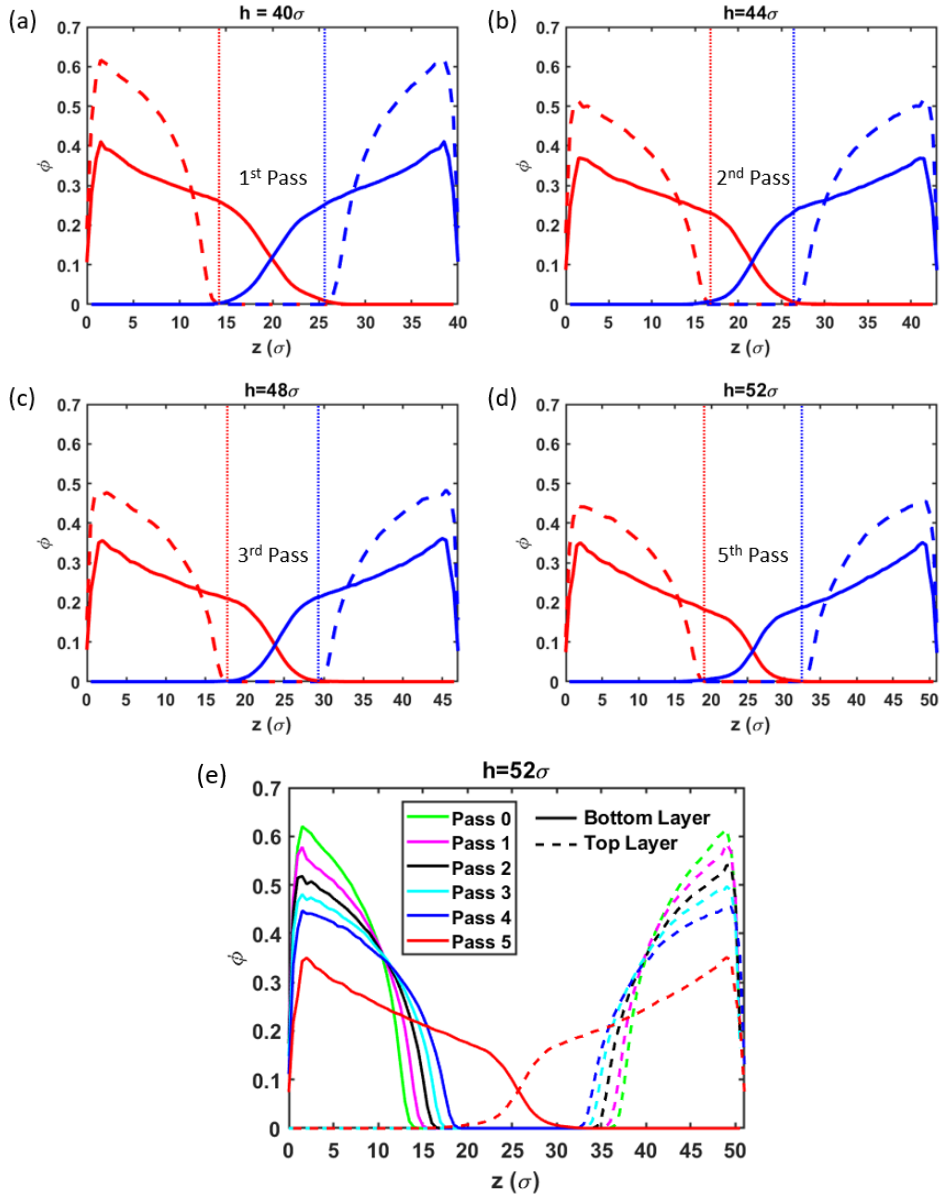

Figure 4.5. Monomer distribution of the nanoconfined polymer layers before and after the final (allowed) drop pass for the nanochannel with (a) h=40σ, (b) h=44σ, (c) h=48σ, and (d) h=52σ. (e) Monomer distribution of the nanoconfined polymer layers after each of all the five allowed drop passes (Pass "0" refers to the case before any pass) for h=52σ.

Universal Nanoscale Valves for On-Demand Liquid Release Using Liquid-Infused Grafted Polymer Layers

In the previous sections of this chapter, we have elucidated the manner in which the nanoconfined grafted polymer layers interact with a drop of highly miscible binary liquid mixture and in the process separates the two liquids, with one liquid (the one to which the polymer layers are philic) getting imbibed into the grafted polymer layers, while the other liquid or the majority of the other liquid (the one to which the polymer layers are highly phobic) being driven away with the drop. Such liquid imbibition into the polymer layers swells the polymer layers, ensures repeated separation of the two liquids, and leads to the formation of the liquid-infused grafted polymer layers. In fact, such liquid-infused grafted polymer layers, can get swelled to such an extent that they interpenetrate. One can recall that we stop the repeated passes of the binary liquid mixture drop once the liquid-infused polymeric layers attain such interpenetrated state.

In this section, we demonstrate the *on-demand* pressure-driven nanovalving of desired volumes of a given liquid (in this case, the liquid that is phobic to the polymer layers, namely liquid B, which is shown by blue colored particles and have $\varepsilon_{BP} \ll 1$) using such nanoconfined liquid-infused and interpenetrating grafted polymer layers. This partially swollen polymer bilayer is solvated by liquid A (depicted by red colored particles), which is philic to both liquid B ($\varepsilon_{AB} \to 1$) as well as the polymer species ($\varepsilon_{AP} > 1$). As discussed in the previous section, the interaction of liquid A with the grafted polymer layers ensures that the polymer partially swells, as the polymer layer changes from being in contact with a "poor" solvent, (i.e., vacuum) to a "good" solvent (i.e., liquid A) (see Fig. 4.5). On the other hand, the molecules of liquid A now get "housed" inside the partially swollen polymeric layer. This ensures attainment of liquid-infused grafted polymeric bilayer. Development of such liquid-infused swollen polymeric layer occurs at the opposing walls of the

nanochannel, and as a result, they exhibit weak interpenetration. This overlapping polymer structure is in the form of a liquid-laden porous barrier to any incoming liquid (see Figs. 4.2 and 4.3). More importantly, this liquid-laden porous barrier has two disparate components in the context of possible interactions with an incoming (in presence of a finite pressure gradient) column of another liquid B: first it consists of the segments of polymer P (which are phobic to the incoming liquid B) and second it contains molecules of liquid A (which are philic to the incoming liquid B). Therefore, when a column of liquid B is subjected to a sufficiently large pressure gradient and driven through this liquid-infused polymeric barrier, a tiny amount of the incoming liquid B molecules is absorbed into the layer (stemming from the favorable interactions between the molecules of liquids A and B), while most of the incoming liquid B molecules pass through the liquid-infused polymeric barrier (see Fig. 4.6). We consider a reservoir of liquid B with a specified amount of liquid molecules ($\sim 0.75 \times 10^6$) at a given pressure $p_{reservoir}$. This fluid reservoir is connected to the polymer grafted nanochannel that has a "sink" attached to it on the other side (the sink is initially maintained at vacuum). For this incoming column of liquid interacting with nanoconfined LIGPL (liquid-infused grafted polymer layer) for a given nanochannel height, the flow rate of liquid B (or effectively the total number of liquid B molecules per unit time) that passes through the liquid-infused polymeric barrier can be precisely controlled by controlling (a) the magnitude of the pressure at which the reservoir containing liquid B is maintained, or effectively the strength of the pressure gradient ($\Delta p/l$) to which the molecules of liquid B have been subjected to, (b) the number of molecules of A present inside the LIGPL, and (c) the height of the nanochannel. In Fig. 4.7., we demonstrate the effect of the nanochannel height in dictating the flow rate of liquid B (or effectively the total number of liquid B molecules per unit time) that passes through the liquid-infused polymeric barrier. This ability to regulate the extent of liquid B

molecules that comes out of the LIGPL barrier is referred to as the valving action. Salient features of this valving mechanism are as follow: (a) unlike several existing techniques, this strategy is not a go-vs-no-go strategy; rather, here one can precisely control the flow rate of liquid B that one wants; (b) this strategy is a very generic and universal one that can be employed for valving liquid B (where B can be any liquid): it will work whenever we have another liquid A and a polymer P, such that $\varepsilon_{AB} \to 1$, $\varepsilon_{AP} > 1$, and $\varepsilon_{BP} < 1$.

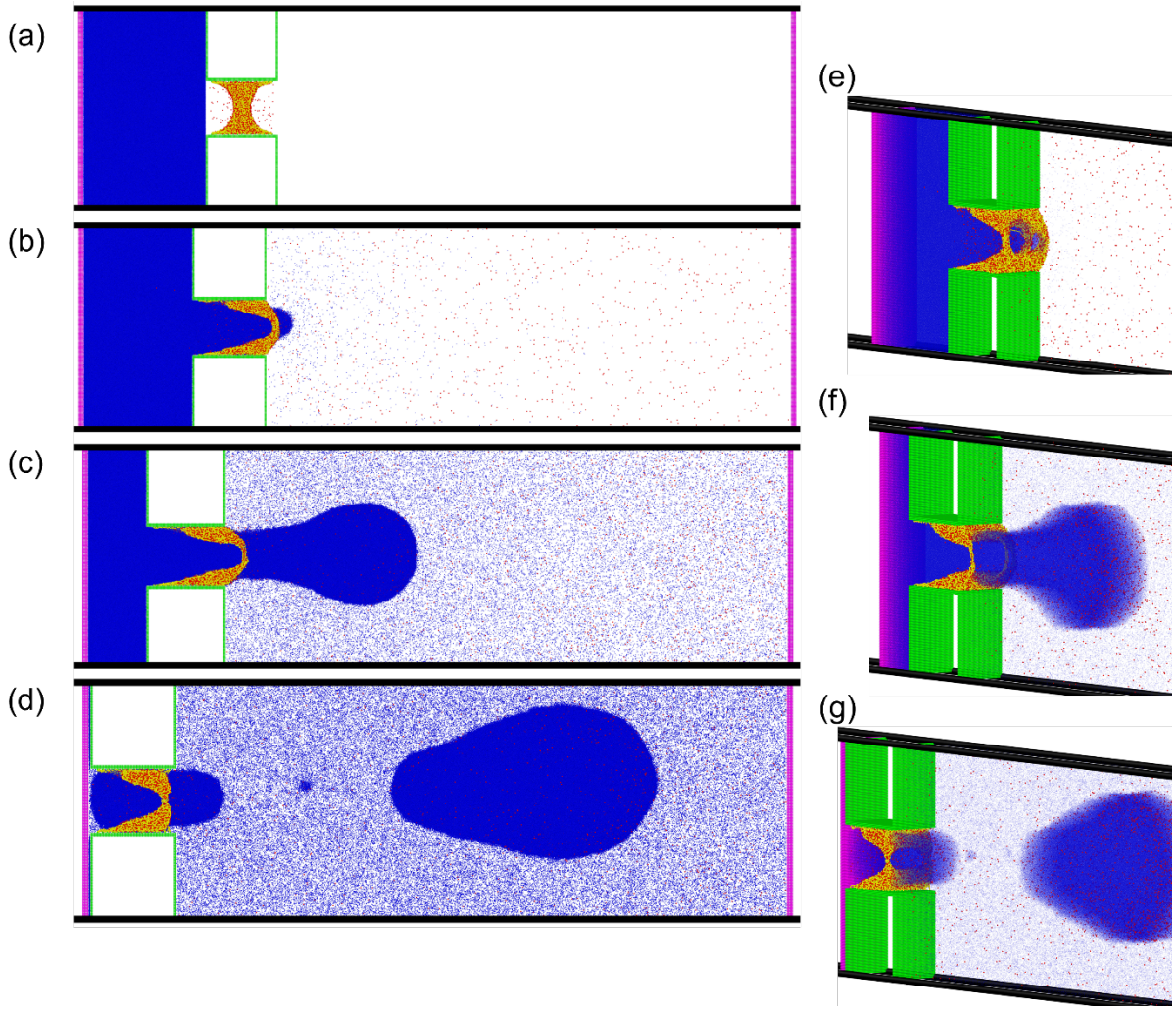

Figure 4.6. (a-d) MD simulation snapshots showing the passage of the phobic liquid drop through the nanoconfined polymer grafted layers for the nanochannel of height = 52σ at times (a) t=0, (b) t=, (c) t=, (d) t=. Subfigures (e)-(g) are magnified versions of subfigures (b)-(d) respectively, with the phobic liquid made partially transparent for better visualization of the polymer layer.

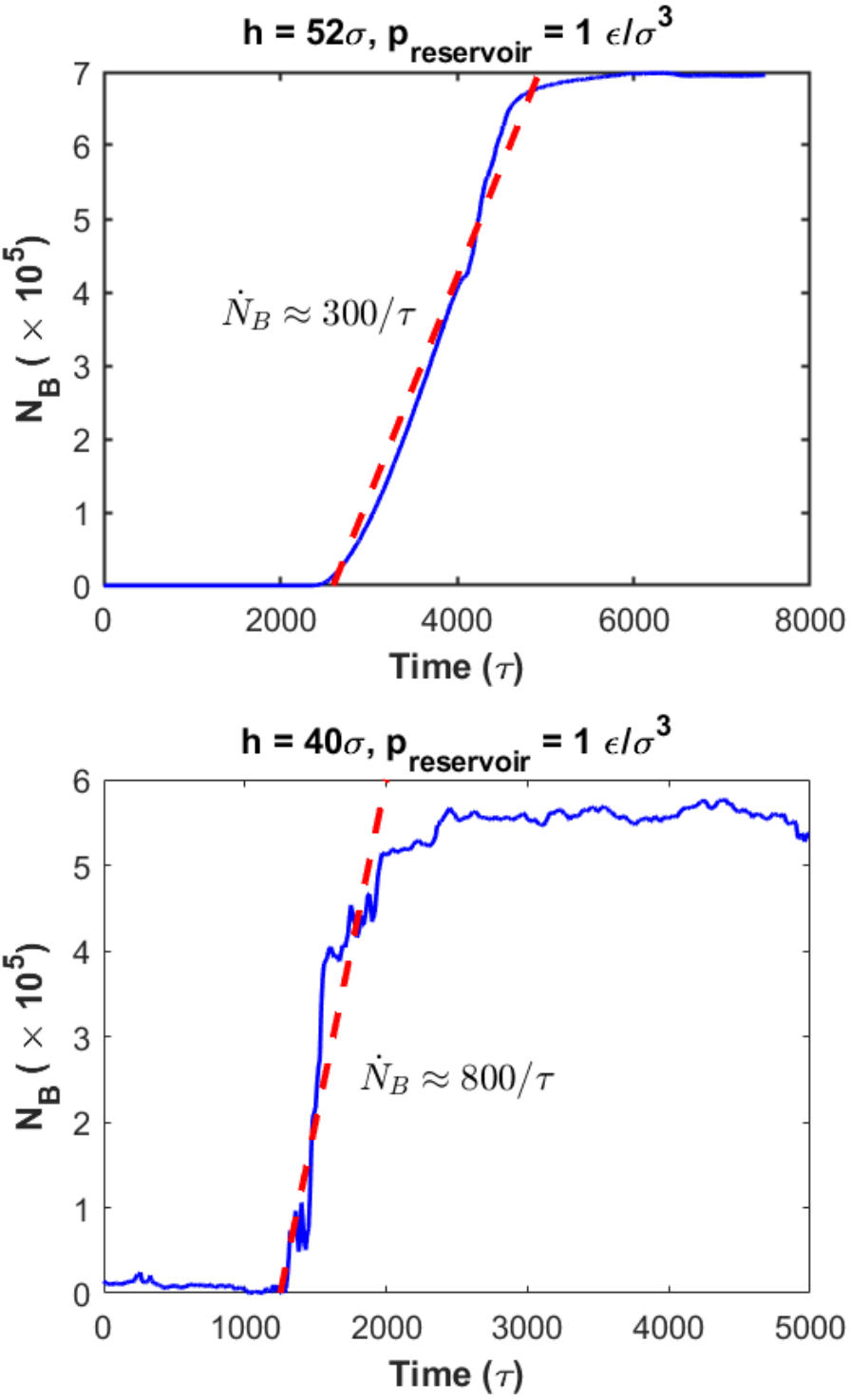

Figure 4.7. Time variation of the number of molecules of liquid B (which also provides the flow rate of liquid B molecules, $\dot{N}_B$; we have indicated the $\dot{N}_B$ in each sub-figure) that pass through the liquid-A-infused interpenetrated nanoconfined polymer layer for a nanochannel height of (a) 52σ and (b) 40σ. For both the cases, we consider a reservoir pressure of $p = 1\epsilon/\sigma^4$ (is it p or Δp/l?).

4.4 Discussion

In this work, we employ a modified version of the generic polymeric modelling procedure introduced by Kremer and Grest (KG).[162] This assumes that the polymer can be approximated as spherical beads constrained by harmonic potential bonds that interact via van der Waals forces and exhibit some degree of stiffness. Although previous work[163] has illustrated the universality of Kuhn scale-mapped KG in predicting the emergent properties of polymer systems, like entanglement modulus and more indirectly, macroscopic properties like non-Newtonian polymer rheology, care has to be taken to apply the correct values of characteristic Kuhn scale properties of the polymer molecules for an accurate match with commodity polymers. In our work, we have used a model polymer length of 100 beads. Depending on the polymer being modelled, this may be insufficient to observe entanglement scales that would dictate features of such filtration and valving phenomena beyond the molecular scale. More precisely, the grafted polymer molecules in the long chain limit would exhibit a greater degree of dependence on the entanglement effects in polymer chains including constraint release[188-192], and crumpling[193-196] as well as correlation hole effects[197], that may help explain the nonlinear rheology of more macroscopic polymeric systems. The rheology would affect how large the forces of interaction become beyond the Kuhn-scale for a given set of materials impacting the feasibility of such applications. Of course, other chemistry-specific effects are disregarded in this approach, especially electrostatic effects, that might be important depending on the context. Another important consideration is the fracture limit of such grafted polymer chains (or even creep failure) under action of high forces/pressures subjected in our systems. However, we believe this work provides a robust treatment of commodity polymer properties and the framework developed here can be expected to provide good predictions outside the linear regime and help establish a direct, quantitative link to experiments. In our work, we also

consider a very simple treatment of the solvent species and do not consider any nonlinear effects like viscoelasticity or chemical specific effects to be important for the fluid interactions. Therefore, above all else, this work merely suggests the possible feasibility of such filtration and fluidic valving applications by providing a customizable modeling procedure to account for the discrepancy in different characteristic time and length scales exhibited by polymer species and hence requires a thorough experimental validation of these phenomena with the right selection of material properties.

4.5 Conclusion

Here, we have proposed a design strategy that uses nanoconfined grafted polymer layer to trigger repeated microscopic phase separation (such repetition enables processing of significant volumes of liquids) of a binary mixture of two miscible liquids (A and B) that show opposite interactions with the polymeric layer. Using nanochannel to trigger microscopic phase separation of miscible liquids, by leveraging the disparate interactions between the liquids and the nanochannel wall is well known: here we propose a paradigm shift to this problem by demonstrating that such separation can be triggered in a repeated fashion by using nanoconfined polymer layers that interact favorably with one of the liquids (liquid A) and thereby progressively swell providing a progressively increasing space to this particular liquid to get separated from the mixture. We additionally demonstrate that the same process leads to a distillation-like behavior, where there is a continuous enhancement (with each repeat of the separation event) of fraction of liquid B in the mixture. We use quantifications to provide a measure of the extent of separation and the extent of distillation-like concentration enhancement, and show that repeated passes can also improve these measures. Finally, we demonstrate that the nanoconfined interpenetrated liquid-infused (with liquid A) polymeric bilayer structure that results from such multi-step separation can be utilized

as a nanoporous liquid valve that can be used for controlled valving of desired amount of the other liquid (liquid B) by driving a column of liquid B through this interpenetrated polymeric bilayer in presence of an externally imposed pressure gradient.

Chapter 5: Conclusion and Future Scope

This thesis explores the atomistic level dynamics of liquid drops and nanoparticles interacting with grafted polymer layers showing a varied range of interactions with these moieties. In the process of this exploration, we are not only able to shed light on the fundamental behavior of drops and NPs in contact with the polymer layer and the responses of the polymer layer to these entities, but also provide ideas of a host of different application designs involving NPs, liquids, and polymers.

First, I uncover the fundamental wetting dynamics of a liquid drop simultaneously spreading and imbibing into a polymer layer, which itself responds to the drop and undergoes a collapsed-state-to-brush-state transition. I quantify the process by describing the drop spreading by scaling laws that match reasonably well with the MD simulation results. We also describe the imbibition dynamics and the collapsed-state-to-brush-state transition dynamics of the grafted polymer layers. Finally, we argue that the process could provide clues to developing "responsive" polymer grafted liquid infused surfaces.

Second, I study the interaction of NP-laden liquid drop with a layer of grafted polymers. The salient feature of this system was that the NP was phobic to the polymer, while the drop carrying the NP was philic to both the NP and the polymer layer. Such a scenario led to the most remarkable onset of stable physical contacts between the NP with the polymer layer, despite the polymer layer being highly repulsive to the NP. The study provided one of the first design approaches that enable stable contacts between a NP and a highly unfavorable functionalized layer: this design, we argued, could well increase the versatility of the designs and applications where such NP-functionalized-layer interactions become the main driving factor.

Third, I studied the interactions between nanoconfined grafted polymer layers with a drop of highly miscible binary liquid mixture. The salient feature of this particular set up was that the two liquids, constituting the liquid drop, showed completely different interactions with the polymer layer. When a drop of this binary and miscible liquid mixture was driven through the nanoconfined polymeric layers, the liquid that was philic to the polymeric layer got imbibed into the polymer layer and as the polymer layer swelled, while the other liquid (phobic to the polymer layer) mostly passed through. This action ensured the first stage of separation. Most intriguingly, the swelling of the polymeric layer was progressive, providing further space to the philic liquid to get imbibed into the polymer layer. This paved the way for the multiple stages of this separation. We also showed that this same principle of the interaction of multiple miscible liquids with nanoconfined polymer layers showing distinctly different interactions with the liquids can be utilized for ensuring nanoscale fluid valving, where one of the liquids (the one phobic to the polymeric layer) can be controllably released. This study, therefore, provided a unique design perspective on developing nanoscale liquid separators and valves by utilizing nanoconfined grated polymer layers.

5.1 Future Work

This thesis has paved the framework for exploring the interactions of liquid drops, NPs, and responsive grafted and nanoconfined polymeric layers in an unprecedented fashion. There is a myriad of problems that this thesis will lead to in future.

For example, in the problems we have studied, the electrostatic interactions were mostly neglected. Therefore, in future studies it will be extremely interesting to probe the interactions of charged polymer layer (polyelectrolyte or PE layer) with an opposite charged NP. Similarly, it will be most remarkable to probe the development of *possible stable direct contacts* between identically charged NP and the PE layer, overcoming the large electrostatic repulsion, for the case when a liquid drop philic to the polymer drives the NP to close enough proximity of the monomers of the swelled polymer chains. This study will be along similar lines as the study on developing stable contacts between NP and a phobic polymer layer (see chapter 3); however, it will be of much greater significance given the dire needs to establish some form of attractive interactions between two similarly charged entities.

A different group of problems that will follow from the present thesis will involve a more explicit chemical consideration of the polymer systems, liquid drops, and NPs. For example, in the problems described in chapters 3 and 4, we have primarily considered Lennard Jones drops, NPs, and polymer chains. On the other hand, the same set of problems could be probed by considering explicit chemical nature of the polymer or PE chains (for example, poly-ethylene glycol chain or poly-acrylic acid chains), chemically explicit nature of the drops (water drops or certain other organic liquid drops), and chemically explicit nature of the NPs (e.g., silver or gold NPs, or NPs with distinct chemical functionalities, or Janus-like properties on two different hemispheres of the NPs). Such consideration will bring to the fore unprecedented molecular effects that have been hitherto overlooked in studies of drop and NP interactions with the polymer layer. For example, the interaction of the NPs with a layer of solvated poly-acrylic acid (or PAA) brushes will be dictated by the manner in which the NPs can break the solvation shell of around the PAA brushes

as well as the nature of the interactions of the NPs with the counterions that are strongly attached to the PAA brushes (in order to screen the PAA brush charges). Similarly, the spreading dynamics of a water drop (with the water modeled explicitly using SPC/E model, for example) on a non-wetted (and hence collapsed) PAA brush layer will depend on the ion content of the water drop. For example, drop wetting and imbibition dynamics and the associated brush swelling (a problem that has been studied for non-charged system in Chapter 2) will vary depending on whether the water drop is rich in monovalent or multivalent cations (or counterions needed for screening the charges of the PAA brushes), given the fact that the PAA brushes will react differently (in terms of swelling) to whether their charges are screened by monovalent or multivalent counterions.

Finally, as long-term future prospects of the findings of this thesis, it would be worthwhile to probe the different applications to which the thesis provides design ideas. For example, developing stable interactions between NP and phobic polymeric layer can be critical in designing universal polymer grafted surfaces for de-activation of a large number of different viruses regardless of their extent of philic/phobic interactions with the polymer layer. Similarly, the separation and valving effects (as outlined in chapter 4) can be better designed for actual nanoconfined liquids, enabling the *on-demand* dispensation of very little liquid volumes (femto-liters to pico-liters). Also, the progressive swelling of the nanoconfined polymer brushes (as elucidated in chapter 4) and the consequent entrapment of the phobic liquid (liquid that is phobic to the polymeric layer) in progressively narrower space within the nanochannel indicates to the localization of the phobic liquid to progressively stronger confinements. Such confinements are much stronger as compared to what can be achieved by simple geometry, and will therefore enable liquid localization and consequent

engineering activities (e.g., confinement driven stretching of a DNA molecule) in nanochannels of dimensions that are otherwise very difficult to achieve through actual nano-fabrication.

Appendix A

Some important supporting information related to chapter 2 is presented here.

A.1. MD Simulation Snapshots

The MD simulation snapshots showing the coupled dynamics of the polymeric liquid drop and the grafted polymer molecules for the grafting density of $\sigma_g=0.31/\sigma^2$ have been provided in Fig. A.1.

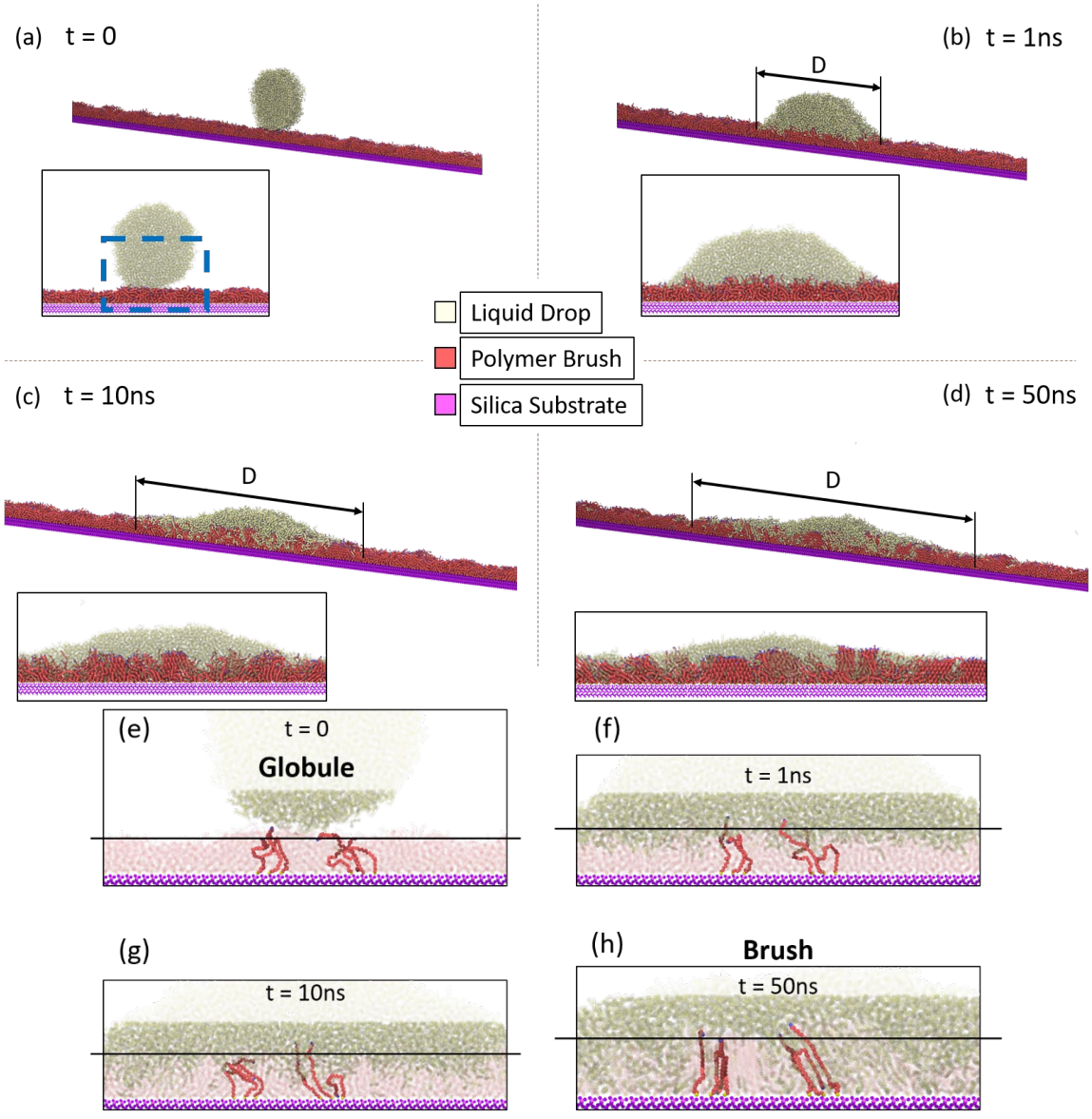

Figure A.1. (a-d) MD simulation snapshots showing the interaction of the polymeric liquid drop with the layer of grafted polymer molecules (grafting density $\sigma_g=0.31/\sigma^2$) at different time instants (identified on top of the snapshots). For these figures, the interaction is shown by depicting the entire length of the layer of the grafted polymer molecules. In the inset of these subfigures, we

highlight a smaller section of the layer of the grafted polymer molecules providing a more detailed view of the solvent-polymer-molecule interface. The simultaneous spreading and wicking of the liquid molecules (inside the layer of the grafted polymer molecules) become apparent from these snapshots. In subfigures (a-d), D represents the contact diameter. (e-g) Zoomed images showcasing the behavior of the liquid molecules and the grafted polymer molecules corresponding to region highlighted in (a). These snapshots show that as the liquid penetrates more and more into the polymer layer (the extent of this penetration is represented by noting the location of the liquid front with respect to the black line that provides the instantaneous average height of the grafted polymer molecules), the polymer molecules swell and stretch out to take the form of brushes (the fact that they attain brush-like configuration is established in Fig. 2.6 in the main chapter). For a clearer visualization, we do not show all the polymer molecules along a given length of the solid surface; rather we show only a selected few.

A.2. Calculation of the Contact Radius (r), Dynamic Contact Angle (θ), Average Time-dependent height of the Grafted Polymer Layer, and Wicking Fraction

We hereby provide the details for the calculation of the different quantities provided in the main paper. First, we calculate the contact radius (r) of the drop as it spreads. For that purpose, we first divide the system into two-dimensional bins of size 5Å × 5Å in the vertical plane and filter out bins with insignificant number of liquid molecules, based on their number density (less than 10% of the maximum number density), at every time instant. This is done so as to obtain the actual shape of the drop and to remove molecules that may have drifted away. Other bin sizes between 3Å-7Å were also tested and we obtain a contact radius variation of less than 2%. Also, the cutoff of 10% of the maximum number density was chosen, because there is a sharp fall in the number density within the bins beyond this cutoff. This implies that for the bins neighboring the drop surface, the number density falls sharply below the cutoff chosen here (10%), so that the adjacent bins have of the order of 1% of the maximum number density. Once this is done, we simply calculate the contact diameter by taking the difference of the minimum and maximum locations of the drop "three-phase" contact line in the x-direction, near the substrate. Of course, after sufficient time, the drop stops spreading and we obtain an equilibrium contact radius. Figure A.2 provides a schematic view of the binning procedure and a depiction of the estimated contact diameter.

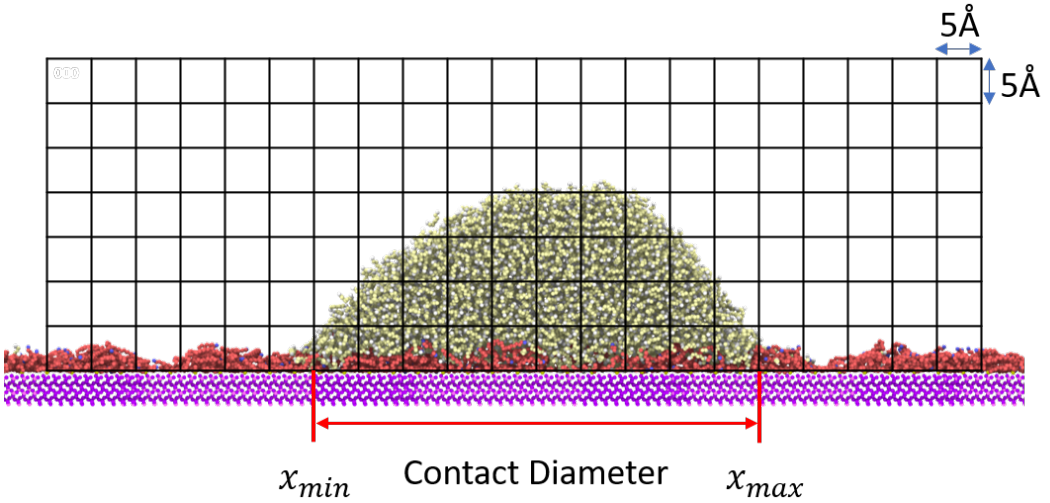

Figure A.2. Schematic of the binning procedure to calculate the contact radius of the drop. Each 2D bin has dimensions of 5Å × 5Å. The red arrow depicts the contact diameter, twice of the contact radius.

Following this, we evaluate the dynamic contact angle (θ) of the drop, based on a similar approach by Yuan[1]. We divide the liquid molecules of the drop into 3Å sized bins in the vertical direction (z), upto the maximum height of the drop and note the maximum (x_{max}) and minimum (x_{min}) x locations of the drop molecules in each of these bins. The drop is defined using the approach employed for the contact radius estimation. Two lines are then fit through each set of the x_{max} and x_{min} values from 5 adjacent bins nearest to the substrate, respectively, and the slope of these lines are evaluated to determine the contact angle. The slope of the line-fit through the x_{max} values would have a negative slope for acute contact angles; therefore, care is taken to compute the contact angle correctly for such a case. Since, there are two contact lines corresponding to the two sides of the 2D drop, we compute the average of the two as the contact angle of the drop at any instant. This process is repeated for the entire simulation time. Figure A.3 provides a schematic view of the binning procedure, the fitted lines through the lateral locations, and a depiction of the estimated contact angle.

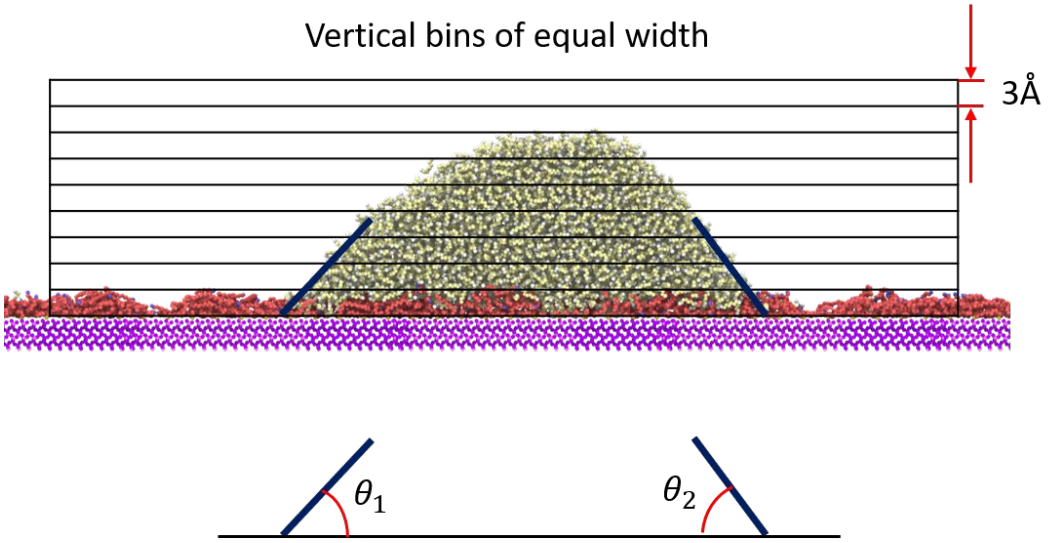

Figure A.3. Schematic of the binning procedure to calculate the contact angle of the drop, with bins of width 3Å. The blue lines depict the linear fit through the minimum and maximum lateral locations from the 5 bins nearest to the substrate. The contact angles for the two sides of the drop are represented by θ_1 and θ_2.

Next, we quantify the height of the grafted polymer layer as it stretches out in the presence of a favorable environment (octane). In Figure 4(a) in the main chapter, we have depicted a region that is x_{wk} =10-nm wide and localized below the drop and around the drop center: in that region, we quantify the dynamics of the polymer chains, as they stretch from a globule-like state to that of a brush, by quantifying the time-dependent average grafted polymer height in that region. We employ a trivial approach to compute this quantity: we average the individual heights of each of the polymer chains that are grafted in the chosen section at every time instant. We repeat this procedure for the whole simulation time.

Finally, we analyze the wicking behavior of the liquid molecules as they imbibe into the grafted polymer layer. To quantify this, we determine the number density of drop molecules that have imbibed into the substrate (any molecule that is within the grafted polymer layer, i.e., it has a vertical location less than the average polymer chain height, obtained from the previous result) at any time instant, within the region identified in Fig. 2.4(a) (a region that is x_{wk} =10-nm wide and localized below the drop and around the drop center). The result is normalized with respect to the maximum number density of imbibed liquid molecules (equilibrium number density inside the polymer layer) and is defined as the wicking fraction in this work.

Fig. A.4 shows the spreading of the droplet on the substrate grafted with the polymer chain (grafting density σ_g=0.31/σ^2) without the polymers being visible. This allows us to understand the drop spreading more clearly. Fig. A.4(c) depicts the equilibrium structure of the drop, and although the contact angle is quite small (only a few degrees), the drop configuration is still preserved (and we do not encounter a liquid film).

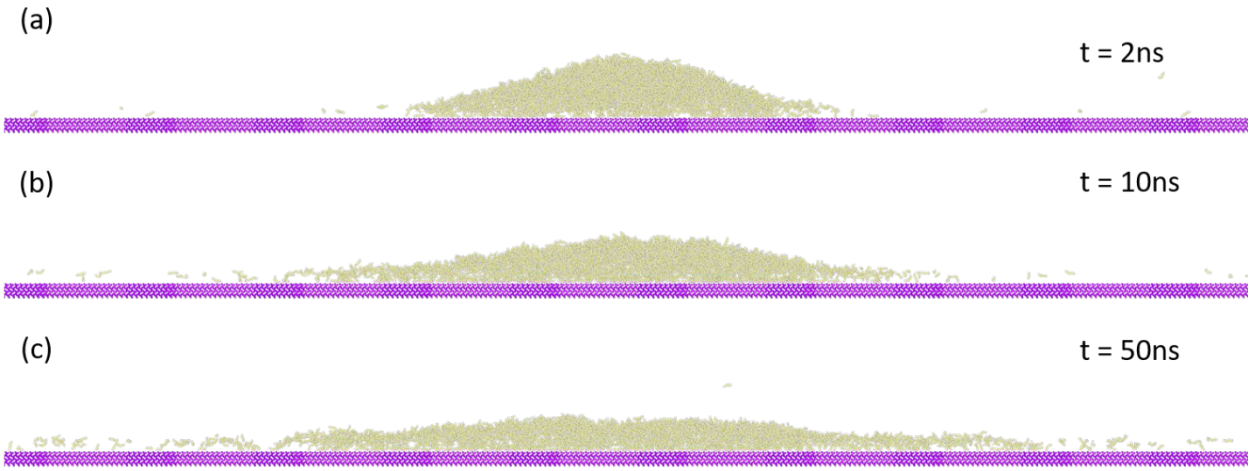

Figure A.4: MD simulation snapshots confirming the spreading dynamics and attainment of drop equilibrium on the substrate grafted with the polymer chain (grafting density σ_g = 0.085/σ^2) without the polymers being visible. The time value corresponding to each snapshot has been provided on the right-hand corner of that snapshot.

A.5. Autocorrelation Function for the Average Brush Height

In Fig. A.5, we provide the autocorrelation function for the average brush height for different grafting density values.

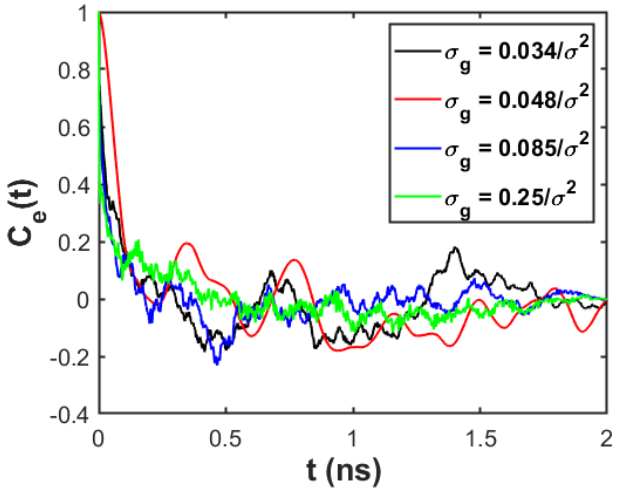

Figure A.5: Variation of the autocorrelation function for the average brush height for different grafting density values.

Appendix B

Some important supporting information related to chapter 3 is presented here.

B.1. Calculation of the Probability of Contact ($P_{contact}$), Average Number of Contacts, Relaxation Time Distribution (RTD) of Contacts, and Mean Square Displacement (MSD)

Here we provide the details for the calculation of various quantities provided in the main paper. The central result of the paper quantifies the stable direct contacts between the nanoparticle (NP) and the polymer molecules. As mentioned in the main paper, the monomers within the first solvation shell of the NP are considered to be in direct contact with the NP. We employ the following procedure to identify the monomers that are in direct contact with the NP. First, we isolate all the species that are within a shell of width 3σ around the NP. Then, for each NP-monomer pair within this shell, we check if there exists a 3rd intervening species (monomer or solvent molecule) within the sphere described by the line joining the NP surface and the monomer as diameter. If an intervening species exists, then the chosen NP-monomer pair are not in direct contact. If no intervening species exists, then the pair is said to be in direct contact. We represent this algorithm using a schematic (see Fig. B.1). From this, we can determine the existence of contact as a binary function: if the value of the function value is 0, it implies that no NP-polymer contact pair exists, while if the value of the function is 1, it implies that at least 1 pair of direct contact exists at any instant [please see the insets of Fig. 3.2 (a-c) in the main chapter]. This information can be subsequently used to trivially calculate the probability of the existence of at least 1 NP-polymer direct contact, i.e., $P_{contact}$ [please see Figs. 3.2(a-c) in main chapter]. We can also calculate the total number of direct contact pairs between the NP and polymer brush layer at

any instant and hence, the average number of contact pairs at any instant [please see Fig. 3.2(d-f) in main chapter]. Finally, we can analyze the lifetime of these direct contact pairs by calculating the relaxation time distribution (RTD) of contacts [defined as the fraction of contacts initiated at time t=0, that still exist at time t, see fig. 3.2(g-i)]. We obtain this by uniquely identifying each NP-monomer contact pair at every time instant and calculating the lifetime of each direct contact pair. The contact calculations are preformed using the data collected at regular time intervals of 0.1τ. A similar approach can be employed to quantify contact between the NP and solvent molecules. We can obtain the total number of direct contact pairs between the NP and solvent molecules ($\bar{N}$) at any time instant and the relaxation time distribution of such NP-solvent direct contacts using a similar algorithm as mentioned above. Finally, the Mean Squared Displacement (MSD) of different species is calculated by considering an ensemble average of the squared displacement over all particles of the corresponding species and over a long duration of time (ensuring equilibration is achieved).

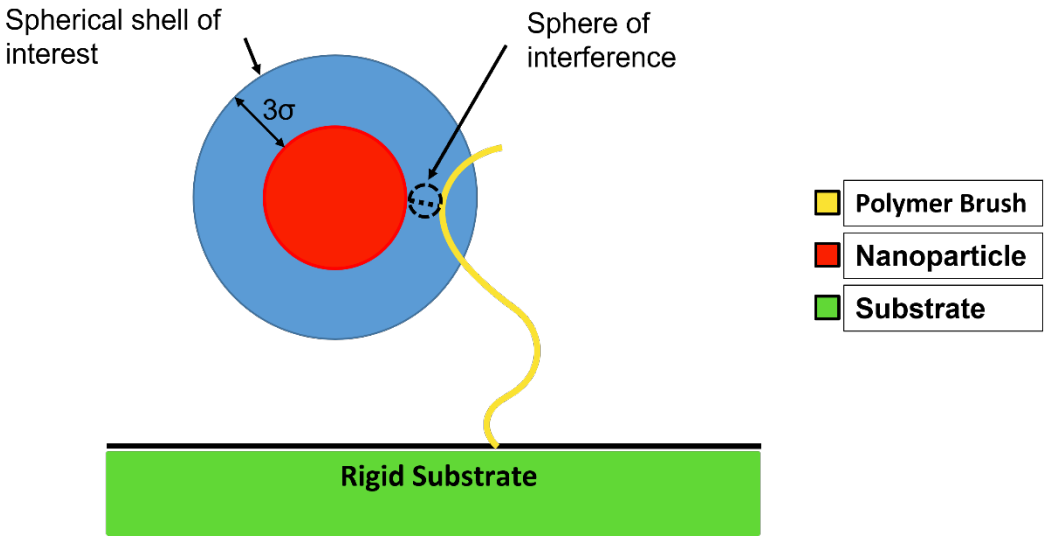

Figure B.1: Schematic representing the algorithm for determination of NP-monomer direct contact pairs. The sphere of interference (shown in this schematic) determines the existence of the contact: if an intervening species exists within this sphere, then the corresponding NP-monomer pair is not in direct contact, otherwise the NP-polymer contact is a direct contact.

B.2. Mean Square Displacement of Solvent Molecules

In fig. B.2, we provide the MSD of solvent molecules for the case of $\frac{\varepsilon_{PN}}{\varepsilon_{LP}} = 0.1$ and NP radius $= 2\sigma$. The MSDs of the solvent molecules remain identical over the full range of $\frac{\varepsilon_{PN}}{\varepsilon_{LP}}$ values and NP radii considered in this study.

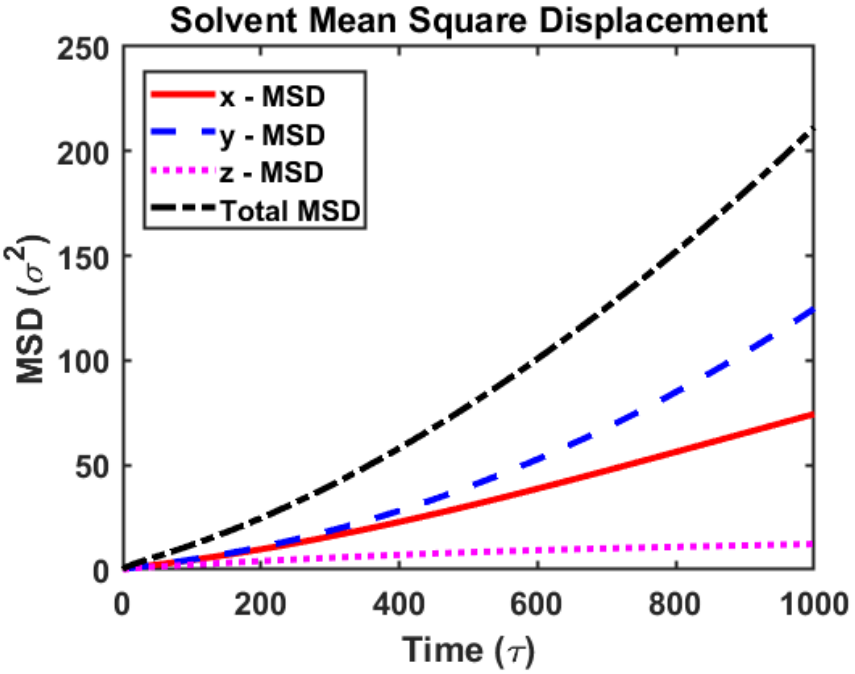

Figure B.2: Mean Squared Displacement (MSD) of the solvent molecules inside the polymer layer for the case corresponding to a NP of radius 2σ and $\frac{\varepsilon_{PN}}{\varepsilon_{LP}} = 0.1$.

Appendix C

Some important supporting information related to chapter 4 is presented here.

C.1. MD simulation snapshots corresponding to the remaining two nanochannel heights: h=44σ and h=48σ

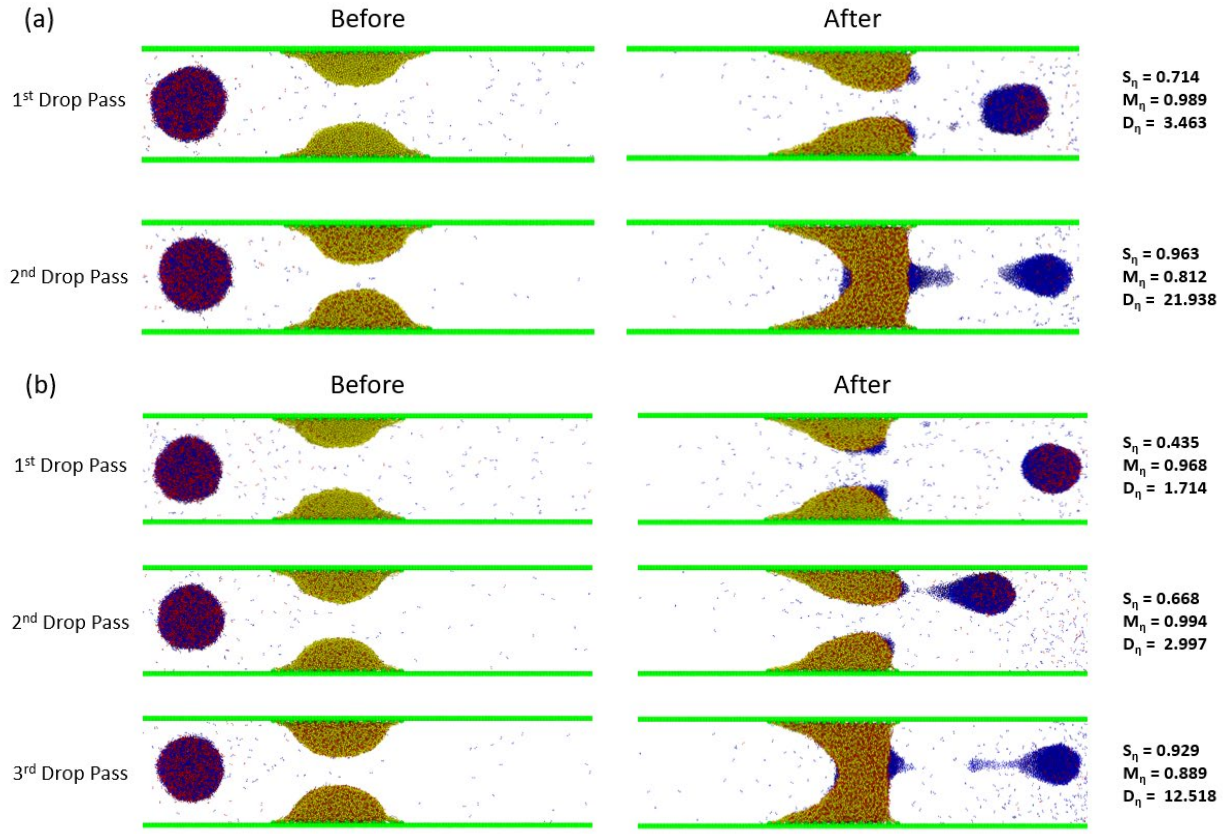

Figure C.1: MD simulation snapshots showing the passage of the liquid drop through the nanoconfined polymer grafted layers for the nanochannel of (a) height = 44σ and (b) height = 48σ. These nanochannels allows for (a) 2 and (b) 3 passages of the drop respectively (hence the *microphase separation process* and distillation-like behaviors correspondingly get repeated (a) 2 and (b) 3 times). On the margin of the figure showing each pass, we identify the corresponding parameters (discussed later) quantifying the separation (S_η, M_η) and distillation-like behavior (D_η).

C.2. Philic liquid (A) distribution at equilibrium and corresponding colormap of liquid densities for different passes for nanochannel height h=52σ

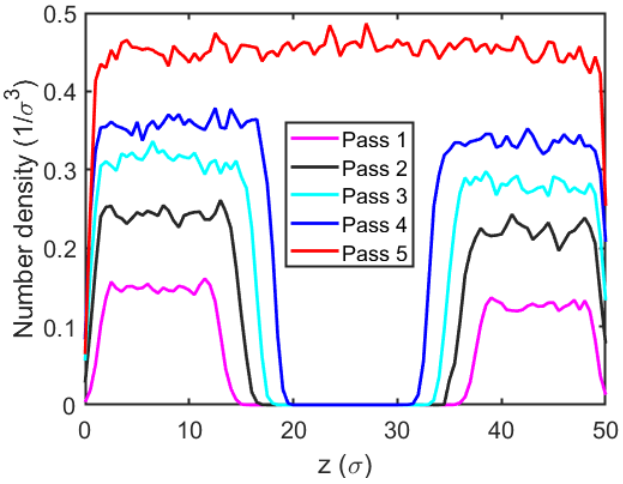

Figure C.2: Variation of the number density of philic liquid (A) molecules inside the polymer layer along the height of the nanochannel (h=52σ) after each drop passage at a midway plane dividing the polymer bilayer equally in the x-direction. The polymer layer swells in response to the imbibition by the philic liquid molecules as can be inferred by the shortening gap between the liquid density peaks. As the volume of liquid A inside the polymer bilayer increases so does the number density. After the last passage (pass 5), the polymer bilayer exhibits interpenetration.

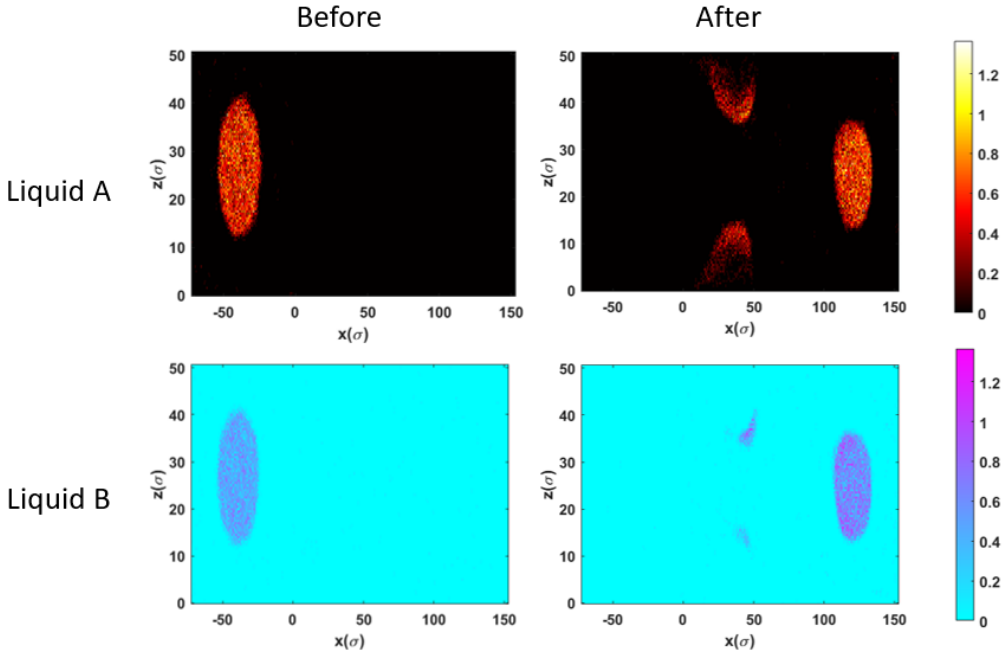

Figure C.3: Colormap depicting the liquid (A and B) densities before and after pass 1 for the case of nanochannel height, h=52σ. The density of liquid A inside the polymer layer increases after the passage of the drop, while a very tiny fraction of the liquid B molecules can be seen wetting the surface of the swollen polymer layers.

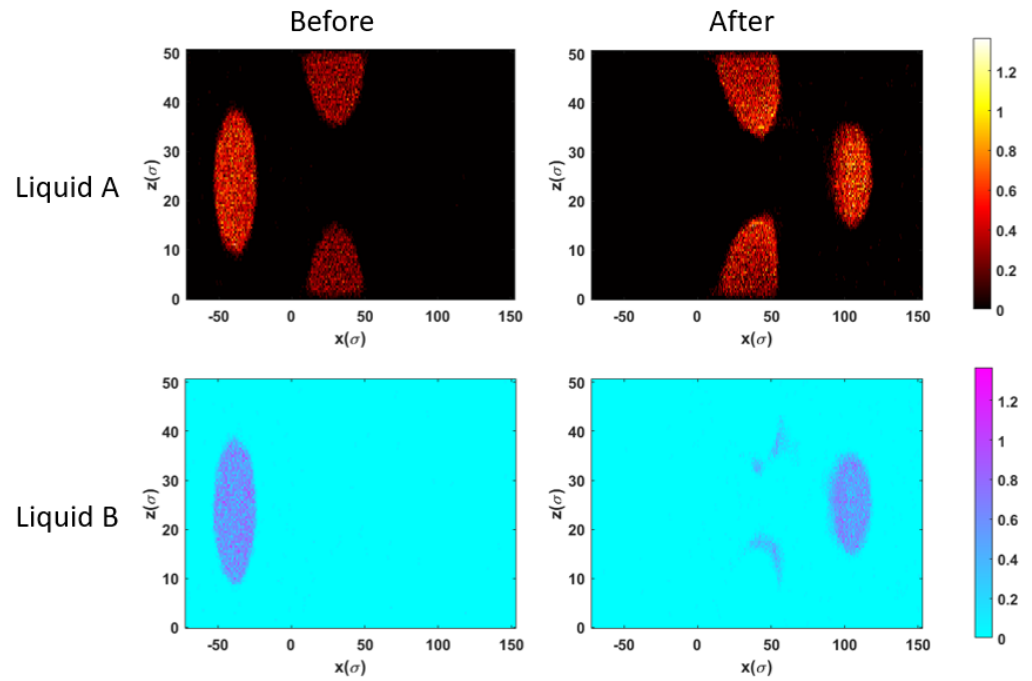

Figure C.4: Colormap depicting the liquid (A and B) densities before and after pass 3 for the case of nanochannel height, h=52σ.

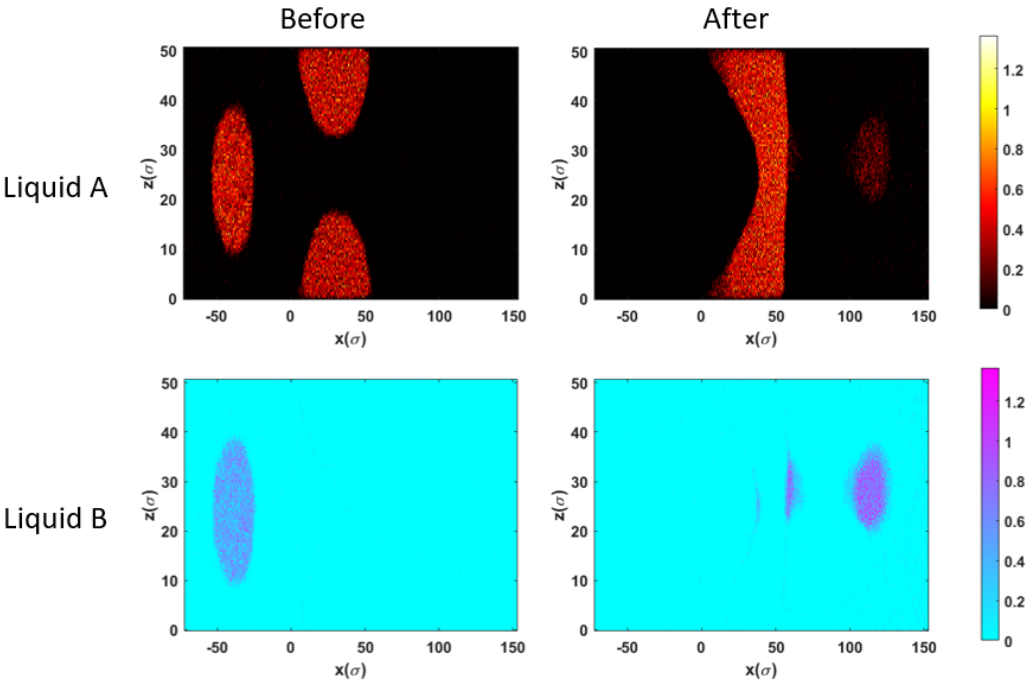

Figure C.5: Colormap depicting the liquid (A and B) densities before and after pass 5 for the case of nanochannel height, h=52σ.

References

1. Advincula, R. C., Brittain, W. J., Caster, K. C., & Rühe, J. (Eds.). (2006). *Polymer brushes: synthesis, characterization and applications*. John Wiley & sons.
2. Chen, T., Ferris, R., Zhang, J., Ducker, R., & Zauscher, S. (2010). Stimulus-responsive polymer brushes on surfaces: Transduction mechanisms and applications. *Progress in Polymer Science*, *35*(1-2), 94-112.
3. Stuart, M. A. C., Huck, W. T., Genzer, J., Müller, M., Ober, C., Stamm, M., ... & Minko, S. (2010). Emerging applications of stimuli-responsive polymer materials. *Nature materials*, *9*(2), 101-113.
4. Li, B., Yu, B., Ye, Q., & Zhou, F. (2015). Tapping the potential of polymer brushes through synthesis. *Accounts of Chemical Research*, *48*(2), 229-237.
5. Mizutani, A., Kikuchi, A., Yamato, M., Kanazawa, H., & Okano, T. (2008). Preparation of thermoresponsive polymer brush surfaces and their interaction with cells. *Biomaterials*, *29*(13), 2073-2081.
6. Wischerhoff, E., Uhlig, K., Lankenau, A., Börner, H. G., Laschewsky, A., Duschl, C., & Lutz, J. F. (2008). Controlled cell adhesion on PEG-based switchable surfaces. *Angewandte Chemie International Edition*, *47*(30), 5666-5668.
7. Azzaroni, O., Brown, A. A., & Huck, W. T. (2007). Tunable wettability by clicking counterions into polyelectrolyte brushes. *Advanced materials*, *19*(1), 151-154.
8. Bajpai, A. K., Shukla, S. K., Bhanu, S., & Kankane, S. (2008). Responsive polymers in controlled drug delivery. *Progress in Polymer Science*, *33*(11), 1088-1118.
9. Wei, Q., Cai, M., Zhou, F., & Liu, W. (2013). Dramatically tuning friction using responsive polyelectrolyte brushes. *Macromolecules*, *46*(23), 9368-9379.
10. Minko, S. (2006). Responsive polymer brushes. *Journal of Macromolecular Science, Part C: Polymer Reviews*.
11. Mansky, P., Liu, Y., Huang, E., Russell, T. P., & Hawker, C. (1997). Controlling polymer-surface interactions with random copolymer brushes. *Science*, *275*(5305), 1458-1460.
12. Minko, S., Müller, M., Motornov, M., Nitschke, M., Grundke, K., & Stamm, M. (2003). Two-level structured self-adaptive surfaces with reversibly tunable properties. *Journal of the American Chemical Society*, *125*(13), 3896-3900.

13. Luzinov, I., Klep, V., Minko, S., Iyer, K. S., Draper, J., & Zdyrko, B. (2004). Synthesis of Responsive Polymer Brushes via Macromolecular Anchoring Layer. *Polymeric Materials: Science & Engineering*, 90.
14. Motornov, M., Minko, S., Eichhorn, K. J., Nitschke, M., Simon, F., & Stamm, M. (2003). Reversible tuning of wetting behavior of polymer surface with responsive polymer brushes. *Langmuir*, *19*(19), 8077-8085.
15. Lemieux, M., Usov, D., Minko, S., Stamm, M., Shulha, H., & Tsukruk, V. V. (2003). Reorganization of binary polymer brushes: Reversible switching of surface microstructures and nanomechanical properties. *Macromolecules*, *36*(19), 7244-7255.
16. Ferhan, A. R., & Kim, D. H. (2016). Nanoparticle polymer composites on solid substrates for plasmonic sensing applications. *Nano Today*, *11*(4), 415-434.
17. Nie, G., Li, G., Wang, L., & Zhang, X. (2016). Nanocomposites of polymer brush and inorganic nanoparticles: preparation, characterization and application. *Polymer Chemistry*, *7*(4), 753-769.
18. Christau, S., Genzer, J., & von Klitzing, R. (2015). Polymer brush/metal nanoparticle hybrids for optical sensor applications: from self-assembly to tailored functions and nanoengineering. *Zeitschrift für Physikalische Chemie*, *229*(7-8), 1089-1117.
19. Müllner, M. (2016). Molecular polymer brushes in nanomedicine. *Macromolecular Chemistry and Physics*, *217*(20), 2209-2222.
20. Tokarev, I., & Minko, S. (2012). Tunable plasmonic nanostructures from noble metal nanoparticles and stimuli-responsive polymers. *Soft Matter*, *8*(22), 5980-5987.
21. Diamanti, S., Arifuzzaman, S., Genzer, J., & Vaia, R. A. (2009). Tuning gold nanoparticle− poly (2-hydroxyethyl methacrylate) brush interactions: From reversible swelling to capture and release. *Acs Nano*, *3*(4), 807-818.
22. Ferhan, A. R., & Kim, D. H. (2012). In-stacking: a strategy for 3D nanoparticle assembly in densely-grafted polymer brushes. *Journal of Materials Chemistry*, *22*(4), 1274-1277.
23. Liu, Z., Pappacena, K., Cerise, J., Kim, J., Durning, C. J., O'Shaughness, B., & Levicky, R. (2002). Organization of nanoparticles on soft polymer surfaces. *Nano Letters*, *2*(3), 219-224.

24. Onses, M. S., Liu, C. C., Thode, C. J., & Nealey, P. F. (2012). Highly selective immobilization of au nanoparticles onto isolated and dense nanopatterns of poly (2-vinyl pyridine) brushes down to single-particle resolution. *Langmuir*, *28*(18), 7299-7307.
25. Onses, M. S., & Nealey, P. F. (2013). Tunable assembly of gold nanoparticles on nanopatterned poly (ethylene glycol) brushes. *Small*, *9*(24), 4168-4174.
26. Steinbach, A., Paust, T., Pluntke, M., Marti, O., & Volkmer, D. (2013). Selective adsorption of functionalized nanoparticles to patterned polymer brush surfaces and its probing with an optical trap. *ChemPhysChem*, *14*(15), 3523-3531.
27. Oren, R., Liang, Z., Barnard, J. S., Warren, S. C., Wiesner, U., & Huck, W. T. (2009). Organization of nanoparticles in polymer brushes. *Journal of the American Chemical Society*, *131*(5), 1670-1671.
28. Bhat, R. R., Genzer, J., Chaney, B. N., Sugg, H. W., & Liebmann-Vinson, A. (2003). Controlling the assembly of nanoparticles using surface grafted molecular and macromolecular gradients. *Nanotechnology*, *14*(10), 1145.
29. Nguyen, T. D., Liu, Y., Saha, S., Leung, K. C. F., Stoddart, J. F., & Zink, J. I. (2007). Design and optimization of molecular nanovalves based on redox-switchable bistable rotaxanes. *Journal of the American Chemical Society*, *129*(3), 626-634.
30. Croissant, J., & Zink, J. I. (2012). Nanovalve-controlled cargo release activated by plasmonic heating. *Journal of the American Chemical Society*, *134*(18), 7628-7631.
31. Li, Z., Song, N., & Yang, Y. W. (2019). Stimuli-responsive drug-delivery systems based on supramolecular nanovalves. *Matter*, *1*(2), 345-368.
32. Hwang, A. A., Lu, J., Tamanoi, F., & Zink, J. I. (2015). Functional nanovalves on protein-coated nanoparticles for in vitro and in vivo controlled drug delivery. *Small*, *11*(3), 319-328.
33. Tarn, D., Ferris, D. P., Barnes, J. C., Ambrogio, M. W., Stoddart, J. F., & Zink, J. I. (2014). A reversible light-operated nanovalve on mesoporous silica nanoparticles. *Nanoscale*, *6*(6), 3335-3343.
34. Dong, J., Xue, M., & Zink, J. I. (2013). Functioning of nanovalves on polymer coated mesoporous silica Nanoparticles. *Nanoscale*, *5*(21), 10300-10306.

35. Wang, Q., Yu, X., Zhao, Y., Wang, Y., Chen, K., Liu, Y., ... & Sun, Y. (2022). Friction-induced supramolecular nanovalves for the potential treatment of osteoarthritis. *Materials Today Chemistry*, *24*, 100876.
36. Chen, T., & Fu, J. (2012). pH-responsive nanovalves based on hollow mesoporous silica spheres for controlled release of corrosion inhibitor. *Nanotechnology*, *23*(23), 235605.
37. Meng, H., Xue, M., Xia, T., Zhao, Y. L., Tamanoi, F., Stoddart, J. F., ... & Nel, A. E. (2010). Autonomous in vitro anticancer drug release from mesoporous silica nanoparticles by pH-sensitive nanovalves. *Journal of the American Chemical Society*, *132*(36), 12690-12697.
38. Özalp, V. C., & Schäfer, T. (2011). Aptamer-based switchable nanovalves for stimuli-responsive drug delivery. *Chemistry–A European Journal*, *17*(36), 9893-9896.
39. Eberle, P., Höller, C., Müller, P., Suomalainen, M., Greber, U. F., Eghlidi, H., & Poulikakos, D. (2018). Single entity resolution valving of nanoscopic species in liquids. *Nature Nanotechnology*, *13*(7), 578-582.
40. Yazbeck, R., Xu, Y., Porter, T., & Duan, C. (2022). Nanoparticle-blockage-enabled rapid and reversible nanopore gating with tunable memory. *Proceedings of the National Academy of Sciences*, *119*(27), e2200845119.
41. Xu, Y., Shinomiya, M., & Harada, A. (2016). Soft Matter-Regulated Active Nanovalves Locally Self-Assembled in Femtoliter Nanofluidic Channels. *Advanced Materials*, *28*(11), 2209-2216.
42. Chu, K. C., Tsao, H. K., & Sheng, Y. J. (2020). Pressure-gated capillary nanovalves based on liquid nanofilms. *Journal of colloid and interface science*, *560*, 485-491.
43. Bhat, R. R., Tomlinson, M. R., & Genzer, J. (2004). Assembly of Nanoparticles using Surface-Grafted Orthogonal Polymer Gradients. *Macromolecular rapid communications*, *25*(1), 270-274.
44. Bhat, R. R., & Genzer, J. (2006). Combinatorial study of nanoparticle dispersion in surface-grafted macromolecular gradients. *Applied surface science*, *252*(7), 2549-2554.
45. Kesal, D., Christau, S., Krause, P., Möller, T., & Von Klitzing, R. (2016). Uptake of pH-sensitive gold nanoparticles in strong polyelectrolyte brushes. *Polymers*, *8*(4), 134.
46. Rothstein, J. P. Slip on Superhydrophobic Surfaces. Annu. Rev. Fluid. Mech. 2010, 42, 89-109.
47. Quéré, D. Rough Ideas on Wetting. Physica A 2002, 313, 32-46.

48. Quéré, D. Wetting and Roughness. Annu. Rev. Mater. Res. 2008, 38, 71-99.
49. Bormashenko, E. Progress in Understanding Wetting Transitions on Rough Surfaces. Adv. Colloid Interface Sci. 2015, 222, 92-103.
50. An, H.; Liu, G.; Craig, V. S. J. Wetting of Nanophases: Nanobubbles, Nanodroplets and Micropancakes on Hydrophobic Surfaces. Adv. Colloid Interface Sci. 2015, 222, 9-17.
51. Zhang, P.; Lv, F. Y. A Review of the Recent Advances in Superhydrophobic Surfaces and the Emerging Energy-related Applications. Energy 2015, 82, 1068-1087.
52. Nosonovsky, M.; Bhushan, B. Superhydrophobic Surfaces and Emerging Applications: Non-adhesion, Energy, Green Engineering. Curr. Opin. Colloid Interface Sci. 2009, 14, 270-280.
53. Zhang, S.; Huang, J.; Chen, Z.; Yang, S.; Lai, Y. Liquid Mobility on Superwettable Surfaces for Applications in Energy and the Environment. J. Mater. Chem. A 2019, 7, 38-63.
54. Faide, E. J.; Yohe, S. T.; Colson. Y. L.; Grinstaff, M. W. Superhydrophobic Materials for Biomedical Applications. Biomaterials 2016, 104, 87-103.
55. Chenab, K. K.; Sohrabi, B.; Rahmanzadeh, A. Superhydrophobicity: Advanced Biological and Biomedical Applications. Biomater. Sci. 2019, 7, 3110-3137.
56. Dietz, C.; Rykaczewski, K.; Fedorov, A. G.; Joshi, Y. Visualization of Droplet Departure on a Superhydrophobic Surface and Implications to Heat Transfer Enhancement during Dropwise Condensation. Appl. Phys. Lett. 2010, 97, 033104.
57. Miljkovic, N.; Enright, R.; Wang, E. N. Effect of Droplet Morphology on Growth Dynamics and Heat Transfer during Condensation on Superhydrophobic Nanostructured Surfaces. ACS Nano 2012, 6, 1776-1785.
58. Wen, R.; Xu, S.; Ma, X.; Lee, Y-C.; Yang, R. Three-Dimensional Superhydrophobic Nanowire Networks for Enhancing Condensation Heat Transfer. Joule 2018, 2, 269-279.
59. Han, K.; Park, T. Y.; Yong, K.; Cha, H. J. Combinational Biomimicking of Lotus Leaf, Mussel, and Sandcastle Worm for Robust Superhydrophobic Surfaces with Biomedical Multifunctionality: Antithrombotic, Antibiofouling, and Tissue Closure Capabilities. ACS Appl. Mater. Interfaces 2019, 11, 9777-9785.
60. Zhang, P.; Lin, L.; Zang, D.; Guo, X.; Liu, M. Designing Bioinspired Anti-Biofouling Surfaces based on a Superwettability Strategy. Small 2017, 13, 1503334.

61. Wang, T.; Huang, L.; Liu, Y.; Li, X.; Liu, C.; Handschuh-Wang, S.; Xu, Y.; Zhao, Y.; Tang, Y. Robust Biomimetic Hierarchical Diamond Architecture with a Self-Cleaning, Antibacterial, and Antibiofouling Surface. ACS Appl. Mater. Interfaces 2020, 12, 24432-24441.
62. Xiang, T.; Han, Y.; Guo, Z.; Wang, R.; Zheng, S.; Li, S.; Li, C.; Dai, X.; Fabrication of Inherent Anticorrosion Superhydrophobic Surfaces on Metals. ACS Sustainable Chem. Eng. 2018, 6, 5598-5606.
63. de Leon, A. C. C.; Pernites, R. B.; Advincula, R. C. Superhydrophobic Colloidally Textured Polythiophene Film as Superior Anticorrosion Coating. ACS Appl. Mater. Interfaces 2012, 4, 3169-3176.
64. Li, Q.; Liu, H.; Zhang, S.; Zhang, D.; Liu, X.; He, Y.; Mi, L.; Zhang, J.; Liu, C.; Shen, C.; Guo, Z. Superhydrophobic Electrically Conductive Paper for Ultrasensitive Strain Sensor with Excellent Anticorrosion and Self-Cleaning Property. ACS Appl. Mater. Interfaces 2019, 11, 21904-21914.
65. Tang, Y.; Zhang, Q.; Zhan, Z.; Chen, F. Superhydrophobic and anti-icing Properties at Overcooled Temperature of a Fluorinated Hybrid Surface Prepared via a Sol–gel Process. Soft Matt. 2015, 11, 4540-4550.
66. Wang, Y.; Xue, J.; Wang, Q.; Chen, Q.; Ding, J. Verification of Icephobic/Anti-icing Properties of a Superhydrophobic Surface. ACS Appl. Mater. Interfaces 2013, 5, 3370-3381.
67. Wang, L.; Gong, Q.; Zhan, S.; Jiang, L.; Zheng, Y. Robust Anti-Icing Performance of a Flexible Superhydrophobic Surface. Adv. Mater. 2016, 28, 7729-7735.
68. Zhou, X.; Zhang, Z.; Xu, X.; Guo, F.; Zhu, X.; Men, X.; Ge, B. Robust and Durable Superhydrophobic Cotton Fabrics for Oil/Water Separation. ACS Appl. Mater. Interfaces 2013, 5, 7208-7214.
69. Zhou, C.; Chen, Z.; Yang, H.; Hou, K.; Zeng, X.; Zheng, Y.; Cheng, J. Nature-Inspired Strategy toward Superhydrophobic Fabrics for Versatile Oil/Water Separation. ACS Appl. Mater. Interfaces 2017, 9, 9184-9194.
70. Winkels, K. G.; Weijs, J. H.; Eddi, E.; Snoeijer, J. H. Initial Spreading of Low-viscosity Drops on Partially Wetting Surfaces. Phys. Rev. E 2012, 85, 055301(R).

71. Zhao, L.; Cheng, J. Analyzing the Molecular Kinetics of Water Spreading on Hydrophobic Surfaces via Molecular Dynamics Simulation. Sci. Rep. 2017, 7, 10880.
72. Ji, D.; Liu, G.; Zhang, X.; Zhang, C.; Yuan, S. Molecular Dynamics Study on the Adsorption of Heavy Oil Drops on a Silica Surface with Different Hydrophobicity. Energy Fuels 2020, 34, 7019-7028.
73. Li, H.; Yan, T.; Fichthorn, K. A.; Yu, S. Dynamic Contact Angles and Mechanisms of Motion of Water Droplets Moving on Nanopillared Superhydrophobic Surfaces: A Molecular Dynamics Simulation Study. Langmuir 2018, 34, 9917-9926.
74. Ma, M.;Tocci, G.; Michaelides, A.; Aeppli, G. Fast Diffusion of Water Nanodroplets on Graphene. Nature Mater. 2016, 15, 66-71.
75. Guo, L.; Tang, G. H.; Kumar, S. Dynamic Wettability on the Lubricant-Impregnated Surface: From Nucleation to Growth and Coalescence. ACS Appl. Mater. Interface 2020, 12, 26555-26565.
76. Guo, L.; Tang, G. H.; Kumar, S. Droplet Morphology and Mobility on Lubricant-Impregnated Surfaces: A Molecular Dynamics Study. Langmuir 2019, 35, 16377-16387.
77. Papadopoulou, E.; Megaridis, C. M.; Walther, J. M.; Koumoutsakos, P. Ultrafast Propulsion of Water Nanodroplets on Patterned Graphene. ACS Nano 2019, 13, 5465-5472.
78. Wang, Y.; Ahuja, K.; Sinha, S.; Desai, P. R.; Das, S. Water-Holey-Graphene Interactions: Route to Highly Enhanced Water-Accessible Graphene Surface Area. ACS Appl. Nano Mater. 2018, 1, 5907-5918.
79. Wang, Y. Sinha, S.; Ahuja, K.; Desai, P. R.; Dai, J.; Hu, L.; Das, S. Dynamics of a Water Nanodrop through a Holey Graphene Matrix: Role of Surface Functionalization, Capillarity, and Applied Forcing. J. Phys. Chem. C 2018, 122, 12243-12250.
80. Andrews, J. E.; Wang, Y.; Sinha, S.; Chung, P. W.; Das, S. Roughness-Induced Chemical Heterogeneity Leads to Large Hydrophobicity in Wetting-Translucent Nanostructures. J. Phys. Chem. C 2017, 121, 10010-10017.
81. Wang, Y.; Andrews, J. E.; Hu, L.; Das, S. Drop Spreading on a Superhydrophobic Surface: Pinned Contact Line and Bending Liquid Surface. Phys. Chem. Chem. Phys. 2017, 19, 14442-14452.

82. Wang, Y.; Sinha, S.; Hu, L.; Das, S. Interaction between a Water Drop and Holey Graphene: Retarded Imbibition and Generation of Novel Water–graphene Wetting States. Phys. Chem. Chem. Phys. 2017, 19, 27421-27434.
83. Andrews, J. E.; Sinha, S.; Chung, P. W.; Das, S. Wetting Dynamics of a Water Nanodrop on Graphene. Phys. Chem. Chem. Phys. 2016, 18, 23482-23493.
84. Wagemann, E.; Wang, Y.; Das, S.; Mitra, S. K. On the Wetting Translucency of Hexagonal Boron Nitride. Phys. Chem. Chem. Phys. 2020, 22, 7710-7718.
85. Wagemann, E.; Wang, Y.; Das, S.; Mitra, S. K. Wettability of Nanostructured Hexagonal Boron Nitride Surfaces: Molecular Dynamics Insights on the Effect of Wetting Anisotropy. Phys. Chem. Chem. Phys. 2020, 22, 2488-2497.
86. Williams, C.; Brochard, F.; Frisch, H. L. Polymer Collapse. Annu. Rev. Phys. Chem. 1981, 32, 433-451.
87. Wang, X.; Qiu, X.; Wu, C. Comparison of the Coil-to-Globule and the Globule-to-Coil Transitions of a Single Poly(N-isopropylacrylamide) Homopolymer Chain in Water. Macromolecules 1998, 31, 2972-2978.
88. Zhang, G.; Wu, C. The Water/Methanol Complexation Induced Reentrant Coil-to-Globule-to-Coil Transition of Individual Homopolymer Chains in Extremely Dilute Solution. J. Am. Chem. Soc. 2001, 123, 1376–1380.
89. Wu, C.; Wang, X. Globule-to-Coil Transition of a Single Homopolymer Chain in Solution. Phys. Rev. Lett. 1998, 80, 4092-4094.
90. Léonforte, F.; Müller, M. Statics of Polymer Droplets on Deformable Surfaces. J. Chem. Phys. 2011, 135, 214703.
91. Cao, Z.; Dobrynin, A. Polymeric Droplets on Soft Surfaces: From Neumann's Triangle to Young's Law. Macromolecules 2015, 48, 443-451.
92. Speyer, K.; Pastorino, C. Droplet Transport in a Nanochannel Coated by Hydrophobic Semiflexible Polymer Brushes: The Effect of Chain Stiffness. Langmuir 2017, 33, 10753-10763.
93. Desai, P. R.; Wang, Y.; Sachar, H. S.; Jing, H.; Sinha, S.; Das, S. Supersolvophobic Soft Wetting: Nanoscale Elastocapillarity, Adhesion, and Retention of a Drop Behaving as a Nanoparticle. Matter 2019, 1, 1262-1273.

94. Mensink, L. I. S.; Snoeijer, J. H.; de Beer, S. Wetting of Polymer Brushes by Polymeric Nanodroplets. Macromolecules 2019, 52, 2015-2020.
95. Liu, X.; Ye, Q.; Song, X.; Zhu, Y.; Cao, X.; Liang, Y.; Zhou, F. Responsive Wetting Transition on Superhydrophobic Surfaces with Sparsely Grafted Polymer Brushes. Soft Matt. 2011, 7, 515-523.
96. Dunderdale, G. J.; England, M. W.; Urata, C.; Hozumi, A. Polymer Brush Surfaces Showing Superhydrophobicity and Air-Bubble Repellency in a Variety of Organic Liquids. ACS Appl. Mater. Interfaces 2015, 7, 12220-12229.
97. Karpitschka, S.; Das, S.; van Gorcum, M.; Perrin, H.; Andreotti, B.; Snoeijer, J. H. Droplets Move over Viscoelastic Substrates by Surfing a Ridge. Nature Comm. 2015, 6, 7891.
98. Karpitschka, S.; Pandey, A.; Lubbers, L. A.; Weijs, J. H.; Botto, L.; Das, S.; Andreotti, B.; Snoeijer, J. H. Proc. Natl. Acad. Sci. USA 2016, 113, 7403-7407.
99. Villegas, M.; Zhang, Y.; Jarad, N. A.; Soleymani, L.; Didar, T. F. Liquid-Infused Surfaces: A Review of Theory, Design, and Applications. ACS Nano 2019, 13, 8517-8536.
100. Peppou-Chapman, S.; Hong, J. K.; Waterhouse, A.; Neto, C. Life and Death of Liquid-infused Surfaces: A Review on the Choice, Analysis and Fate of the Infused Liquid Layer. Chem. Soc. Rev. 2020, 49, 3688-3715.
101. Howell, C.; Grinthal, A.; Sunny, S.; Aizenberg, M.; Aizenberg, J. Designing Liquid-Infused Surfaces for Medical Applications: A Review. Adv. Mater. 2018, 30, 1802724.
102. Sett, S.; Yan, X.; Barac, G.; Bolton, L. W.; Miljkovic, N. Lubricant-Infused Surfaces for Low-Surface-Tension Fluids: Promise versus Reality. ACS Appl. Mater. Interface 2017, 9, 36400-36408.
103. Ashrafi, Z.; Lucia, L.; Krause, W. Nature-Inspired Liquid Infused Systems for Superwettable Surface Energies. ACS Appl. Mater. Interface 2019, 11, 21275–21293.
104. Qiu, R.; Zhang, Q.; Wang, P.; Jiang, L.; Hou, J.; Guo, W.; Zhang, H. Fabrication of Slippery Liquid-Infused Porous Surface Based on Carbon Fiber with Enhanced Corrosion Inhibition Property. Colloids Surf. A 2014, 453, 132-141.
105. Osborne, M.; Aryasomayajula, A.; Shakeri, A.; Selvaganapathy, P. R.; Didar, T. F. Suppression of Biofouling on a Permeable Membrane for Dissolved Oxygen Sensing Using a Lubricant-Infused Coating. ACS Sensors 2019, 4, 687-693.

106. Kim, P.; Wong, T.-S.; Alvarenga, J.; Kreder, M. J.; Adorno-Martinez, W. E.; Aizenberg, J. Liquid-Infused Nanostructured Surfaces with Extreme Anti-Ice and Anti-Frost Performance. ACS Nano 2012, 6, 6569−6577.
107. Ferreira, P. G., Ajdari, A., & Leibler, L. (1998). Scaling law for entropic effects at interfaces between grafted layers and polymer melts. Macromolecules, 31(12), 3994-4003.
108. Maas, J. H., Fleer, G. J., Leermakers, F. A. M., & Cohen Stuart, M. A. (2002). Wetting of a polymer brush by a chemically identical polymer melt: Phase diagram and film stability. Langmuir, 18(23), 8871-8880.
109. Plimpton, S. Fast Parallel Algorithms for Short-range Molecular Dynamics. J. Comput. Phys. 1995, 117, 1-19.
110. Ingram, B. T. Wetting of Silica by n-alkanes. J. Chem. Soc. Farad. Trans. 1 1974, 70, 868-876.
111. Jorgensen, W. L.; Madura, J. D.; Swenson, C. J. Optimized Intermolecular Potential Functions for Liquid Hydrocarbons. J. Am. Chem. Soc. 1984, 106, 6638-6646.
112. Taylor, R. S., & Shields, R. L. (2003). Molecular-dynamics simulations of the ethanol liquid–vapor interface. The Journal of chemical physics, 119(23), 12569-12576.
113. da Silva, G. C., Silva, G. M., Tavares, F. W., Fleming, F. P., & Horta, B. A. (2020). Are all-atom any better than united-atom force fields for the description of liquid properties of alkanes?. Journal of Molecular Modeling, 26(11), 1-17.
114. Bai, P.; Tsapatsis, M.; Siepmann, J. I. TraPPE-zeo: Transferable Potentials for Phase Equilibria Force Field for All-silica Zeolites. J. Phys. Chem. C 2013, 117, 24375-24387.
115. Nosé, S. A Unified Formulation of the Constant Temperature Molecular Dynamics Methods. J. Chem. Phys. 1984, 81, 511-519.
116. Hoover, W. G. Canonical Dynamics: Equilibrium Phase-Space Distributions. Phys. Rev. A 1985, 31, 1695-1697.
117. Murat, M.; Grest, G. S. Structure of a Grafted Polymer Brush: A Molecular Dynamics Simulation. Macromolecules 1989, 22, 4054-4059.
118. Stukowski, A. Visualization and Analysis of Atomistic Simulation Data with OVITO–the Open Visualization Tool. Model. Simul. Mater. Sci. Eng. 2010, 18, 015012.
119. Milner, S. T. Polymer Brushes. Science 1991, 251, 905-914.

120. Eddi, A.; Winkels, K. G.; Snoeijer, J. H. Short Time Dynamics of Viscous Drop Spreading. Phys. Fluid. 2013, 25, 013102.
121. Tanner, L. H. The Spreading of Silicone Oil Drops on Horizontal Surfaces. J. Phys. D 1979, 12, 1473-1484.
122. Bonn, D.; Eggers, J.; Indekeu, J.; Meunier, J.; Rolley, E. Wetting and Spreading. Rev. Mod. Phys. 2009, 81, 739-804.
123. Carré, A.; Gastel, J-C.; Shanahan, M. E. R. Viscoelastic Effects in the Spreading of Liquids. Nature 1996, 379, 432-434.
124. Shanahan, M. E. R.; Carré, A. Viscoelastic Dissipation in Wetting and Adhesion Phenomena. Langmuir 1995, 11, 1396-1402.
125. Fredrickson, G. H.; Ajdari, A.; Leibler, L.; Carton, J-P. Surface Modes and Deformation Energy of Molten Polymer Brush. Macromolecules 1992, 25, 2882-2889.
126. Badv, M.; Jaffer, I. H.; Weitz, J. I.; Didar, T. F. An Omniphobic Lubricant-Infused Coating Produced by Chemical Vapor Deposition of Hydrophobic Organosilanes Attenuates Clotting on Catheter Surfaces. Sci. Rep. 2017, 7, 11639.
127. Brown, A. A., Azzaroni, O., & Huck, W. T. (2009). Photoresponsive polymer brushes for hydrophilic patterning. Langmuir, 25(3), 1744-1749.
128. Azzaroni, O., Brown, A. A., & Huck, W. T. (2007). Tunable wettability by clicking counterions into polyelectrolyte brushes. Advanced materials, 19(1), 151-154.
129. Lubbers, L. A., Weijs, J. H., Botto, L., Das, S., Andreotti, B., & Snoeijer, J. H. (2014). Drops on soft solids: free energy and double transition of contact angles. Journal of fluid mechanics, 747.
130. Marchand, A., Das, S., Snoeijer, J. H., & Andreotti, B. (2012). Contact angles on a soft solid: From Young's law to Neumann's law. Physical review letters, 109(23), 236101.
131. Jing, H., Sinha, S., & Das, S. (2017). Elasto-electro-capillarity: drop equilibrium on a charged, elastic solid. Soft matter, 13(3), 554-566.
132. Pastorino, C., Binder, K., Kreer, T., & Müller, M. (2006). Static and dynamic properties of the interface between a polymer brush and a melt of identical chains. The Journal of chemical physics, 124(6), 064902.

133. de Beer, S., Kutnyanszky, E., Schön, P. M., Vancso, G. J., & Müser, M. H. (2014). Solvent-induced immiscibility of polymer brushes eliminates dissipation channels. Nature communications, 5(1), 1-6.

134. Zhao, M., Lequeux, F., Narita, T., Roché, M., Limat, L., & Dervaux, J. (2018). Growth and relaxation of a ridge on a soft poroelastic substrate. Soft matter, 14(1), 61-72.

135. Xu, Q., Wilen, L. A., Jensen, K. E., Style, R. W., & Dufresne, E. R. (2020). Viscoelastic and poroelastic relaxations of soft solid surfaces. arXiv preprint arXiv:2006.09767.

136. Inutsuka, M., Tanoue, H., Yamada, N. L., Ito, K., & Yokoyama, H. (2017). Dynamic contact angle on a reconstructive polymer surface by segregation. RSC advances, 7(28), 17202-17207.

137. Cohen Stuart, M. A., De Vos, W. M., & Leermakers, F. A. M. (2006). Why surfaces modified by flexible polymers often have a finite contact angle for good solvents. Langmuir, 22(4), 1722-1728.

138. Thiele, U., & Hartmann, S. (2020). Gradient dynamics model for drops spreading on polymer brushes. The European Physical Journal Special Topics, 229(10), 1819-1832.

139. Dai, L.; He, P.; Li, S. Functionalized Surfaces Based on Polymers and Carbon Nanotubes for Some Biomedical and Optoelectronic Applications. *Nanotechnology* **2003**, *14* (10), 1081-1097.

140. Li, D.; Wei, Q.; Wu, C.; Zhang, X.; Xue, Q.; Zheng, T.; Cao, M. Superhydrophilicity and Strong Salt-Affinity: Zwitterionic Polymer Grafted Surfaces with Significant Potentials Particularly in Biological Systems. *Adv. Colloid Interface Sci* **2020**, 278, 102141.

141. Nie, G.; Li, G.; Wang, L.; Zhang, X. Nanocomposites of Polymer Brush and Inorganic Nanoparticles: Preparation, Characterization and Application. *Polymer Chemistry* **2016**, *7* (4), 753-769.

142. Tokareva, I.; Minko, S.; Fendler, J. H.; Hutter, E. Nanosensors Based on Responsive Polymer Brushes and Gold Nanoparticle Enhanced Transmission Surface Plasmon Resonance Spectroscopy. *J. Am. Chem. Soc.* **2004**, *126* (49), 15950-15951.

143. Lupitskyy, R.; Motornov, M.; Minko, S. Single Nanoparticle Plasmonic Devices by the "grafting to" Method. *Langmuir* **2008**, *24* (16), 8976-8980.

144. Bobrin, V.A.; Chen, S.P.; Grandes Reyes, C.F.; Sun, B.; Ng, C.K.; Kim, Y.; Purcell, D.; Jia, Z.; Gu, W.; Armstrong, J.W.; McAuley, J.; Monteiro, M. J. Water-Borne Nanocoating

for Rapid Inactivation of SARS-CoV-2 and Other Viruses. *ACS Nano* **2021**, *15* (9), 14915-14927.

145. Chen, P. C.; Du, J. S.; Meckes, B.; Huang, L.; Xie, Z.; Hedrick, J. L.; Dravid, V.P.; Mirkin, C. A. Structural Evolution of Three-Component Nanoparticles in Polymer Nanoreactors. *J. Am. Chem. Soc.* **2017**, *139* (29), 9876-9884.
146. Liu, Y.; Wang, J.; Zhang, M.; Li, H.; Lin, Z. Polymer-Ligated Nanocrystals Enabled by Nonlinear Block Copolymer Nanoreactors: Synthesis, Properties, and Applications. *ACS Nano* **2020**, *14* (10), 12491-12521.
147. Nakamura, S.; Mitomo, H.; Ijiro, K. Assembly and Active Control of Nanoparticles using Polymer Brushes as a Scaffold. *Chemistry Letters* **2021**, *50* (2), 361-370.
148. Kiremitler, N. B.; Pekdemir, S.; Patarroyo, J.; Karabel, S.; Torun, I.; Puntes, V. F.; Onses, M. S. Assembly of Plasmonic Nanoparticles on Nanopatterns of Polymer Brushes Fabricated by Electrospin Nanolithography. *ACS Macro Letters* **2017**, *6* (6), 603-608.
149. Oren, R.; Liang, Z.; Barnard, J. S.; Warren, S. C.; Wiesner, U.; Huck, W. T. Organization of Nanoparticles in Polymer Brushes. *J. Am. Chem. Soc.* **2009**, *131* (5), 1670-1671.
150. Button, B.; Cai, L. H.; Ehre, C.; Kesimer, M.; Hill, D. B.; Sheehan, J. K.; Boucher, R. C.; Rubinstein, M. A periciliary brush promotes the lung health by separating the mucus layer from airway epithelia. *Science* **2012**, *337* (6097), 937-941.
151. Ritsema Van Eck, G. C.; Chiappisi, L.; de Beer, S. Fundamentals and Applications of Polymer Brushes in Air. ACS Appl. Polym. Mater. 2022, 4, 3062−3087
152. Kim, Y.-Y.; Uezu, K. Functional Microfiber Nonwoven Fabric with Copper Ion-Immobilized Polymer Brush for Detection and Adsorption of Acetone Gas. *Sensors* **2022**, *22* (1), 91.
153. Yang, H.; Zhu, H.; Hendrix, M. M.; Lousberg, N. J.; de With, G.; Esteves, A. C. C.; Xin, J. H. Temperature-Triggered Collection and Release of Water from Fogs by a Sponge-Like Cotton Fabric. *Advanced Materials* **2013**, *25* (8), 1150-1154.
154. Cheng, S.; Stevens, M. J.; Grest, G. S. Ordering Nanoparticles with Polymer Brushes. *J. Chem. Phys.* **2017**, *147* (22), 224901.
155. Yang, E.; Ivancic, R. J.; Lin, E. Y.; Riggleman, R. A. Effect of Polymer–Nanoparticle Interaction on Strain Localization in Polymer Nanopillars. *Soft Matter* **2020**, *16* (37), 8639-8646.

156. Gao, H. M.; Li, B.; Zhang, R.; Sun, Z. Y.; Lu, Z. Y. Free Energy for Inclusion of Nanoparticles in Solvated Polymer Brushes from Molecular Dynamics Simulations. *J. Chem. Phys.* **2020**, *152* (9), 094905.
157. Curk, T.; Martinez-Veracoechea, F. J.; Frenkel, D.; Dobnikar, J. Nanoparticle Organization in Sandwiched Polymer Brushes. *Nano Letters* **2014**, *14* (5), 2617-2622.
158. , R. B.; Zhang, T.; Manohar, N.; Stebe, K. J.; Riggleman, R. A.; Lee, D. Effect of Polymer–Nanoparticle Interactions on Solvent-Driven Infiltration of Polymer (SIP) into Nanoparticle Packings: A Molecular Dynamics Study. *Molecular Systems Design & Engineering* **2020**, *5* (3), 666-674.
159. Egorov, S. A. Insertion of Nanoparticles into Polymer Brush under Variable Solvent Conditions. *J. Chem. Phys.* **2012**, *137* (13), 134905.
160. Etha, S. A.; Desai, P. R.; Sachar, H. S.; Das, S. Wetting Dynamics on Solvophilic, Soft, Porous, and Respnsive Surfaces. *Macromolecules* **2021**, *54* (2), 584-596.
161. Merlitz, H.; Wu, C. X.; Sommer, J. U. Inclusion free energy of nanoparticles in polymer brushes. *Macromolecules* **2012**, *45* (20), 8494-8501.
162. Grest, G. S., & Kremer, K. (1986). Molecular dynamics simulation for polymers in the presence of a heat bath. *Physical Review A*, *33*(5), 3628.
163. Everaers, R., Karimi-Varzaneh, H. A., Fleck, F., Hojdis, N., & Svaneborg, C. (2020). Kremer–Grest models for commodity polymer melts: linking theory, experiment, and simulation at the Kuhn scale. *Macromolecules*, *53*(6), 1901-1916.
164. Milchev, A., Dimitrov, D. I., & Binder, K. (2008). Excess free energy of nanoparticles in a polymer brush. *Polymer*, *49*(17), 3611-3618.
165. Galvin, C. J.; Dimitriou, M. D.; Satija, S. K.; Genzer, J. Swelling of polyelectrolyte and polyzwitterion brushes by humid vapors. *J. Am. Chem. Soc.* **2014**, *136* (36), 12737-12745.
166. Brió Pérez, M.; Cirelli, M.; de Beer, S. Degrafting of polymer brushes by exposure to humid air. *ACS Appl. Polym. Mater.* **2020**, *2* (8), 3039-3043.
167. Biesalski, M.; Rühe, J. Swelling of a polyelectrolyte brush in humid air. *Langmuir* **2000**, *16* (4), 1943-1950.
168. de Beer, S.; Mensink, L. I.; Kieviet, B. D. Geometry-dependent insertion forces on particles in swollen polymer brushes. *Macromolecules* **2016**, *49* (3), 1070-1078.

169. Maas, J. H.; Fleer, G. J.; Leermakers, F. A. M.; Cohen Stuart, M. A. Wetting of a polymer brush by a chemically identical polymer melt: Phase diagram and film stability. *Langmuir* **2002**, *18* (23), 8871-8880.

170. Plimpton, S. Fast Parallel Algorithms for Short-Range Molecular Dynamics. *J. Chem. Phys.* **1995**, *117* (1), 1-19.

171. Nosé, S. A Unified Formulation of the Constant Temperature Molecular Dynamics Methods. *J. Chem. Phys.* **1984**, *81* (1), 511-519.

172. Hoover, W. G. Canonical Dynamics: Equilibrium Phase-Space Distributions. *Phys. Rev. A* **1985**, *31* (3), 1695.

173. Murat, M.; Grest, G. S. Structure of a Grafted Polymer Brush: A Molecular Dynamics Simulation. *Macromolecules* **1989**, *22* (10), 4054-4059.

174. Stukowski, A. Visualization and Analysis of Atomistic Simulation Data with OVITO–the Open Visualization Tool. *Model. Simul. Mater. Sci. Eng* **2009**, *18* (1), 015012.

175. Essafri, I., Morineau, D. & Ghoufi, A. Microphase separation of a miscible binary liquid mixture under confinement at the nanoscale. Npj Comput. Mater. 5, 42 (2019).

176. Guo, X.-Y., Watermann, T. & Sebastiani, D. Local microphase separation of a binary liquid under nanoscale confinement. J. Phys. Chem. B 118, 10207 (2014).

177. You, F., Yu, Y. & Gao, G. Structures and adsorption of binary hard-core yukawa mixtures in a slitlike pore: grand canonical monte carlo simulation and density-functional study. J. Chem. Phys. 123, 114705 (2005).

178. Krycka, K. L., Dura, J. A., Langston, L. J. & Burba, C. M. Nanoconfinement-induced phase segregation of binary benzene cyclohexane solutions within a chemically inert matrix. J. Phys. Chem. C 122, 7676 (2018).

179. Harrach, M. F., Drossei, B., Winschel, W., Gutmann, T. & Buntkowsky, G. Mixtures of isobutyric acid and water confined in cylindrical silica nanopores revisited: A combined solid-state nmr and molecular dynamics simulation study. J. Phys. Chem. C119, 28961 (2015).

180. Abdel Hamid, A. R. et al. Microphase separation of binary liquids confined in cylindrical pores. J. Phys. Chem. C 120, 9245 (2016).

181. Abdel Hamid, A. R. et al. Multiple glass transitions of microphase separated binary liquids confined in mcm-41. J. Phys. Chem. C120, 11049 (2016).

182. Mhanna, R. et al. More room for microphase separation: an extended study on binary liquids confined in sba-15 cylindrical pores. J. Chem. Phys. 146, 024501 (2017).
183. Mhanna, R. et al. Dynamic heterogeneities in liquid mixtures confined in nanopores. J. Phys. Chem. B 124, 3152 (2020).
184. Vegas Mendoza, S. M., Avella Moreno, E., Guerrero Fajardo, C. A. & Fierro Medina, R. Liquid–liquid continuous extraction and fractional distillation for the removal of organic compounds from the wastewater of the oil industry. Water 11, 1452 (2019).
185. Antony, F. M., Pal, D. & Wasewar, K. Separation of bio-products by liquid–liquid extraction. Phys. Sci. Rev. 6 (2021).
186. Bokhary, A., Leitch, M. & Liao, B. Q. Liquid–liquid extraction technology for resource recovery: Applications, potential, and perspectives. J. Water Process Eng. 40, 101762 (2021).
187. Faller, R., Kolb, A., & Müller-Plathe, F. (1999). Local chain ordering in amorphous polymer melts: influence of chain stiffness. *Phys. Chem. Chem. Phys. 1*(9), 2071-2076.
188. Graessley, W. W. Entangled linear, branched and network polymer systems – Molecular theories. *Adv. Polym. Sci.* **1982**, 47, 67
189. Marrucci, G. (1985). Relaxation by reptation and tube enlargement: A model for polydisperse polymers. *J. Polym. Sci., Polym. Phys. Ed*, *23*(1), 159-177.
190. Rubinstein, M., & Colby, R. H. (1988). Self-consistent theory of polydisperse entangled polymers: Linear viscoelasticity of binary blends. *J. Chem. Phys. 89*(8), 5291-5306.
191. Marrucci, G., & Ianniruberto, G. (2003). Flow-induced orientation and stretching of entangled polymers. *Philos. Trans. R. Soc., A 361*(1805), 677-688.
192. Ianniruberto, G., & Marrucci, G. (2014). Convective constraint release (CCR) revisited. . *J. Rheol. 58*(1), 89-102.
193. Rosa, A., & Everaers, R. (2014). Ring polymers in the melt state: the physics of crumpling. *Phys. Rev. Lett*, *112*(11), 118302.
194. Halverson, J. D., Lee, W. B., Grest, G. S., Grosberg, A. Y., & Kremer, K. (2011). Molecular dynamics simulation study of nonconcatenated ring polymers in a melt. *The J. Chem. Phys. 134*, 204904.
195. Rosa, A., & Everaers, R. (2008). Structure and dynamics of interphase chromosomes. *PLoS Comput. Biol. 4*(8), e1000153.

196. Halverson, J. D., Grest, G. S., Grosberg, A. Y., & Kremer, K. (2012). Rheology of ring polymer melts: From linear contaminants to ring-linear blends. *Phys. Rev. Lett. 108*(3), 038301.

197. Wittmer, J. P., Meyer, H., Baschnagel, J., Johner, A., Obukhov, S., Mattioni, L., Müller, M., & Semenov, A. N. (2004). Long range bond-bond correlations in dense polymer solutions *Phys. Rev. Lett. 93*(14), 147801.